



The Cepheid Period-Luminosity Relation and the Distance to the Andromeda Galaxy

Telescope Group Project 2025/26

David Clayton, JP Duminy, Mimi Gornig, Amy Hall, Harsha Kuruganti

Supervised by Professor Kenneth Duncan

ABSTRACT

Cepheid variable stars are crucial distance indicators in the local Universe. These stars pulsate via the kappa opacity mechanism and exhibit a relationship between their period of pulsation and their intrinsic luminosity, known as the period-luminosity (P-L) relation. We present a P-L relation calibrated with 6 Classical Cepheid variables imaged over 5 weeks. MCMC methods were used to fit the periods of Cepheids; a hierarchical Bayesian inference model was then used to fit the P-L relation. The final form was $M_V = -2.087^{+0.191}_{-0.183} (\log_{10}(P) - 1) - 3.817^{+0.072}_{-0.071}$ with an intrinsic scatter of $\sigma = 0.118^{+0.064}_{-0.039}$, which is within the 95% credible interval of values in literature [1]. A Classical Cepheid in the Andromeda Galaxy, M31 CV1, then had its period determined: by placing M31 CV1 onto the calibrated P-L relation, a distance measurement of $D = 660^{+66}_{-60} \text{ kpc}$ to the Andromeda Galaxy was derived, which is again within the 95% credible interval but underestimated compared to the literature value of $761 \pm 11 \text{ kpc}$ [2]. While 11 Cepheids were observed, only 6 were used to calibrate the P-L relation: unavoidable saturation and low exposure times caused exposures to be significantly read-noise-limited, which was the cause for omission from the P-L relation for 4 Cepheids and introduced systematic errors to the remaining Cepheids.

INTRODUCTION

COSMIC DISTANCE LADDER

Accurate distance measurements in astronomy are crucial to furthering our understanding of the Universe: the distance to an object guides our understanding of its physical properties. In the local neighbourhood, trigonometric parallax allows for accurate and direct distance measurements. However, parallax is limited to a maximum range of around 9.2 kpc with current technology [3]; thus, astronomers use a chain of deduction known as the **cosmic distance ladder** to determine distances beyond. A crucial aspect of this ladder is the concept of a **standard candle**. Standard candles are objects for which we know the intrinsic luminosity, or the absolute magnitude M . Observations of a standard candle may then use the relationship between M and the apparent magnitude m , known as the distance modulus $\mu \equiv m - M$ (Eq. 1), to determine its distance.

$$\mu = 5 \log_{10} \left(\frac{d(\text{pc})}{10} \right) \quad (1)$$

Cepheid variable stars were the first confirmed standard candles. Variable stars are generally any stars which have observed variations in their apparent magnitude from Earth: Cepheids are a specific type of pulsating variable star. In 1912, astronomer Henrietta Swan Leavitt published a paper observing the existence of a relationship between the period of pulsation and brightness of Cepheids in the Small Magellanic Cloud [4]. Leavitt surmised that since these Cepheids were located in the same dwarf galaxy, they were about the same distance from Earth, and so the period of pulsation was likely as-

sociated with their intrinsic luminosity. This relationship is now referred to as the **period-luminosity** relation (henceforth P-L relation). In her paper, Leavitt also noted the similarities between the light curves of Cepheids in the Small Magellanic Cloud and those in the Milky Way. Though she passed away in 1921 without revisiting the matter, this observation was significant: if distance measurements to Cepheid variables could be determined from trigonometric parallax, it would be possible to calibrate the P-L relation, enabling distance measurements to Cepheids at greater distances. This is a key component of the cosmic distance ladder: each rung calibrates the next.

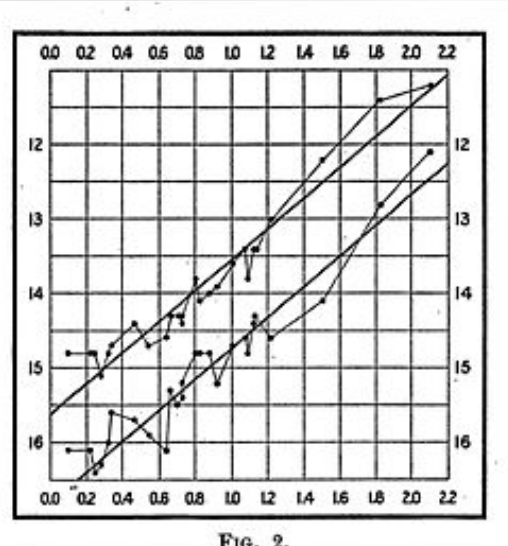


Figure 1: The original P-L relation in the 1912 paper [4].

In 1925, astronomer Edwin Hubble located a Cepheid in what was known as the Andromeda Nebula and used it to conclusively prove that it lay outside the Milky Way, settling the debate in astronomy over whether Andromeda was its own galaxy

or a nebula [5]. Cepheids have since emerged as crucially important distance indicators [6]. The P-L relation has been extensively studied and calibrated [7]: issues arising with the distance scale led to the eventual discovery that there are different populations of Cepheids, each with unique P-L relations: classical (Population I) Cepheids and Population II Cepheids. Classical Cepheids are young and found in the spiral arms; Population II Cepheids are older and found in the bulge and globular clusters [8]. Furthermore, the dependence of metallicity and colour on P-L relations has been investigated.

Decades later, among the key projects of the eponymous Hubble Space Telescope was the measurement of the Hubble constant through classical Cepheids, thus constraining the age of the Universe and the rate at which it is expanding [9].

CLASSICAL CEPHEIDS

Classical Cepheid variables are intermediate-mass post-main sequence stars that have entered the core helium burning phase. They are classified as either bright giants or low-luminosity supergiants, with masses $4M_{\odot} - 20M_{\odot}$ [10] and luminosities $1,000L_{\odot} - 50,000L_{\odot}$ [11]. Their outer envelopes are unstable to pulsations; they occupy a region of the H-R diagram known as the **instability strip** (Fig. 2), which is populated by a number of different classes of pulsating stars [12]. In the case of Cepheids, the pulsations are driven by the **κ opacity mechanism**. Partially-ionised stellar layers that move inwards during a compression phase of a pulsation become more opaque to radiation: this causes an accumulation of heat under the layer which in turn causes an increase in pressure which pushes the

layer outwards once more. The opacity of the layer decreases as it is pushed out, and heat will flow out; thus the process is cyclic, which led it to be originally termed the 'Eddington Valve'. In classical Cepheids, the change in opacity is due to He^{+} ions becoming doubly-ionised during the compression; during expansion, these ions recombine with free electrons to become singly-ionised [13] once again. Henceforth 'Cepheid' shall refer to the classical variety unless stated otherwise.

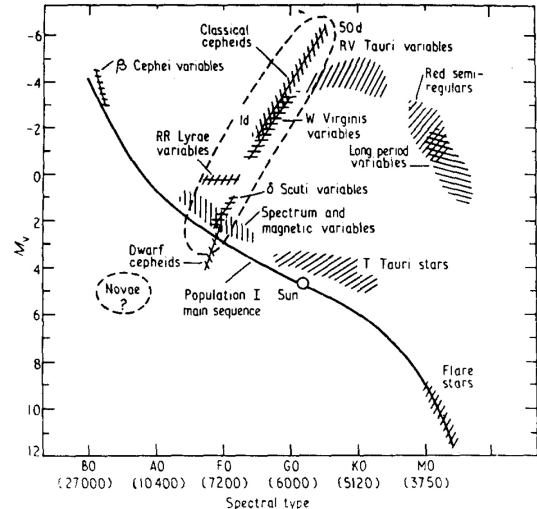


Figure 2: H-R diagram showing the instability strip and the position of classical Cepheid variables within it [14].

The κ opacity mechanism manifests as a periodic variation in the brightness of Cepheids [15]. The surface temperature of the star increases as it rapidly contracts; a maximum of the brightness occurs at the maximum expansion velocity of the outer layer, which is correlated with the maximum surface temperature [13]. The expansion is comparably more gentle, meaning Cepheid light curves are characterised by a distinct asymmetric 'sawtooth' shape: a sharp rise in brightness followed by a gradual dimming phase.

The shape of the light curve of a Cepheid is also wavelength-dependent.

Observations in shorter wavelengths are characterised by larger variations in amplitude and more asymmetric curves, exhibiting a strong sawtooth shape. Observations in longer wavelengths are associated with greater symmetry but weaker amplitude variations [16], appearing more sinusoidal. There also exists a subset of short-period Cepheids known as s-Cepheids which are characterised primarily by sinusoidal light curves [17].

Cepheids exhibit different modes of pulsation [18]. Most pulsate in either the fundamental mode or first overtone; rarely, some are observed to pulsate in the second overtone [19]. There also ex-

ist 'beat' Cepheids, which simultaneously pulsate in two or three modes [20]; and 'bump' Cepheids, which exhibit a bump on their light curves [21].

There are currently around 3,600 known classical Cepheids in the Milky Way [22]. In this project we sought to image 11 to calibrate a galactic P-L relation. In addition, M31 CV1, a classical Cepheid in the Andromeda Galaxy, was imaged. Once its period was determined, M31 CV1, it was placed onto the calibrated P-L relation to derive a fundamental distance measurement to the Andromeda Galaxy. This echoes the work of Hubble a century ago.

CEPHEID LIBRARY

Cepheid	RA [hr]	Dec [deg]	Mode	Distance [pc]
01 MW Cygni	20 12 22.83	+32 52 17.8	F	1856.9
02 V520 Cygni	20 54 57.53	+47 32 01.7	F	2272.2
03 VX Cygni	20 57 20.83	+40 10 39.1	F	3114.7
04 VY Cygni	21 04 16.63	+39 58 20.1	F	2080.1
05 CP Cephei	21 57 52.69	+56 09 50.0	F	3641.3
06 Z Lacertae	22 40 52.15	+56 49 46.1	F	1972.4
07 V Lacertae	22 48 38.00	+56 19 17.5	F	2022.2
08 SW Cassiopeiae	23 07 10.08	+58 33 15.1	F	2167.0
09 TU Cassiopeiae	00 26 19.45	+51 16 49.3	F/1H	977.2
10 DL Cassiopeiae	00 29 58.59	+60 12 43.1	F	1724.8
11 V636 Cassiopeiae	01 32 43.22	+63 35 37.7	1H	733.2
M31 CV1	00 41 27.30	+41 10 10.4	-	-

Table 1: The twelve Cepheids observed, including the Andromeda Galaxy Cepheid M31 CV1. F indicates the fundamental mode; 1H indicates the first overtone [23]. It should be noted TU Cas is a known beat Cepheid [24]

The coordinates, modes of pulsation, and distances of the eleven galactic Cepheids and M31 CV1 are displayed in

Table 1.

The P-L relation was calibrated with distances obtained from parallax measure-

ments. Though Gaia DR3 provided parallax measurements of unprecedented accuracy [3], the fractional uncertainties on the distances to more distant stars is large. It is noted in literature that a probabilistic approach is necessary to infer the distances from the parallax measurements [25]. In 2021 Bailer-Jones et al. [26] used rigorous MCMC methods to deliver a correc-

tion to the Gaia DR3 measurements, which we consequently took as our literature parallax measurements. The quoted distance values are the median of the photogeometric posterior from this catalogue, which employed a direction-dependent prior and used both the colour and apparent magnitude of stars to improve both accuracy and precision.

METHODOLOGY

OBSERVATION NIGHTS

When observing Cepheids, it is crucial to achieve sufficient phase coverage of their light curves as this facilitates accurate determination of their pulsation periods. For this reason it is necessary to conduct observations over a long time period with multiple epochs. Observations commenced on 2025-09-22 and continued until 2025-10-23; the timing between epochs was based on availability and observing conditions.

There were 14 epochs in total, of which 8 included a full set of galactic Cepheid and standard star observations. Observations of M31 CV1 required a significantly longer exposure time and were thus lower-priority: unfortunately, timing and availability constraints resulted in a limited number of M31 CV1 exposures being made available. These 8 primary observing epochs were supplemented by a further 6 observing epochs generously queued by other users of the telescope. These supplementary nights lacked standard star observations and only included a limited number of galactic Cepheids: they were nonetheless useful to improve the phase coverage of the light curves.

The observations were carried out with the PIRATE (Physics Innovations

Robotic Telescope Explorer [27]) Mk IV telescope, located at the Teide Observatory in Tenerife, Spain. Its main optical system is a 24-inch (61 cm) f/6.5 Corrected Dall–Kirkham Astrograph (PlaneWave CDK24) [28]. Imaging was performed using an FLI ProLine camera with a KAF-16803 CCD detector (4096 x 4096 pixels with a pixel size of 9 μ m), giving a field of view of 32 arcmin and a pixel scale of 0.47 arcsec pixel $^{-1}$. The targets were extremely bright and were expected to quickly saturate, thus motivating the choice of 1x1 binning. The Cepheids were observed in the V-filter, whereas the standard star and M31 CV1 images were taken in both the V- and B-filters. The V-band was ideal for the primary Cepheid observations as the quantum efficiency of the KAF-16803 CCD peaks at 60% near 550 nm, close to the central wavelength 540 nm of the Johnson V-filter [29]. Furthermore, as the sawtooth shape is more exaggerated in lower wavelengths, the low-wavelength V-band observations would better facilitate modelling the shape of the light curve.

The raw images obtained from these observations were subsequently processed using standard astronomical data reduction procedures.

DATA REDUCTION

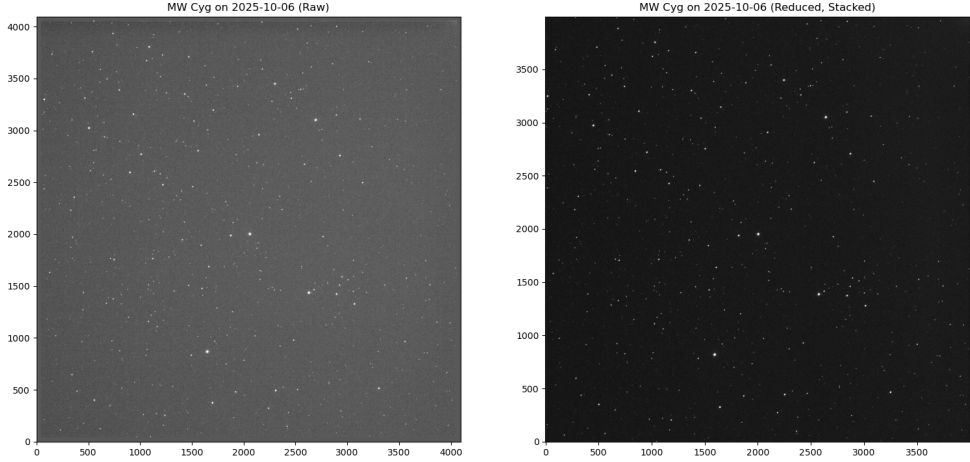


Figure 3: MW Cyg before reduction (left) and after calibration and stacking (right), observed on 2025-10-06. The reduced image appears noticeably darker because the electronic bias level has been subtracted from short-exposure frames with very low sky background.

The PIRATE telescope automatically takes its calibrations frames once per week during twilight. These calibration data are used to correct instrumental signatures in the science images prior to analysis.

Raw astronomical images taken with a charge-coupled device (CCD) contain a number of different instrumental signatures introduced by the detector itself, telescope optics and atmospheric conditions. The goal of data reduction is to remove these systematic effects so that the remaining signal more accurately reflects the true number of photons received from the target object. There are three main steps in the data reduction process, each of which corrects for a different source of noise in the image: bias subtraction, dark-frame correction, and flat-fielding. All raw images contained overscan and non-science edge regions introduced during

the CCD readout process. Overscan pixels are electronically generated during readout to monitor the bias level and do not correspond to photoactive detector pixels [30]. In addition, the outer edges of the frames exhibited vignetting. Accordingly, 50 pixels were removed from each edge of every frame so that only the fully illuminated science region remained for further processing.

The bias in a CCD is a low-level electronic offset applied to all pixels so that, when the accumulated charge in each pixel is converted by the analogue-to-digital converter into digital numbers, these values remain positive [31]. A bias frame is taken with the shutter closed and the exposure time minimised, only capturing this instrumental offset introduced by the detector electronics. Calibration bias frames for each week were combined using me-

dian stacking to produce a master bias frame, shown in Fig. 4. The median is preferred over the mean because it is more effective in removing transient artefacts such as cosmic rays.

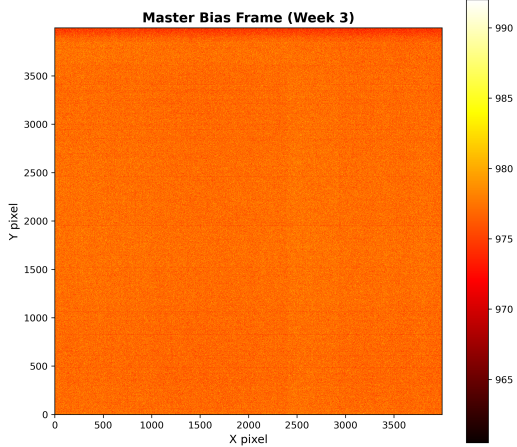


Figure 4: Master bias frame for week 3 produced by median combining individual bias exposures.

Dark current arises from thermally generated electrons that accumulate during the exposure, increasing the electron count in each pixel [30]. Most modern astronomical CCDs produce only a few ADU (Analogue-to-Digital Unit) per pixel per hour, so that the thermal contribution is small compared with other noise sources [31]. During our observations the PIRATE detector was operated at -30°C , which significantly suppresses thermal noise. As a result, the dark current was negligible, and thus dark-frame correction was not applied.

The final step in data reduction is flat-fielding. A CCD is made up of several pixels, and the sensitivity of each pixel can vary slightly due to dust, vignetting

and the intrinsic detector response [30]. To account for this, a flat-field image is taken with the CCD illuminated by a uniform light source. This image is then normalised so that mean pixel count is unity. Weekly flat-field frames were median combined to produce a master flat field, Fig. 5.

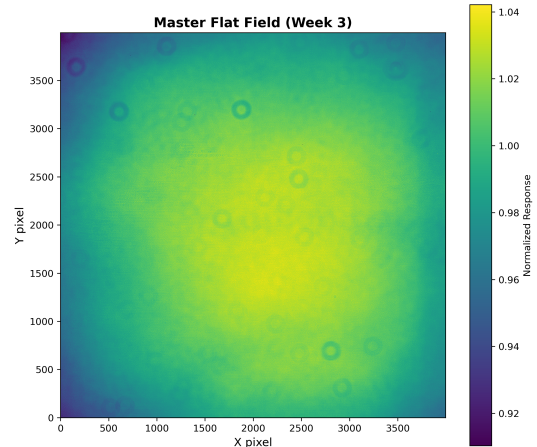


Figure 5: Normalised master flat-field frame for week 3.

Each observing night was mapped to its corresponding week's calibration set, ensuring that science images were reduced using calibrations taken under similar conditions. Each trimmed Cepheid image was reduced individually by subtracting the corresponding master bias frame and dividing by the normalised master flat field. Cepheids were imaged in bursts of ten consecutive exposures. Finally, the reduced images for each Cepheid on a given night within each burst were stacked to improve the signal-to-noise ratio (SNR). Fig. 3 shows a comparison image of MW Cygni before and after reduction was applied.

PHOTOMETRY

TARGET LOCATION

Initially, the locations of the targets in their images were computed using the *astropy.wcs* inbuilt World Co-ordinate System (WCS) and necessary FITS header items. However, a WCS could not be derived for some images due to a lack of appropriate headers. Furthermore, the WCS often failed in locating the targets, missing them by a distance of up to 100 pixels. This method was consequently discarded.

The pixel co-ordinates of each target were correctly computed in a two-stage process. Firstly, the approximate position of the target was manually estimated by viewing the image using the SAOImage DS9 software. This achieved an accuracy of $\lesssim 10$ pixels from the target's true position. Secondly, the position of the target was refined using the photutils function DAOStarFinder, which operates the DAOFIND algorithm [32].

This located sources in the image which followed a Gaussian intensity distribution and an amplitude greater than a specified threshold, thus identifying all stars in the image. The source closest to the hand-marked pixel coordinates was identified as the target star. The results of the DAOFIND algorithm were compared with star charts to confirm it had identified the target star correctly; a diagnostic was added to flag images where the closest source to the hand-marked guess was greater than 10 pixels away in case of human error when marking targets. The DAOFIND algorithm served as both a diagnostic and to refine the hand-marked pixel coordinates.

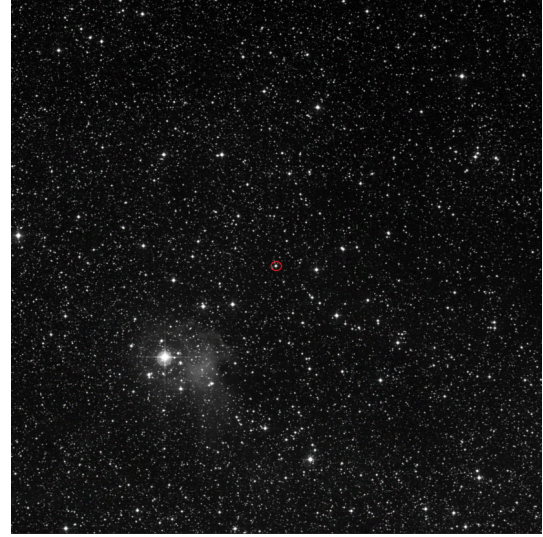


Figure 6: A finder chart for V520 Cygni (marked in red).

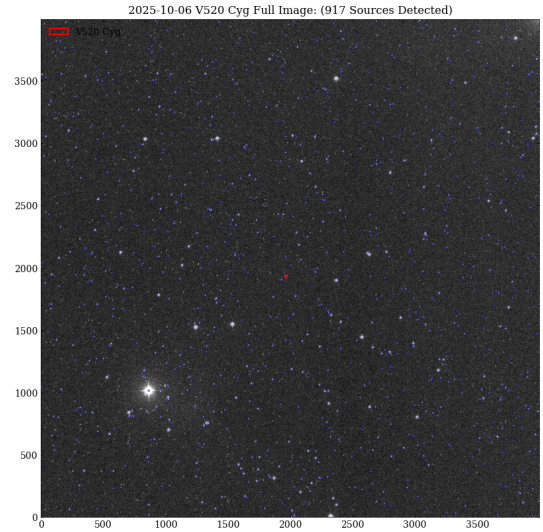


Figure 7: DAOStarFinder results for V520 Cygni on 2025-10-06. The algorithm found a total of 917 sources (blue). The estimated location of the Cepheid (red) matches the finder chart.

Around the estimated target location, the point spread function (PSF) of the target's flux was obtained by fitting a 2D Gaussian to its intensity distribution. The fitted centroid of the Gaussian improved

the location estimate to sub-pixel accuracy (see Fig. 8). The FWHM of the Gaussian was also computed, which was the main parameter for the estimation of the aperture size.

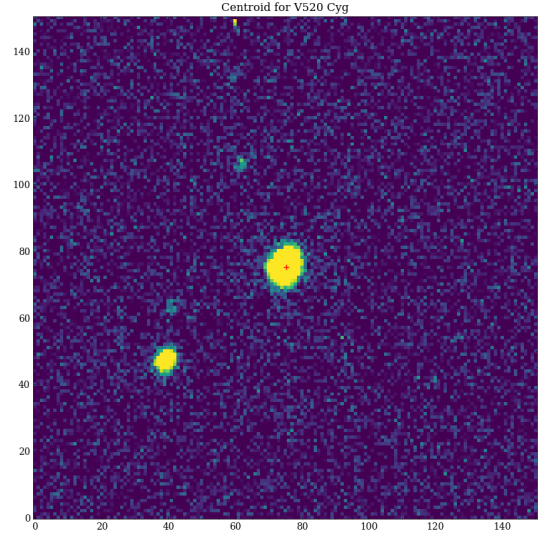


Figure 8: Centroided location of V520 Cygni on 2025-10-06.

APERTURE PHOTOMETRY

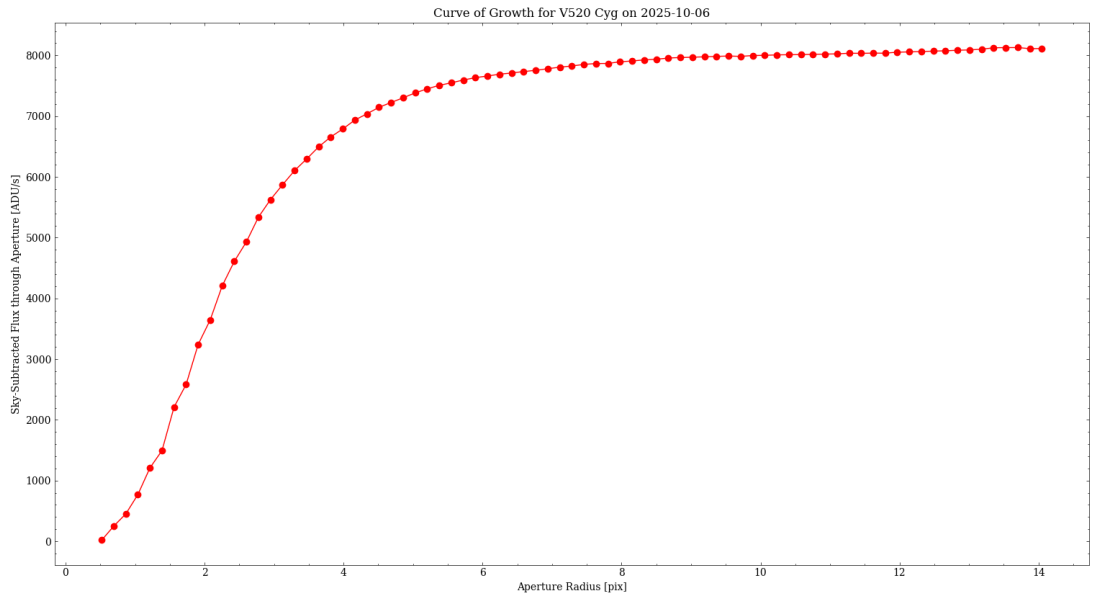


Figure 9: Curve of growth for an aperture around V520 Cygni on 2025-10-06. As can be seen, the flux plateaus at large radii. An important property of the plateau is a marginally smaller flux occurs with a significantly smaller aperture.

The aperture radius was estimated to be the smallest radius on the plateau of the target's curve of growth (see Fig. 9).

The sky background was estimated

with a circular annulus concentric to the aperture with inner and outer radii of 1.5x and 2x the aperture radius respectively [33]. To provide an even and accu-

rate background subtraction, the sky annulus was sigma-clipped with built-in *astropy* functionality [34] to account for any unwanted noise such as cosmic rays that would bias the background estimate. See Fig. 10. The per-pixel sky background was estimated to be the median intensity of the sigma-clipped background in the annulus.

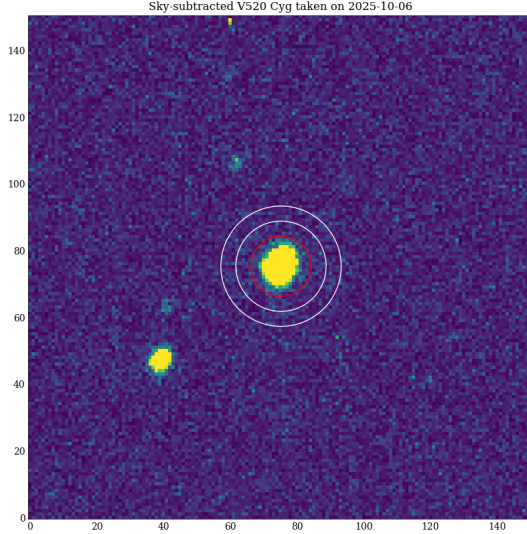


Figure 10: Target aperture (red) and background annulus (white) around V520 Cygni on 2025-10-06.

The sky-subtracted CCD fluxes were converted into instrumental magnitudes using the logarithmic magnitude equation,

$$m_{\text{inst}} = -2.5 \log_{10}(F) \quad (2)$$

where F is the measured flux in digital numbers. For calibration purposes, fluxes were normalised by the exposure time to obtain counts per second ensuring that instrumental magnitudes are independent of exposure duration.

The uncertainty on m_{inst} was computed as $\frac{1.086}{\text{SNR}}$, where the SNR is given by the complete CCD equation [30]:

$$\text{SNR} = \frac{N_* t}{\sqrt{N_* t + n_{\text{pix}} \left(1 + \frac{n_{\text{pix}}}{n_B}\right) (N_S t + N_R^2)}} \quad (3)$$

where N_* is the target flux in electrons rather than digital numbers, n_{pix} is the pixel area of the aperture, n_B is the pixel area of the background annulus, N_S is the sky background flux per pixel, N_R is the per-pixel read-noise uncertainty for the stacked image, and t is the exposure time. The sigma-clipped sky-background was assumed to follow Poisson statistics. The read-noise term in Eq. 3 for an image stacked from m images all with equal read-noise n_r , is simply the product of the individual read-noise terms, mn_r^2 . As the dark current correction was unnecessary due to the cooling of the telescope, the dark current term was assumed to be negligible.

CORRECTIONS

ATMOSPHERIC EXTINCTION, ZERO POINT

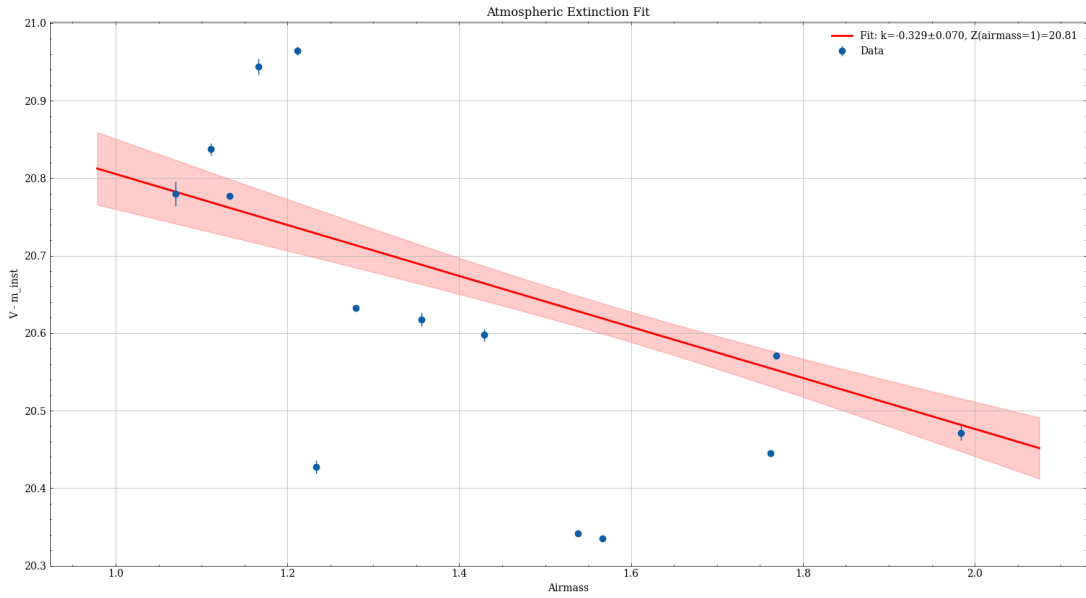


Figure 11: The linear atmospheric extinction fit.

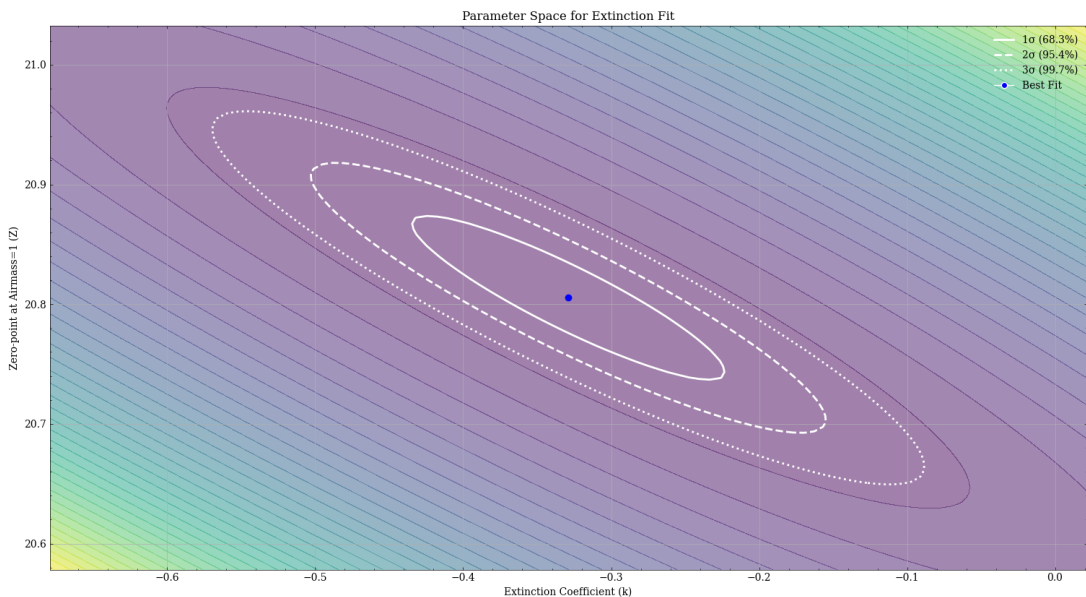


Figure 12: χ^2 contour plot visualising the covariance between the atmospheric extinction coefficient and zero point.

Light from stars is reduced as it passes through the Earth's atmosphere due to absorption and scattering by molecules of various gases. The magnitude of this effect depends on the airmass, defined as the relative optical path length through the atmosphere [35]. To quantify this effect, atmospheric extinction was modelled using a first-order linear approximation,

$$m_{atm} = m_{inst} - kX \quad (4)$$

where m_{atm} is the airmass corrected magnitude, m_{inst} is the instrumental magnitude, X is the airmass, and k is the atmospheric extinction coefficient in magnitudes per unit airmass [35]. Airmass values were calculated from FITS metadata using the recorded target coordinates, observation time, and observatory location. RA and DEC values were first extracted from the FITS headers and transformed to horizontal coordinates using the *astropy* library [34]. The altitude of each target was computed for the time of observation, and the airmass was defined using the approximation $X = \sec(z)$, where z is the zenith angle. This approximation was contingent on observations obtained at low to moderate airmass ($X \lesssim 2.92$ [36]), as was the case for the dataset analysed in this project (all airmasses < 2). The extinction coefficient was determined from standard star observations to account for atmospheric conditions.

Instrumental magnitudes were corrected to the standard photometric system using the derived zero point, ZP ,

$$m_{std} = m_{atm} + ZP, \quad (5)$$

where m_{std} is the standard photometric magnitude [35].

The extinction coefficient and photometric zero point were determined simultaneously using observations of standard

stars with known catalogue V -band magnitudes. The following relation was fitted as a straight-line graph:

$$V - m_{inst} = ZP + kX, \quad (6)$$

where V is the catalogue magnitude of the standard star in the V -band [35].

A weighted least-squares (WLS) regression was used to perform the fit, with each data point being weighted by the inverse variance of its photometric uncertainty, $w_i = 1/\sigma_i^2$ [37]. The use of WLS ensured that measurements with smaller photometric uncertainties contribute more strongly to the fit, preventing higher uncertainty data points from dominating the calibration [37]. The regression was performed using the *statsmodels* [37] WLS framework, which provided best-fit values for k and Z . The covariance matrix was also computed: uncertainties on the parameters were taken as the square root of the diagonals [37].

In the standard photometric calibration relation, the zero point is formally defined as the magnitude offset at zero airmass [35]. However, an airmass of $X = 0$ corresponds to the absence of an atmosphere and therefore represents an unphysical observing condition for ground-based observations [38].

As a result, the photometric zero point was instead evaluated at unit airmass ($X = 1$), which corresponds to observations at the zenith. Additionally, from a statistical perspective, since k and ZP are correlated parameters, evaluating the zero point at $X = 1$ rather than $X = 0$ reduces this covariance by placing the reference point closer to the centre of the airmass distribution, minimising the propagated uncertainty in the zero point [38].

The 6 aforementioned supplementary observing epochs did not include accompanying standard star observations. As a

result, while independent nightly extinction coefficients and zero points could be determined and applied to neighbouring nights, it would lead to poorly constrained solutions with increased statistical scatter. As a result, a single global extinction coefficient and zero point were fitted using all available standard star observations.

The atmospheric extinction correction was assessed by plotting $V - m_{\text{inst}}$ as a function of airmass, along with the best-fit linear model. Error bars corresponding to the magnitude uncertainties were included to visualise the weighting applied during the regression (larger errors carry smaller weights), as well as a 1σ shaded region.

The initial relation between catalogue magnitude and instrumental magnitude as a function of airmass found most points were within 2σ , although a potential outlier was identified at an airmass of 1.23. In order to confirm this, a graph of residuals was plotted, as seen in Fig. 13. This anomaly was a singular measurement error, which could be explained by a passing cloud or other atmospheric disturbances resulting in a poor exposure. Consequently, this star was eliminated from the analysis.

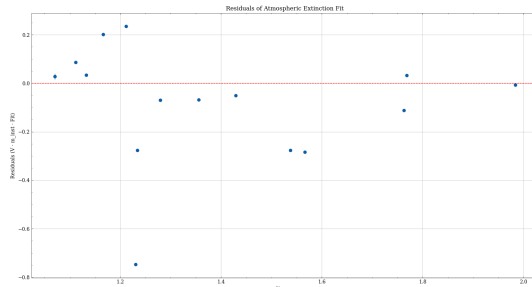


Figure 13: Diagnostic residual plot showing the deviation of each data point from the best fit line. Most points are well constrained with the exception of the anomaly at an airmass of 1.23.

Following a refit of the relation in Eq. 6, after the removal of the anomaly, the best-fit relation between catalogue magnitude and instrumental magnitude as a function of airmass is shown in Fig. 11. The fit yielded an atmospheric extinction coefficient of

$$k = 0.33 \pm 0.07 \text{mag/airmass}$$

and a photometric zero point evaluated at unit airmass of

$$ZP = 20.8 \pm 0.1 \text{mag}$$

The data exhibits a clear linear trend between $V - m_{\text{inst}}$ and airmass, with most data points within 2σ from the fitted model. The scatter about the best-fit line is consistent with the estimated photometric uncertainties, indicating that the first-order extinction model provides an adequate description of the atmospheric effects present in the dataset.

To further portray the uncertainty in the fitted parameters, a diagnostic plot of the (k , ZP) parameter space was constructed by evaluating the χ^2 statistic over a grid of extinction coefficient and zero point values. Confidence contours corresponding to 1σ , 2σ , and 3σ levels were plotted to illustrate the correlation between the extinction coefficient and zero point and to verify that the solution for these values were reliable. As seen in Fig. 12, the elliptical shape of the contours centred around the best fit point demonstrates a correlation between k and ZP , indicating that both parameters are well constrained, as expected from the linear extinction model.

INTERSTELLAR DUST EXTINCTION

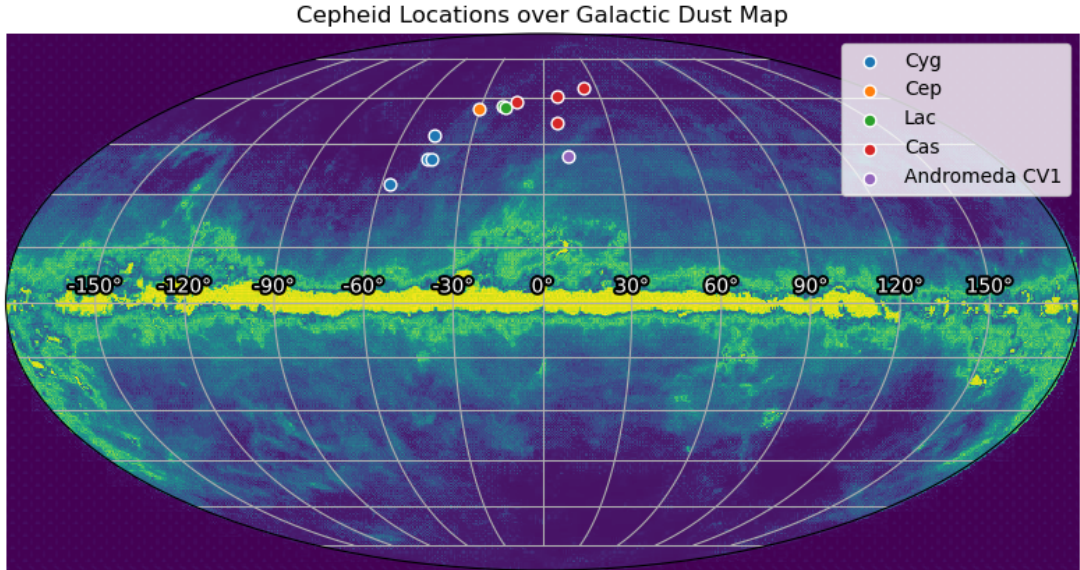


Figure 14: Location of each Cepheid observed overlayed on an all-sky view of the IRAS 100 micron imaging data combined using individual images from Schlegel et al. [39].

Calibrated magnitudes were corrected for interstellar dust extinction using the colour excess $E(B - V)$ values from literature [40]. The extinction in the V band was computed as

$$A_V = R_V * E(B - V), \quad (7)$$

where $R_V = 3.1$ was adopted as the standard extinction ratio for the interstellar medium [41]. The Cepheids sampled in this experiment are located in similar regions of the sky (see Fig. 14), as well as not being associated with dense molecular clouds or star-forming regions where de-

viations from the standard extinction law are commonly observed [41]. Any resulting systematic offsets can be assumed to be negligible compared to other sources of photometric uncertainty, justifying this value.

The final corrected magnitude was obtained by subtracting A_V from the calibrated magnitude,

$$V_0 = m_{std} - A_V \quad (8)$$

[41].

DIFFERENTIAL PHOTOMETRY

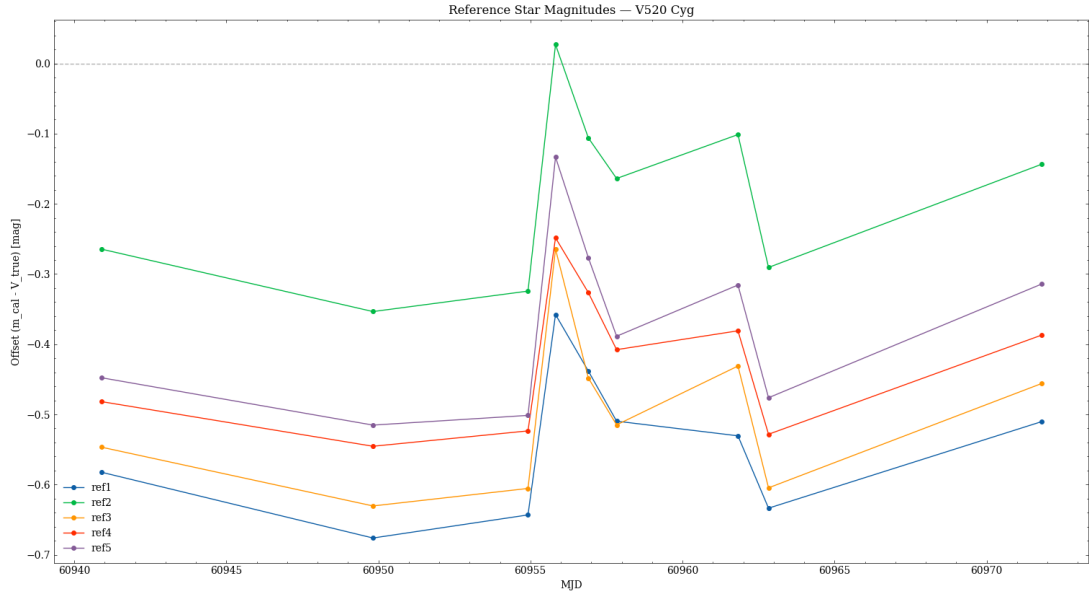


Figure 15: The systematic variations in night-to-night brightness due to observing conditions for V520 Cygni, quantified by the change in brightness of its reference stars.

It was crucial to ensure the actual variation in the intrinsic brightness of the Cepheids was being measured as opposed to night-to-night variations. Humidity, moonlight, light pollution, and cloud cover differ between epochs: these variations could introduce systematic errors into the light curve that could be misattributed to the pulsations of the Cepheid.

Differential photometry was employed to account for these systematic variations between nights. This involves the use of non-variable reference stars to quantify the nightly offset, thus 'normalising' the light curve to the intrinsic brightness variation of the Cepheid. Five reference stars were selected for each Cepheid. These reference stars were bright, non-variable, had known V-band magnitudes, and were chosen such that the different quadrants of the image were sampled.

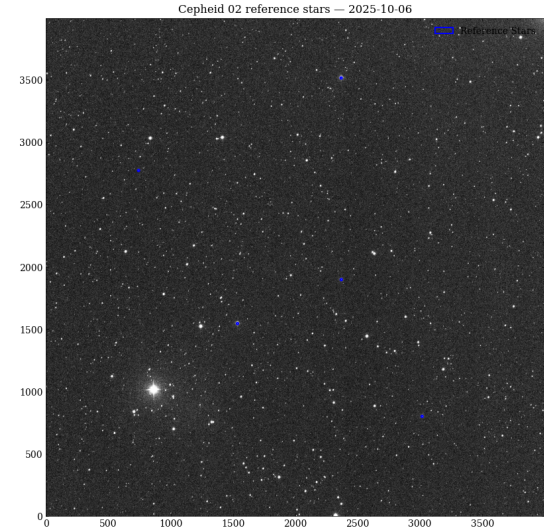


Figure 16: The reference stars of V520 Cygni on the reference night (blue).

The magnitudes of the reference stars were calculated using the aforementioned methodology. To avoid the significant time cost of manually marking five reference stars per Cepheid per night, the reference stars were instead marked on the defined reference night 2025-10-06. This

night was chosen as it was the night which produced the most successful and comprehensive series of observations. Then, a simple algorithm was employed to appropriately account for the different pixel coordinates between nights.

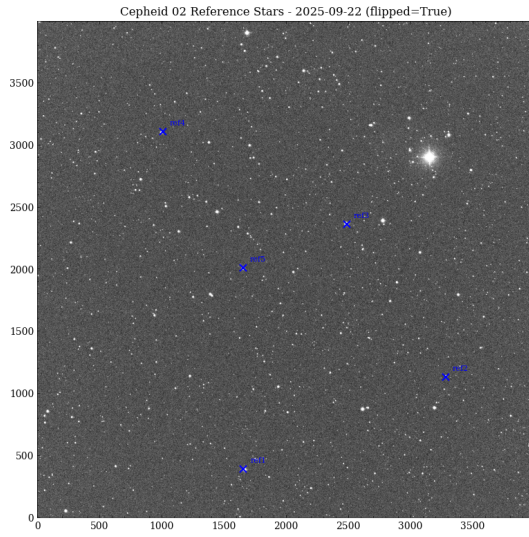


Figure 17: The reference star coordinate transformation algorithm.

The orientation of the image was not considered previously because the pixel coordinates of each Cepheid were marked manually for each night. The FITS headers contain a FLIPSTAT entry which indicates the orientation of the image. The reference direction was thus defined as the orientation of each Cepheid on its reference night. The image was then flipped

on nights when the orientation was different to the defined reference value. The image was also shifted between epochs: to account for this, the Cepheid was used to compute the translation of the pixel coordinates. The offset of the coordinates of the Cepheid were computed by comparison to the reference night, allowing the pixel coordinates of the reference stars to be appropriately transformed. The reference star photometry was inspected and it was confirmed the transformation algorithm was functional: the algorithm is demonstrated in Fig. 16 and Fig. 17.

The reference stars for each Cepheid had known standard V-band magnitudes [42]: as such, the systematic offset for each Cepheid on a given night was computed as the median offset of the reference stars from their known magnitudes. The median was taken in case of any outliers.

One inherent advantage of the differential photometry was that it provided a more reasonable error estimation by estimating the night-to-night systematic scatter, which is not included in the CCD equation. This prevents a systematic underestimation of errors.

The final output of the photometry pipeline consists of extinction and differentially-corrected V-band magnitudes for each Cepheid observation.

ANDROMEDA PHOTOMETRY

M31 CV1 could not be adequately observed due to timing constraints. Instead, SDSS g-band observations of M31 CV1 over 19 nights were supplied from the Liverpool Telescope (LT). These data were already fully reduced before they were supplied.

The LT data were not accompanied by standard star observations. In this case, a selection of reference stars in the image surrounding the Cepheid was used to calibrate the magnitudes. 4 suitable reference stars were chosen; there was no suitable candidate for the fifth reference star. Similarly to the Cepheid reference stars, these stars had well known g-band magnitudes queried from Pan-STARRS [43] with *astroquery* [44][45]. The median difference between the instrumental magnitudes of the reference stars and the literature magnitudes was determined to be the magnitude offset of the night, which encapsulated zero point, atmospheric, and night-to-night corrections.

Herein lay another benefit of differential photometry: as the reference stars had known magnitudes they could act as standard stars, correcting M31 CV1 accordingly.

The apparent magnitudes of M31 CV1

were calculated in the g-band, and had to be converted to the V-band so they could be correctly compared with the V-band P-L relation. The conversion was done with the two conversion relations of Eq. 9 and 10 [46].

$$V = g - 0.59(g - r) - 0.01 \pm 0.02 \quad (9)$$

where

$$(g - r) = \frac{1}{0.98}((B - V) - 0.22 \pm 0.04) \quad (10)$$

While best practice would involve computing $B - V$ for M31 CV1 from our observations and using this to transform from SDSS g to Johnson V, there were unfortunately insufficient data from our observations to perform this. The $B - V$ colour of M31 CV1 was thus taken from an outside source to be 1.28 [47]. With an assumed value for B-V, the g-band magnitudes could be directly converted to V-band magnitudes.

Once M31 CV1's magnitudes were converted into the V-band, dust corrections were then applied to get the final calibrated V-band magnitudes over the observation period, which could be analysed with the V-band P-L relation.

MODEL FITTING

The light curves of the Cepheids were expected to display a sawtooth shape, as observations were conducted in the shorter-wavelength 542 nm V-filter [16, 48]. However, the limited number of data points available meant the waveform would not necessarily be adequately-sampled. In light of this both a sinusoid and sawtooth model were fitted to the data in the event that a sinusoid would serve as a better model to sparsely-sampled data.

$$m(t) = A \sin\left(\frac{2\pi t}{P} + \phi\right) + M \quad (11)$$

where m is the apparent magnitude at time t , A is the amplitude, ϕ is the phase, M is the midline, and P is the period.

The sinusoid model was defined by Eq. 11 and computed using the numerical computing package *numpy* [49]. The sawtooth model was defined by its form in the scientific computing package *scipy* [50]. The *scipy* sawtooth model uses the same amplitude, period, phase and midline parameters as the sinusoid, but incorporates a width parameter, which describes the width of the rising ramp as a proportion of the total cycle.

The phase coverage of the light curves was incomplete, meaning fitting width

as a free parameter would cause a geometric degeneracy between width and period. Since the width parameter governs the portion of the period spent rising, the model could compensate variations in the period by altering the width. This would lead to the model exploring mathematically-possible yet physically-incorrect waveforms.

Another problem arose from the limited number of data points. The number of degrees of freedom v is defined as $N - k$, where N is the number of data points and k is the number of model parameters. Lower degrees of freedom indicate a less-flexible model which may represent the data points but not necessarily capture the underlying trends, known as overfitting. Overfitting is undesirable because it causes models to capture the noise in the data, resulting in systematic underestimation of uncertainties. Each Cepheid had 8 data points on average: a 5-parameter model would thus produce an unacceptable decrease in the degrees of freedom to 3. On this basis it was decided to fix the sawtooth width parameter to a physically-sensible value, a ratio of 1:3 between the brightening and dimming phase.

INITIALISATION

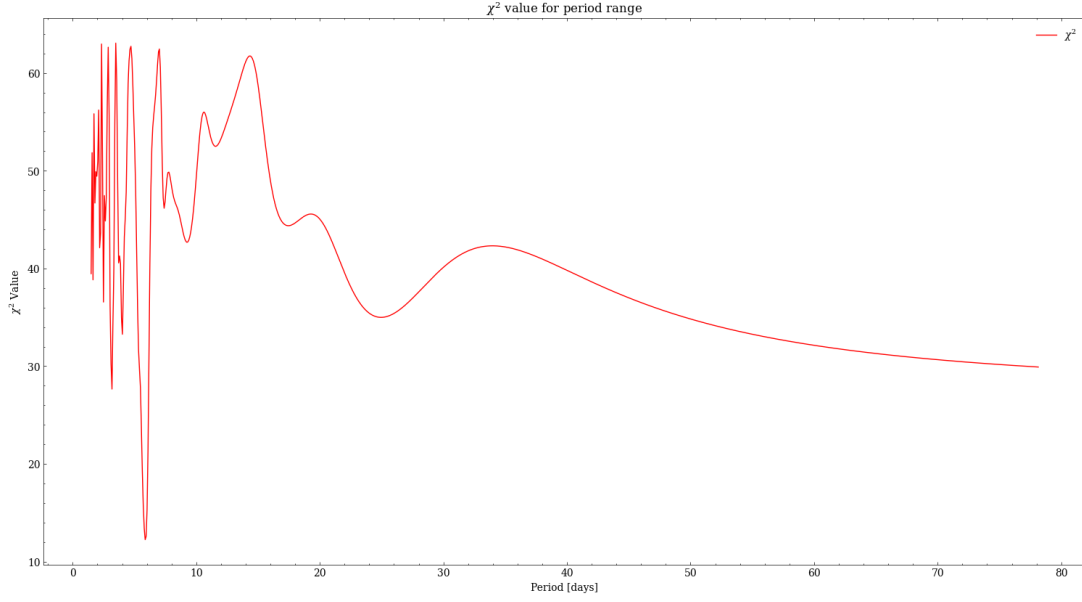


Figure 18: The χ^2 grid search for MW Cygni with the sinusoid model (literature period: 5.95 days).

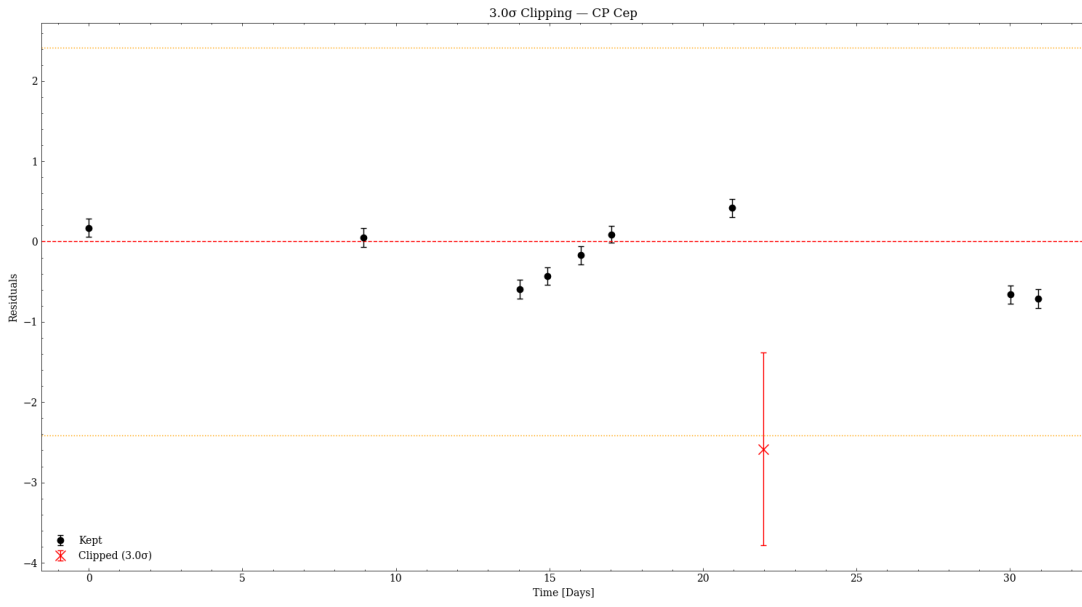


Figure 19: Trimming of an outlier data point in the light curve of CP Cephei. Due to limited data, the outlier rejection was conservative: 3σ .

The initialisation process for period-fitting the Cepheids was threefold: to determine the optimal model (sinusoid or sawtooth), to determine a best-guess for the initial values of the 4 parameters;

and to provide an initial assessment of goodness-of-fit.

The first stage in fitting the period of each Cepheid was to determine an initial guess for the period. Cepheids are

sometimes analysed in literature with the Lomb-Scargle periodogram [51, 52], which is based on Fourier decomposition. However, the L-S periodogram fits sinusoidal terms to the signal, which does not fully capture the asymmetric nature of the expected sawtooth shape. Furthermore, the sparse and uneven sampling of the light curve introduces aliasing which poses a problem for Fourier-based decomposition.

To determine an initial guess for the period value, a grid search was conducted over literature period range for both the sawtooth and sinusoid models. The periods of classical galactic Cepheids vary in literature: the shortest reported period is 1.49 days [53], whilst the longest reported is 78.14 days [54]. The models were fitted with the *curve_fit* function of *scipy* [50] which implements the Levenberg–Marquardt non-linear least squares algorithm [55]. The appropriate value of the initial guess for the period was determined by computing the χ^2 value (Eq. 12) at each period across the grid search.

$$\chi^2 = \sum_{i=1}^N \frac{(m_i - m_{model})^2}{\sigma_i^2} \quad (12)$$

where χ^2 is the chi-squared value, m_i is the measured magnitude at time t_i , m_{model} is the modelled magnitude at time t_i , σ_i is the uncertainty of m_i , and N is the number of data points. The χ^2 value is a quantitative measure of goodness-of-fit: a lower value indicates a better fit. To determine the optimal initial guess for the period and other parameters, the χ^2 value was computed at each point across the grid search: thus, the optimal initial guess would occur at the minimum χ^2 value.

It is crucial to be cautious of overfitting, given the limited number of data points compared to the number of parameters. For this reason it is custom to define the reduced chi-squared value (Eq. 13), which incorporates the aforementioned degrees of freedom v :

$$\chi_v^2 = \frac{\chi^2}{v} \quad (13)$$

where χ_v^2 is the reduced chi-squared and v are the degrees of freedom. The χ_v^2 value is useful and widely-used diagnostic because it penalises models that overfit data. In general, a value $\chi_v^2 \approx 1$ indicates a good fit; $\chi_v^2 > 1$ indicates a poorer fit; $\chi_v^2 < 1$ indicates overfitting. At the chi-squares minimum over the grid search, the value of χ_v^2 was computed for both the sinusoid and sawtooth models to provide a quantitative measure of goodness-of-fit for either model. The fit was also plotted for visual inspection as a qualitative check. As MCMC would refine the initial parameters, the reduced chi-squares value is also quoted in results as a recognisable, quantitative estimation of the goodness-of-fit.

Fig. 18 demonstrates the grid search on data for MW Cygni: there is an evident minimum in the χ^2 value corresponding to a period close to the literature value. This provides a suitable initial guess for the values of the parameters for the model fitting algorithm.

The initialisation process also diagnosed outlier data points to be trimmed before the model fitting. This was done through plotting of the residuals of a fit. An example for CP Cephei is shown in Fig. 19.

MCMC: PERIOD FITTING

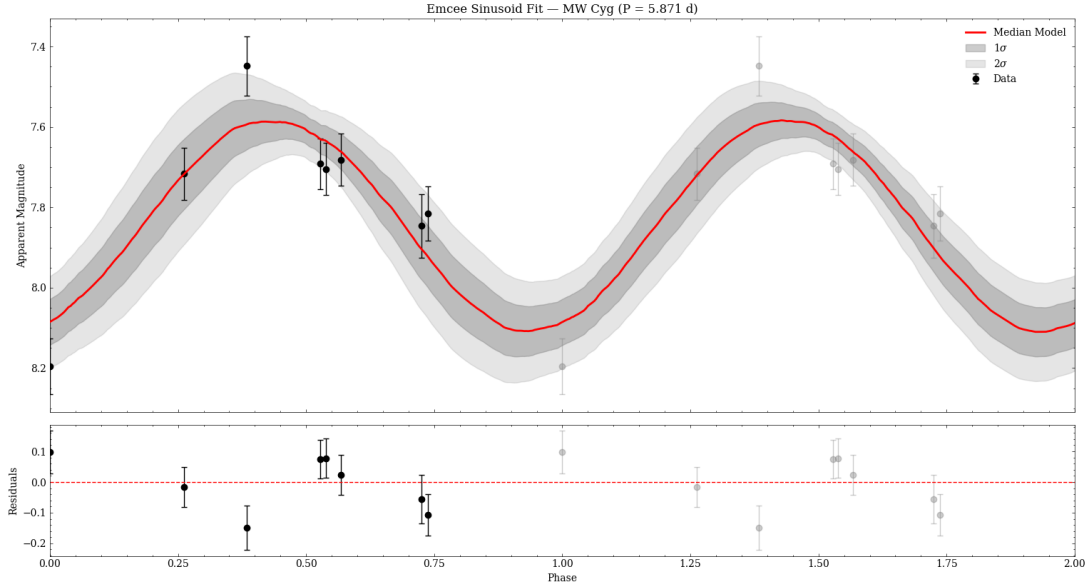


Figure 20: Phase-wrapped plot of the *MW Cygni* light curve and its fit (in this case, a sinusoid), with corresponding 68% and 95% credible intervals and residuals.

A Monte Carlo Markov Chain (MCMC) method from the *emcee* package [56] was used to sample the posterior distribution of the parameters of each Cepheid, starting from the initial guess. MCMC methods have grown commonplace in astrophysics literature to treat typically complex, high-dimensional and computationally-expensive models. Where analytical solutions are not feasible, MCMC methods seek to provide a numerical solution by sampling from the posterior distribution (Eq. 14).

$$p(\Theta | D) = \frac{1}{Z} p(\Theta) p(D | \Theta) \quad (14)$$

Eq. 14 is Bayes' theorem. $p(\Theta | D)$ represents the probability of the parameters given the data, known as the posterior probability; Z is the normalisation, known as the evidence; $p(D | \Theta)$ is the probability of the data given the parameters, known as the likelihood; and $p(\Theta)$ is the probability of the parameters, known as the prior.

It is in principle difficult to compute the normalisation [56]; however, since MCMC generates samples proportional to the posterior and compares probability ratios, this problem is avoided.

emcee is a Python implementation of an ensemble sampler with affine invariance [57]. Affine-invariance means the algorithm is unaffected by covariant parameters. The ensemble refers to an ensemble of 'walkers', where the proposed move for one walker depends on the positions of the other walkers.

Wide, flat priors constrained to physically-sensible values were chosen for each parameter. The ln-likelihood of the model is defined by Eq 15.

$$\ln(\mathcal{L}) = -\frac{1}{2}\chi^2 - \frac{1}{2}\ln(2\pi\sigma_i^2). \quad (15)$$

where \mathcal{L} is the likelihood.

As the algorithm computes ratios, the constant cancels in practice. Walkers in the ensemble were initialised around the

initial guess for each parameter: in the initialisation, the walkers were distributed by Gaussian noise scaled to each parameter to ensure they would fully explore parameter space.

An initial ‘burn-in’ run was conducted to allow the walkers to explore parameter space, allowing the Markov chain to reach equilibrium. The burn-in was then discarded such that the initial guess did not contaminate the chain that would be used for analysis. This was followed by a production run.

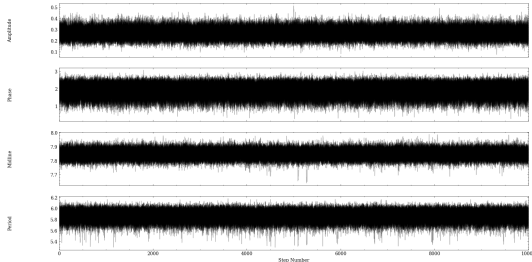


Figure 21: The parameter time series of MW Cygni. This is a visual representation of the Markov chain.

The principle of ergodicity is that a dynamic system will eventually visit every possible configuration given enough time. By this principle, a sufficiently-long Monte Carlo Markov Chain that converges will see its parameters converge towards their ‘true’ values. The principle method for evaluating a chain from *emcee* is the autocorrelation time τ [56]. The autocorrelation time is a measure of the number of steps over which samples remain correlated: a well-converged chain is indicated by a low autocorrelation time. Chains of length $\approx 50\tau$ are considered to have a sufficient number of independent samples [58]. The τ values for each Cepheid can be found in Table 8 (Appendix).

The highest value of τ observed was 153.6. This motivates the choice of 10,000 steps for production runs as sufficient to produce enough independent samples. The number of independent samples is

also correlated with the number of walkers. It is recommended to have at least twice as many walkers as parameters, while the only upper constraint on the number of walkers is computational performance [56]; more walkers also allows a more comprehensive exploration of parameter space. This motivated the choice of 100 walkers for both the burn-in and production run.

The resulting chain encodes information about the parameters along with their associated uncertainties. Fig. 21 is a visual representation of one such chain: the clustering of the walkers around a central value indicates convergence.

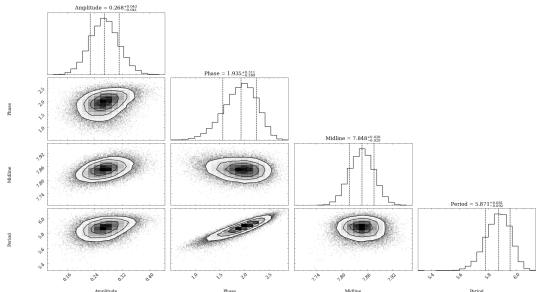


Figure 22: The corner plot of posterior spread of MW Cyg. The one-dimensional plots demonstrate the marginalised distribution of each parameter; the two-dimensional plots demonstrate the covariance between parameters. Covariant parameters will have skewed projections. This is evident in the period-phase relationship.

The distribution of each parameter can be extracted from the chain (Fig. 22). Inferring the values of each parameter thus comes from straightforward analysis of the distribution. Herein lies an advantage of MCMC methods: highly-accurate uncertainties may also be inferred from the posterior. These uncertainties also capture any skewness of the distribution. Uncertainties were quoted at the 68% credible interval, corresponding to a $1-\sigma$ Gaussian error. The median of the posterior distribution is quoted as the best-fit value as this summarises the central tendency of the distribution.

Figs. 20 & 22 demonstrate the robust model fitting algorithm.

P-L SELECTION CRITERIA

Hitherto we have described data analysis which was applied to all Cepheids. However, before fitting the P-L relation, it was important to apply selection criteria to the Cepheids to ensure a well-calibrated relation: each Cepheid was appropriately interrogated. Due to the limited sample size, the selection criteria were conservative.

It was identified during observing nights that DL Cassiopeiae and V636 Cassiopeiae were heavily saturated, even at the minimum t_{exp} . For DL Cassiopeiae heavy saturation limited the choice of reference stars to targets which did not adequately sample the quadrants of the image. On this basis these Cepheids were flagged during observation nights as almost certainly unusable. The period fitting confirmed this: the χ^2_v values indicated extreme overfitting. The τ values were notably high, indicating poor convergence (Table 8). This is further illustrated by the parameter time series and posterior spread plots (see Appendix). DL Cassiopeiae and V636 Cassiopeiae were consequently excluded from the P-L relation.

Saturation was also observed and flagged in the case of Z Lacertae; it was comparably less severe than the aforementioned cases, and restricted to four observations. On this basis Z Lacertae was flagged as likely unusable. The diagnostic parameter time series and posterior spread (see Appendix) did not support its inclusion. Furthermore, the residuals in its fit displayed a sinusoidal pattern. This is indicative of a systematic error in the data, attributed to the saturation being more severe than originally thought. Z Lacertae was subsequently excluded from the P-L

relation.

V Lacertae was not flagged during observation nights. During period fitting, the very high χ^2_v value of 5.537 indicated an unusually-poor fit, which was noted. Though the value of τ and diagnostic plots indicated the MCMC fit had converged, a trial run of the P-L fitting with residuals revealed V Lacertae was an anomaly, lying beyond 2σ of the fit. On the basis of the poor χ^2_v value and P-L residuals indicating it was anomalous, its images were re-inspected. This revealed unnoticed minor saturation on three nights. It was decided that the removal of these nights would leave too few remaining data points for a reliable fit. V Lacertae was then excluded from the P-L relation: a subsequent trial run concluded its removal improved the quality of the fit.

CP Cephei was flagged when reviewing literature distance measurements to the Cepheids. Its measured distance varies significantly in literature: values are quoted from 3667 pc [59, 60, 61] to 4208 pc. Furthermore, the parallax distance catalogue from which the literature distance measurements were used [26] delivers a significant correction to the Gaia DR3 parallax, adjusting the initial estimate of $3946.33^{+317.7}_{-317.7}$ pc to $3641.318^{+218.887}_{-60.541}$ pc. This was a correction of 8%, notably higher than the parallax correction to the other Cepheids. On this basis, it was decided the distance measurements to CP Cephei were unreliable, and it was thus excluded from the P-L relation.

After selection criteria were applied, the data of 6 Cepheids were deemed of sufficient quality to be used in the P-L fitting. Issues with these Cepheids were noted; however, the already-limited data made the justification of further omission difficult (see Discussion).

MCMC: P-L RELATION

The P-L relation was constructed using a hierarchical Bayesian inference model. Rather than taking the period of each Cepheid and its associated uncertainty as a fixed point estimate, the posterior samples were resampled directly into the P-L fitting from the stored chains. Herein lies another advantage of MCMC methods over a frequentist approach: the full posterior distribution of each Cepheid propagates into the P-L fitting. This fully propagates parameter correlations, asymmetries and uncertainties.

The P-L relation is a function of form:

$$M_V = a(\log_{10}(P) - 1) + b \quad (16)$$

where M_V represents the absolute V-band magnitude and P represents the period of a Cepheid; a represents the slope, and b represents the zero point. The model also incorporated a scatter parameter σ as a means of quantifying the individual differences between Cepheids that arise due to aforementioned factors such as metallicity.

The MCMC model for the P-L relation followed a similar structure to that of the period fitting. The key difference is the model was now hierarchical, meaning the period-fitting models of each Cepheid would combine to construct the P-L relation. Each Cepheid provides a contribution to the likelihood of the form in Eq. 17:

$$\ln(\mathcal{L}_i) = \ln\left(\frac{1}{N_S} \sum_j^{N_S} \mathcal{L}(a, b, \sigma \mid P_j, M_j)\right) \quad (17)$$

where \mathcal{L} represents the contribution of Cepheid i to the likelihood; N_S is the number of posterior samples; and P_j, M_j are the j^{th} resampled posterior sample of period and absolute magnitude from the chain of Cepheid i .

The full likelihood is thus the contribution from each Cepheid as in Eq. 18.

$$\ln(\mathcal{L}_{tot}) = \sum_i^{N_C} \ln(\mathcal{L}_i) \quad (18)$$

Where N_C is the number of Cepheids. In practice these likelihoods were computed in log-space for numerical stability (as in Eq. 15).

As demonstrated in Eq. 17, the model marginalises over the posterior samples for each Cepheid. Herein lies another benefit of the hierarchical model: Cepheids with more well-converged chains and thus more tightly-constrained posterior samples will contribute more strongly to the overall likelihood. This means each Cepheid has an automatically-weighted contribution to the overall P-L relation.

The chain of the P-L relation was also stored for use with M31 CV1.

ANDROMEDA

M31 CV1 was fit using the same period-fitting algorithm described for the other Cepheids. Its chain was also stored: to place M31 CV1 onto the P-L relation, its posterior P samples were randomly resampled from its chain in conjunction with the posterior a, b, σ samples from the P-L chain to compute M_V samples according to Eq. 16. The distance modulus equation (Eq. 1) converted these to distance samples from which the distance to Andromeda and its uncertainty were inferred. The best-fit value was quoted as the median and $1-\sigma, 2-\sigma$ errors as 68% and 95% credible intervals respectively, in accordance with the convention in the period fitting.

RESULTS

INITIALISATION

Cepheid	Model	χ^2_v
01 MW Cygni	Sinusoid	3.061
02 V520 Cygni	Sinusoid	1.452
03 VX Cygni	Sawtooth	0.430
04 VY Cygni	Sawtooth	0.407
05 CP Cephei	Sawtooth	0.346
06 Z Lacertae	Sinusoid	0.845
07 V Lacertae	Sinusoid	5.537
08 SW Cassiopeiae	Sinusoid	0.595
09 TU Cassiopeiae	Sawtooth	1.458
10 DL Cassiopeiae	Sawtooth	0.103
11 V636 Cassiopeiae	Sinusoid	0.021

Table 2: The model used for each Cepheid along with its corresponding χ^2_v value.

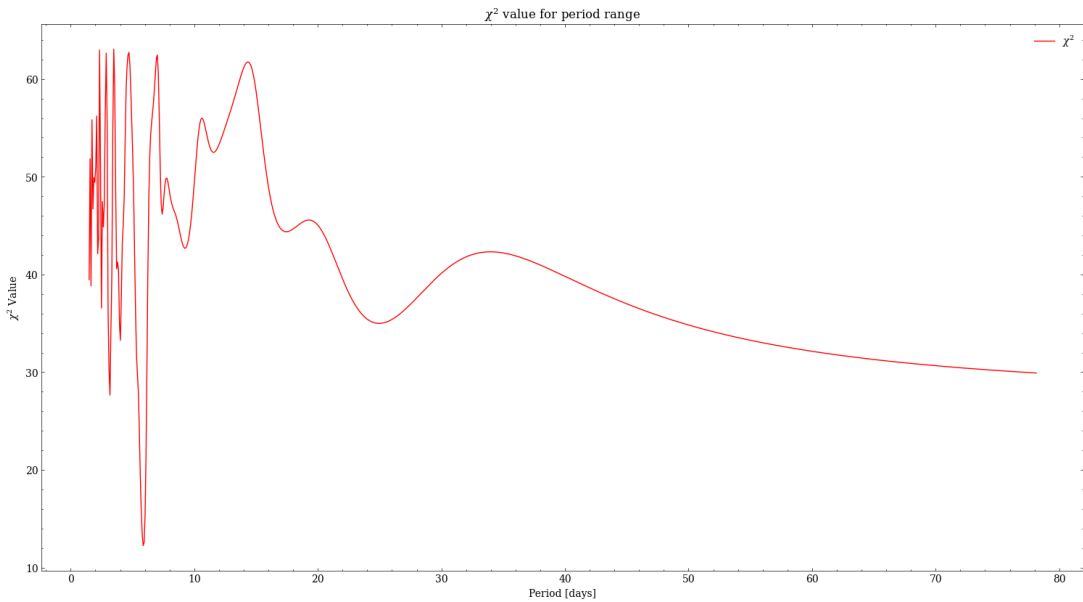


Figure 23: The χ^2 grid search for MW Cygni with the sinusoid model (literature period: 5.95 days [23]).

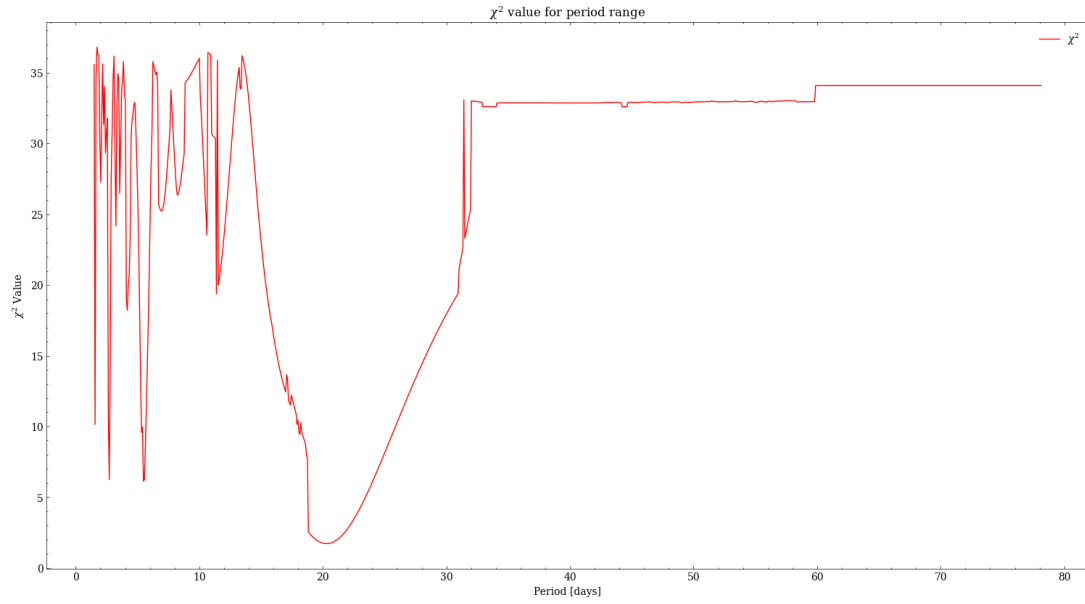


Figure 24: The χ^2 grid search for VX Cygni with the sawtooth model (literature period: 20.13 days [23]).

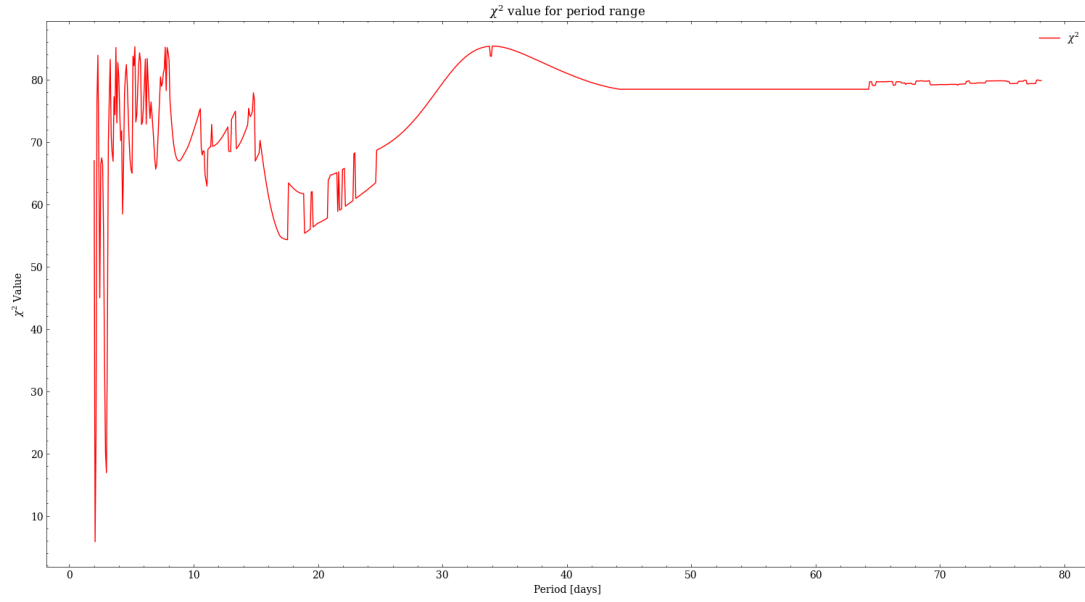


Figure 25: The χ^2 grid search for TU Cassiopeiae with the sawtooth model (literature period: 2.14 days [24]).

MCMC MODEL FITTING

Cepheid	P [days]	Literature P [days]
01 MW Cygni	$5.871^{+0.081}_{-0.092}$	5.954
02 V520 Cygni	$4.049^{+0.039}_{-0.059}$	4.049
03 VX Cygni	$20.296^{+1.187}_{-1.197}$	20.133
04 VY Cygni	$7.941^{+0.288}_{-0.201}$	7.856
05 CP Cephei	$17.370^{+0.887}_{-1.009}$	17.859
06 Z Lacertae	$10.693^{+0.114}_{-0.127}$	10.886
07 V Lacertae	$4.617^{+0.039}_{-0.031}$	4.983
08 SW Cassiopeiae	$5.346^{+0.099}_{-0.088}$	5.44
09 TU Cassiopeiae	$2.151^{+0.014}_{-0.017}$	2.139
10 DL Cassiopeiae	$8.175^{+0.559}_{-0.509}$	8.001
11 V636 Cassiopeiae	$8.984^{+0.634}_{-0.605}$	8.377

Table 3: The best-fit period values for each cepheid, taken as the median of the posterior, compared to their literature values [23]. Cepheids that would later be omitted from the P-L calibration are highlighted in grey.

Cepheid	m_V	Literature m_V	A	Literature A
01 MW Cygni	$7.848^{+0.028}_{-0.029}$	9.489	$0.268^{+0.043}_{-0.041}$	0.719
02 V520 Cygni	$8.832^{+0.044}_{-0.046}$	10.851	$0.272^{+0.028}_{-0.029}$	0.636
03 VX Cygni	$8.104^{+0.054}_{-0.053}$	10.069	$0.568^{+0.104}_{-0.104}$	1.043
04 VY Cygni	$7.889^{+0.071}_{-0.070}$	9.593	$0.448^{+0.096}_{-0.094}$	0.81
05 CP Cephei	$9.139^{+0.052}_{-0.053}$	10.59	$0.483^{+0.098}_{-0.097}$	0.74
06 Z Lacertae	$7.507^{+0.023}_{-0.023}$	8.415	$0.45^{+0.045}_{-0.044}$	0.968
07 V Lacertae	$8.109^{+0.024}_{-0.024}$	8.936	$0.554^{+0.039}_{-0.038}$	0.94
08 SW Cassiopeiae	$8.534^{+0.046}_{-0.046}$	9.705	$0.328^{+0.058}_{-0.058}$	0.662
09 TU Cassiopeiae	$7.560^{+0.032}_{-0.032}$	7.733	$0.417^{+0.065}_{-0.062}$	0.553
10 DL Cassiopeiae	$7.511^{+0.080}_{-0.087}$	8.969	$0.327^{+0.268}_{-0.126}$	0.571
11 V636 Cassiopeiae	$5.29^{+0.072}_{-0.071}$	7.199	$0.188^{+0.075}_{-0.055}$	0.188

Table 4: The best-fit m_V values, quoted as the median of the midline posterior, and the best-fit magnitude variations, quoted as the median amplitude posterior, compared to their literature values [23].

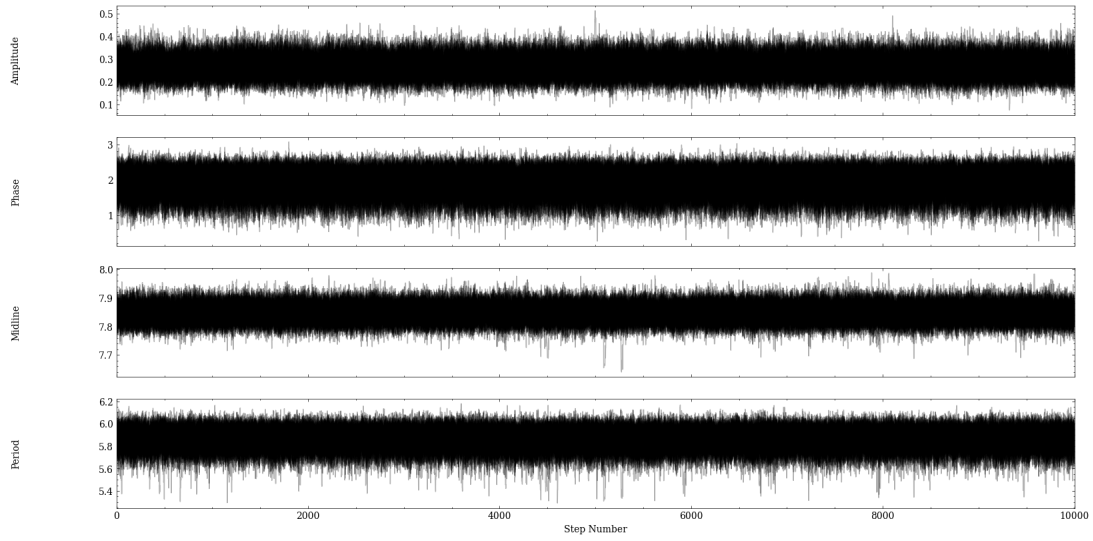


Figure 26: The parameter time series of MW Cygni.

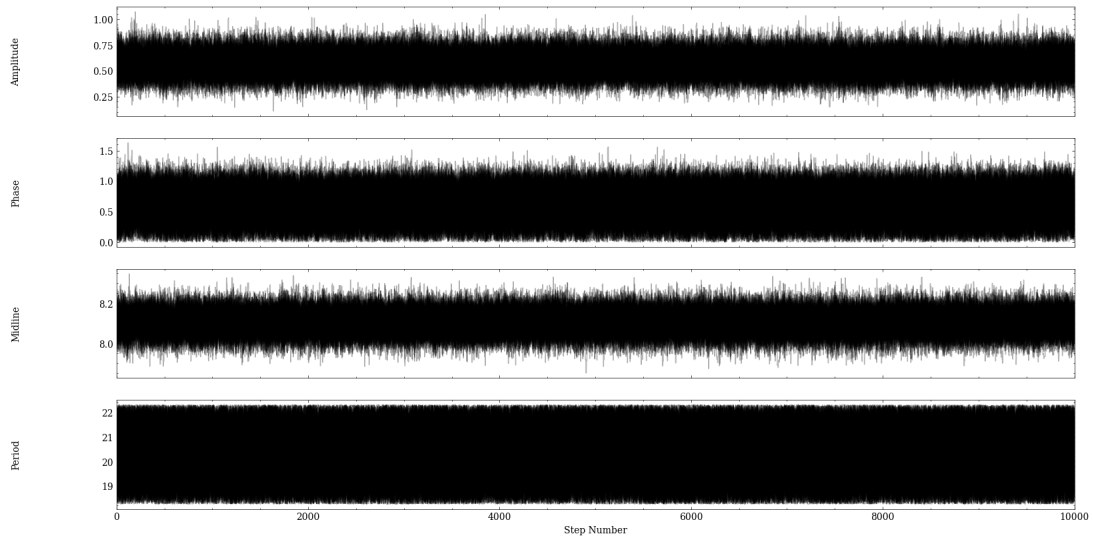


Figure 27: The parameter time series of VX Cygni.

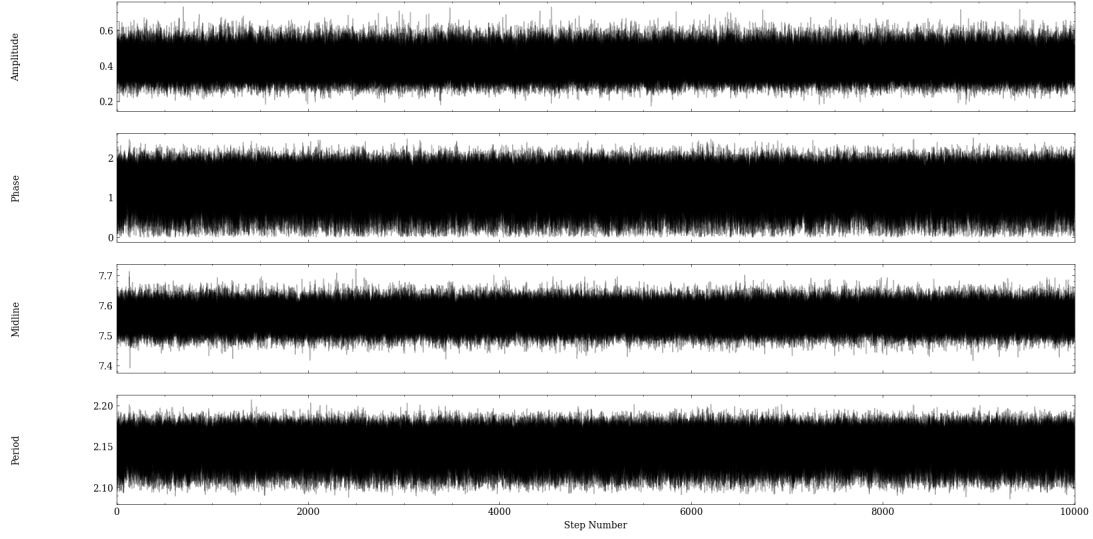


Figure 28: The parameter time series of TU Cassiopeiae.

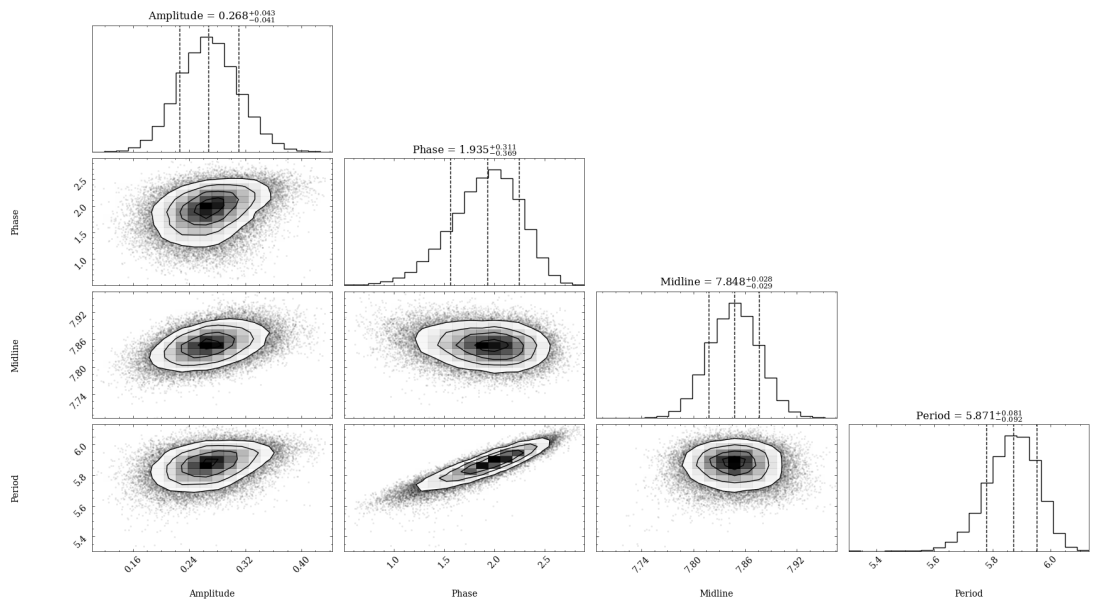


Figure 29: The posterior spread of MW Cygni.

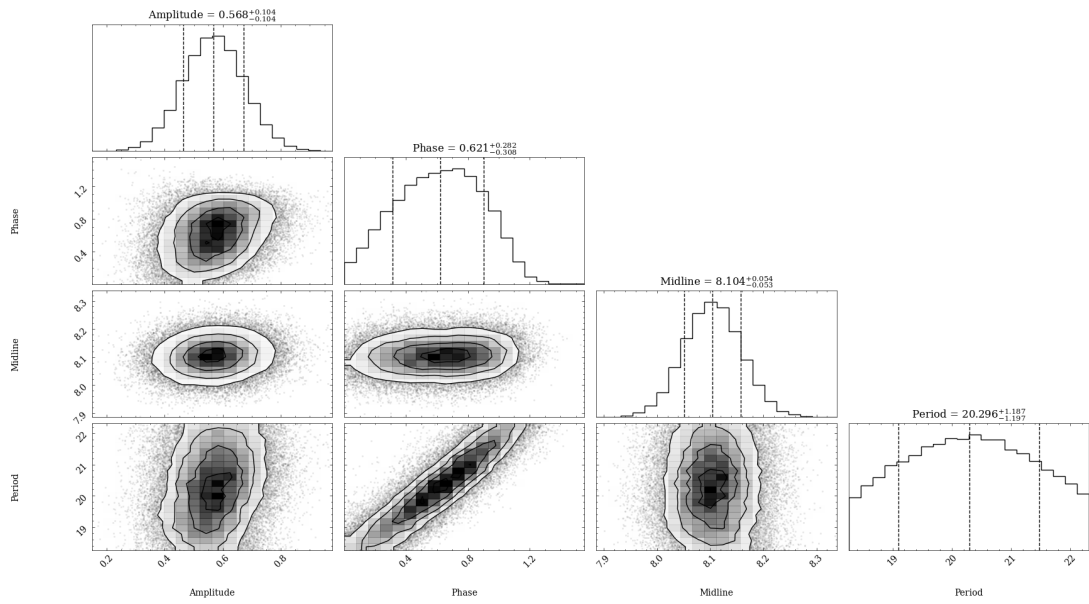


Figure 30: The posterior spread of VX Cygni.

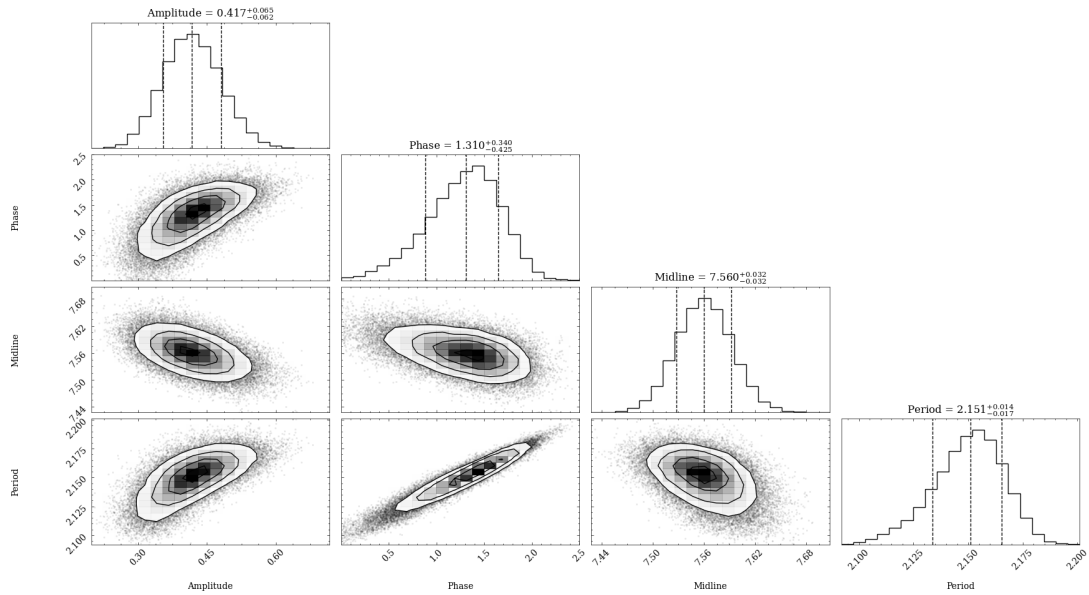


Figure 31: The posterior spread of TU Cassiopeiae.

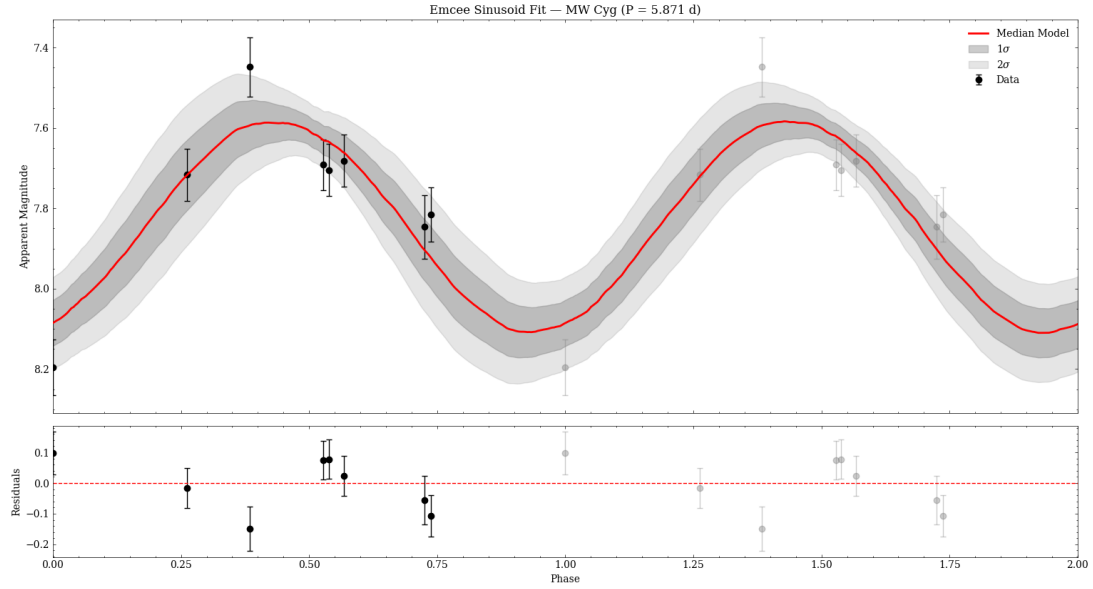


Figure 32: The sinusoid fit to MW Cygni.

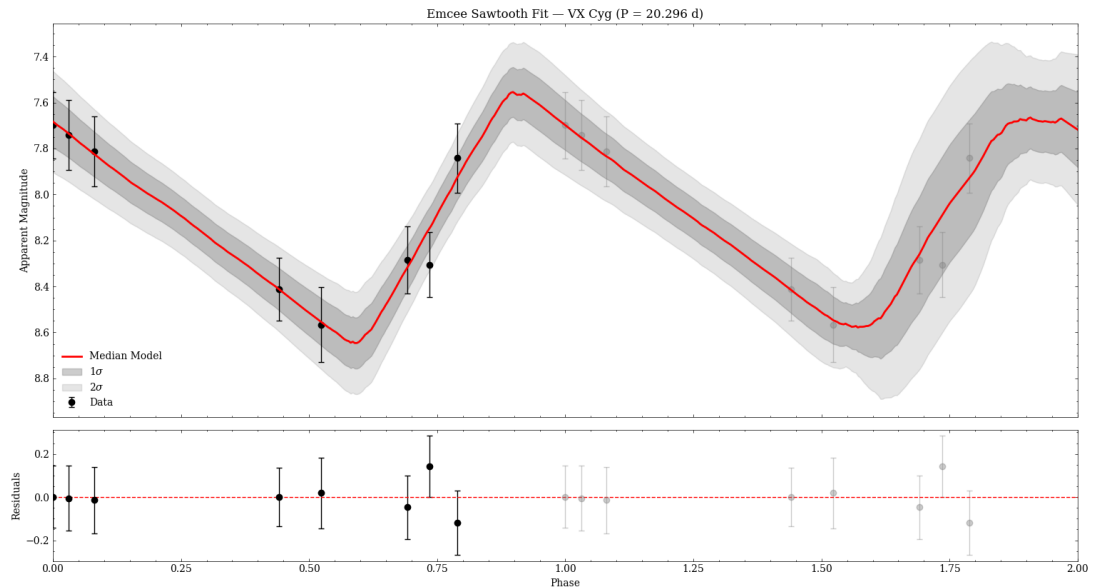


Figure 33: The sawtooth fit to VX Cygni.

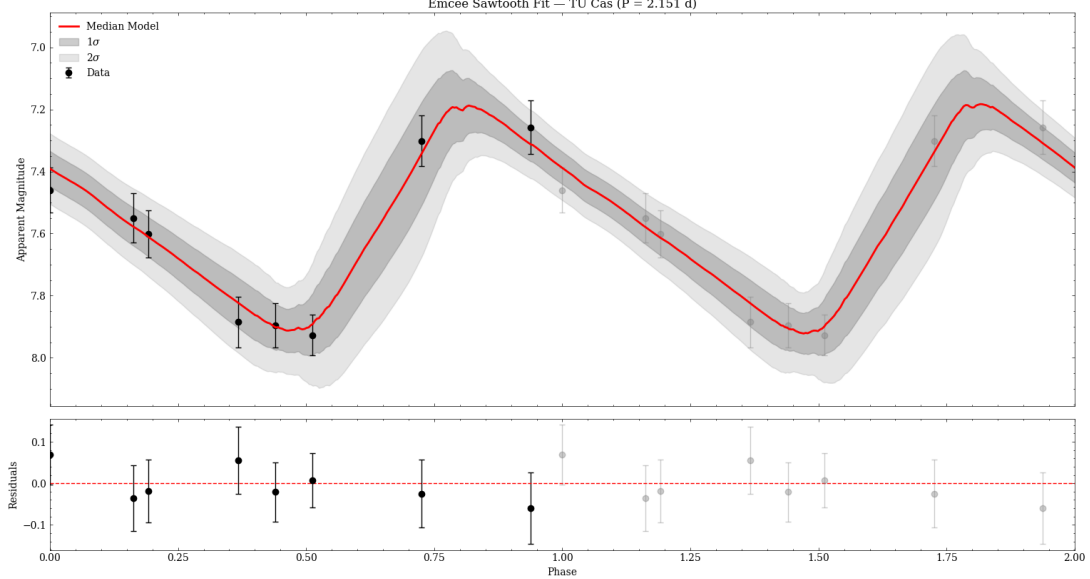


Figure 34: The sawtooth fit to TU Cassiopeiae.

We present a demonstration of the model fitting results on three Cepheids which were chosen as a representative sample. MW Cygni, which was fit with a sinusoid; VX Cygni, which had the longest period and was fit with a sawtooth; and TU Cassiopeiae, which had the shortest period and was fit with a sawtooth.

Figs. 23, 24, 25 demonstrate the χ^2 grid search to determine the initial guess. For all Cepheids, the initial-guess period was close to literature values. The model used for each Cepheid and its corresponding χ^2 value are displayed in Table 2.

Figs. 26, 27, 28 demonstrate param-

ter time series, the visual representations of the Markov Chain. Of the Cepheids used in the P-L relation, the maximum observed autocorrelation time τ was 100.2 for VX Cygni; $\tau \approx 50$ for other Cepheids. This supports the choice of 10,000 steps for each Cepheid chain.

Figs. 26, 27, 31 demonstrate posterior spreads. There is an evident correlation between period and phase.

Table 3 demonstrates the results of the MCMC model fitting for the period values, while Table 4 demonstrates the results for the apparent V-band magnitudes and light curve amplitudes.

P-L RELATION

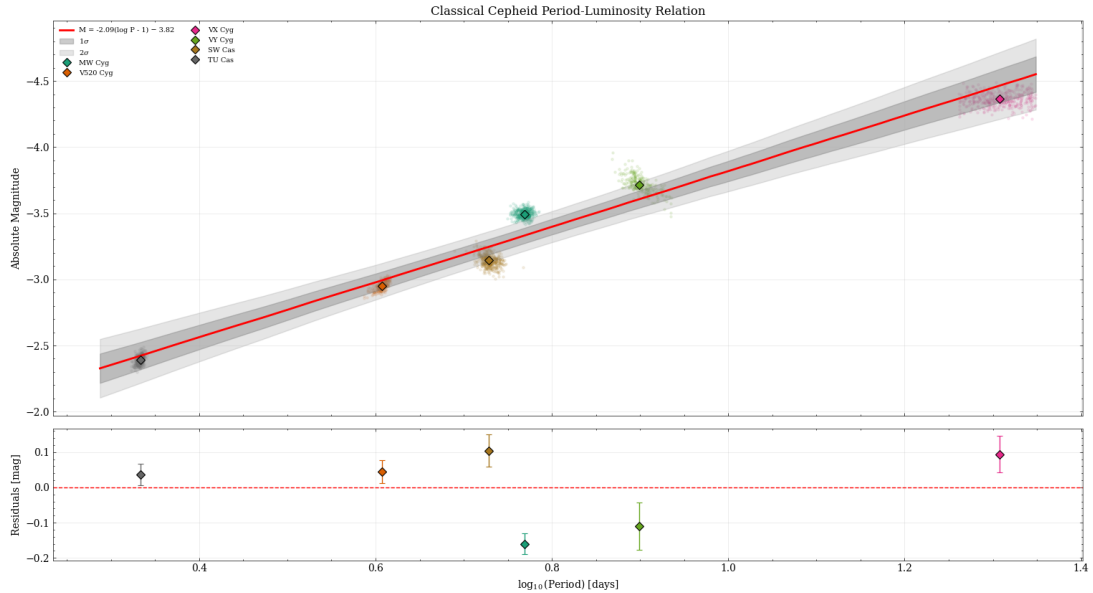


Figure 35: The P-L relation for six classical Cepheids.

$$M_V = -2.087_{-0.183}^{+0.191} (\log_{10}(P) - 1) - 3.817_{-0.071}^{+0.072} \quad (19)$$

with $\sigma = 0.118_{-0.039}^{+0.064}$

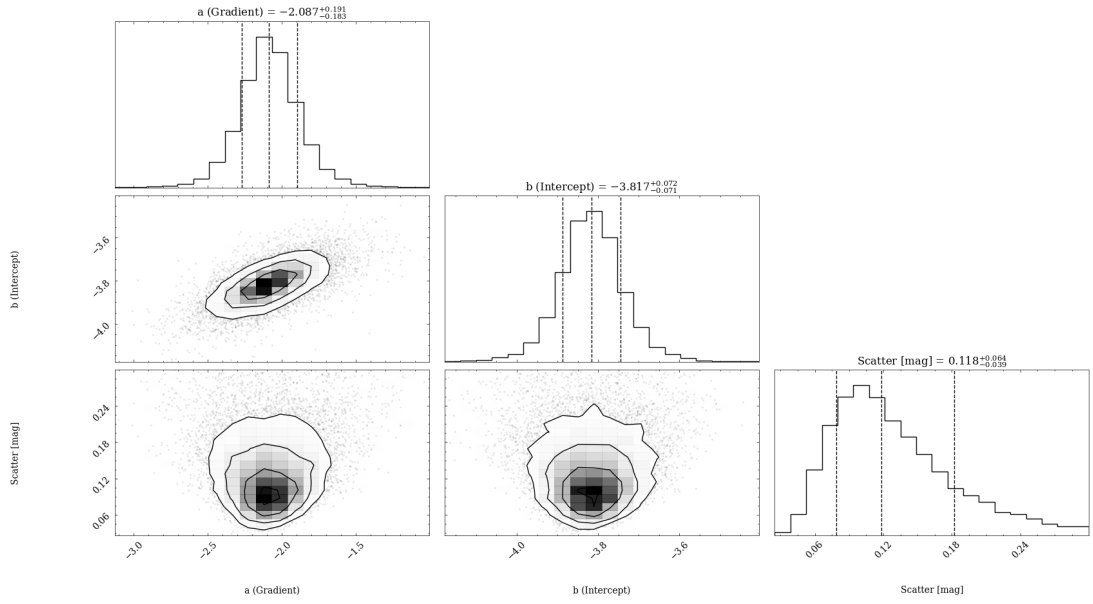


Figure 36: The posterior spread of the P-L relation.

After careful consideration of factors affecting the fit of each Cepheid (see Discussion), five Cepheids were omitted from the P-L relation. The calibrated relation is shown in Fig. 35; the posterior samples are visualised as a 'cloud' to demonstrate the resampling employed by the hierarchical model.

The functional form of the P-L model is shown in Eq. 19. We contrast this with the value obtained in literature (Eq. 20) [1].

$$M_V = -2.43 \pm 0.12 (\log_{10}(P) - 1) - 4.05 \pm 0.02 \quad (20)$$

The literature value of the slope a is within the 95% credible interval (2σ) of the obtained best-fit value; the literature zero point b is within the 99% credible interval (3σ) of the obtained best-fit value.

The scatter in the V-band observed in literature is usually found to be $\sigma \approx 0.25$ mag [62, 16, 63], a significant difference from the obtained best-fit value of $0.118^{+0.064}_{-0.039}$.

ANDROMEDA

P [days]	m_V	A	$B - V$	χ^2_V
$32.328^{+0.554}_{-0.510}$	$19.401^{+0.067}_{-0.067}$	$1.466^{+0.101}_{-0.103}$	1.28	11.352

Table 5: The best-fit values of M31 CV1, the Cepheid in the Andromeda Galaxy. Its period P in literature is 31.401 days [64]. Due to insufficient data the value of $B - V$ used was quoted from literature [47].

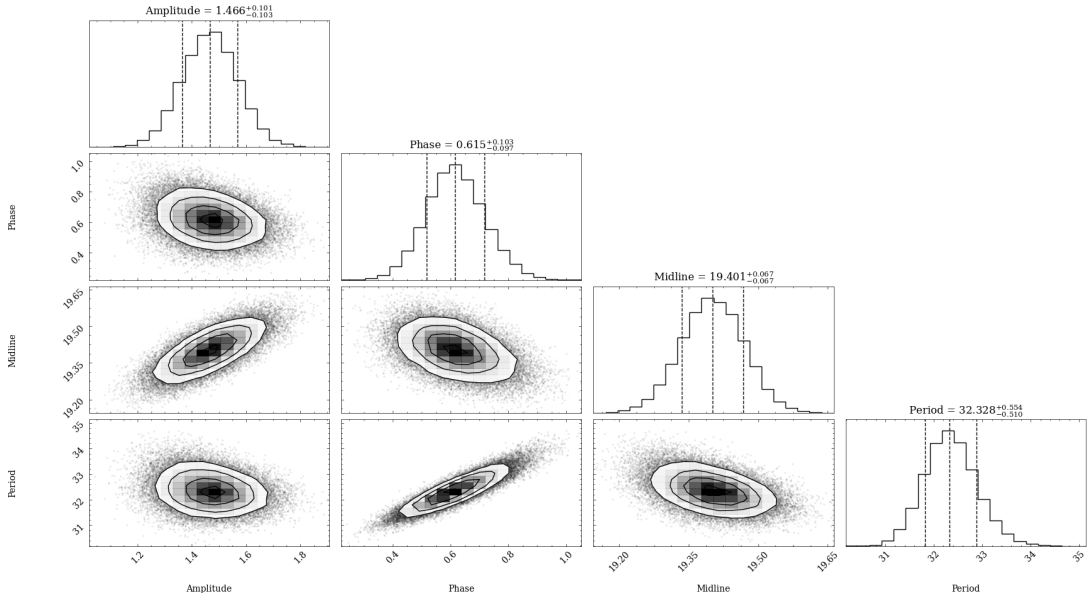


Figure 37: The posterior spread of M31 CV1.

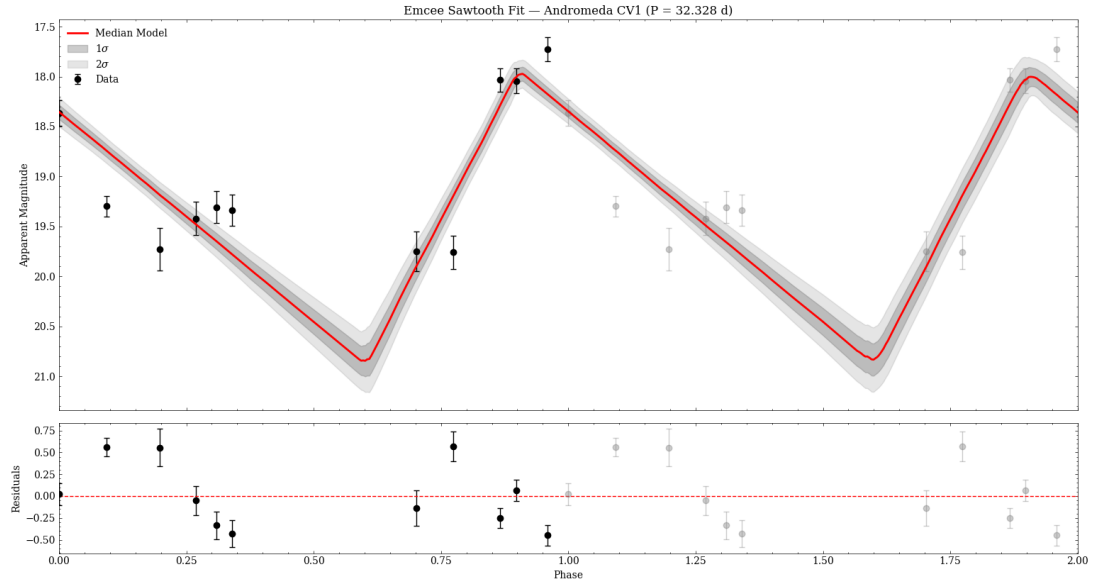


Figure 38: The sawtooth fit to M31 CV1.

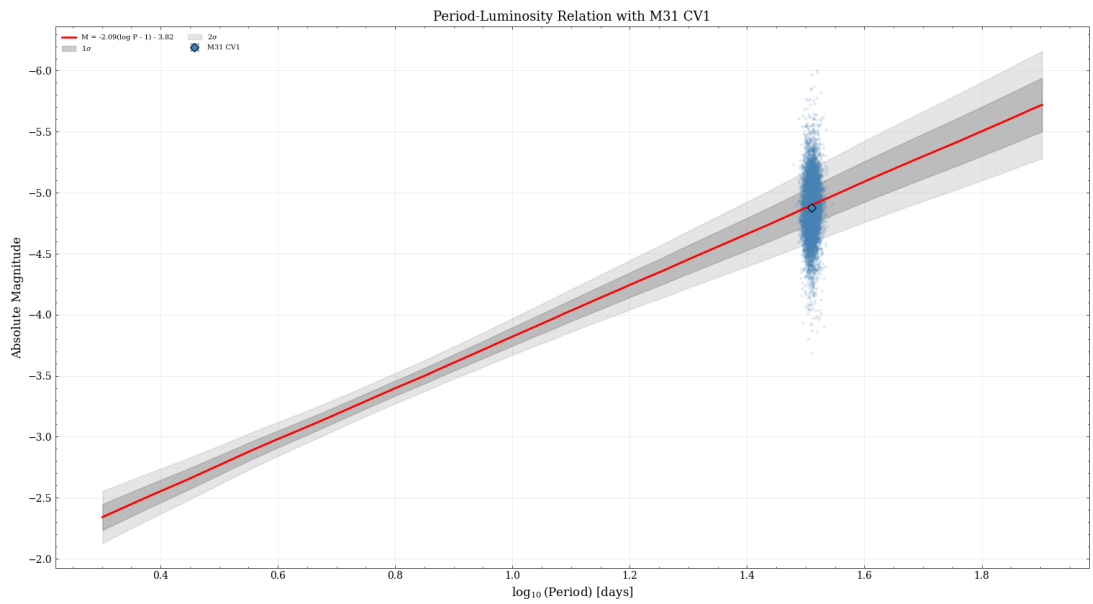


Figure 39: The posterior samples of M31 CV1 placed onto the calibrated P-L relation.

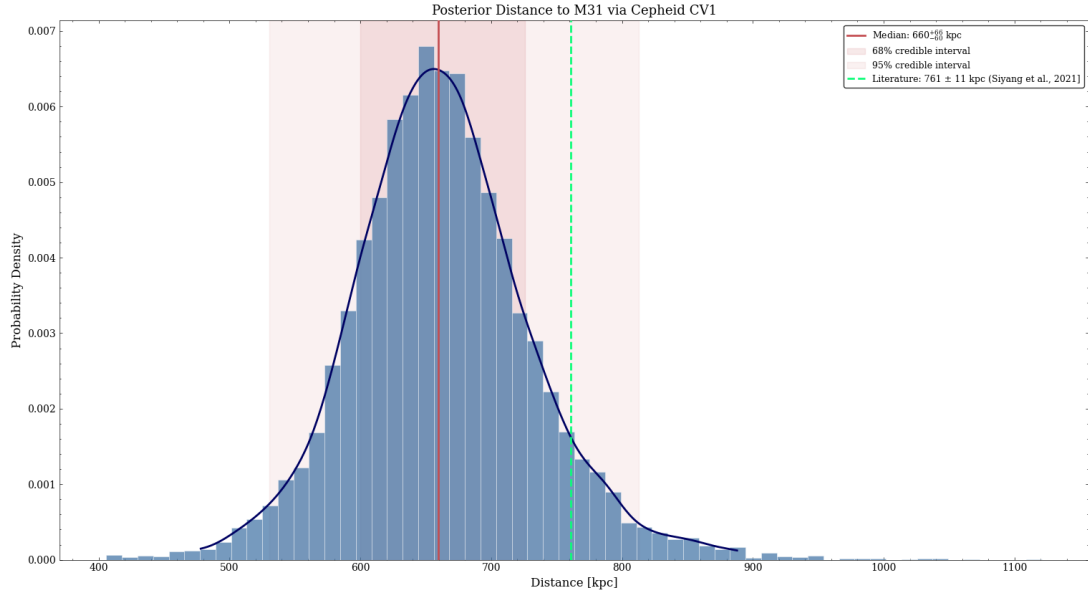


Figure 40: The posterior distance estimate of M31 CV1, with the literature value of 761 ± 11 kpc marked [2].

$$D = 660^{+66}_{-60} \text{ kpc} \quad (21)$$

The best-fit values for the parameters of M31 CV1 are shown in Table 5. The literature value of P (31.401 days [64]) was within the 95% credible interval (2σ) of the median posterior estimate, which was longer at $32.328^{+0.554}_{-0.510}$. The posterior spread of the parameters of M31 CV1 are displayed in Fig. 37; it is evident the fit has converged. The final best-fit model is shown in Fig. 38.

The position of M31 CV1 on the calibrated P-L relation is shown in Fig. 39; its overestimated period would consequently

cause its absolute magnitude and thus distance to be overestimated (Eqs. 16, 1). The corresponding distribution of the distance modulus μ posterior samples is then shown in Fig. 40.

The literature value for the distance to the Andromeda Galaxy of 761 ± 11 kpc, which was also derived from P-L relations [2], is within the 95% credible interval of the posterior distance estimate of 660^{+66}_{-60} kpc. The obtained distance measurement is notably closer.

DISCUSSION

As Cepheids are intrinsically extremely luminous, they appear bright even for ground-based observations at distances on the order of kiloparsecs. This posed a challenge during the observation period.

In observational astronomy, it is preferable to ensure the noise on images is background-limited, where the SNR increases as $\sqrt{t_{exp}}$ (see Eq. 23). As the background-limited regime normally corresponds with long exposure times, the signal-to-noise ratio is normally high.

In contrast, it is preferable to avoid the noise being dominated by exposure-time-independent read noise, because this regime correlates with short exposure time, thus normally results in a low signal-to-noise ratio (see Eq. 22).

$$SNR \approx \frac{N_* t_{exp}}{\sqrt{n_{pix}(1 + \frac{n_{pix}}{n_B})N_R^2}} \quad (22)$$

$$SNR \approx \frac{N_*}{\sqrt{n_{pix}(1 + \frac{n_{pix}}{n_b})N_S}} \sqrt{t_{exp}} \quad (23)$$

In order to avoid entering the read-noise-limited regime, the minimum t_{exp} used during observations was 3s. Some of the targets would saturate the detector even at this exposure time.

The unavoidably-short exposure times posed a problem for the image reduction. The median counts of the master bias frames was close to the sky background of the raw science images: consequently, almost no sky signal remained following background subtraction. Diagnostic tests on science images revealed $\sim 20\%$ of pixel values to be negative, and the error to be dominated by the read-noise term. The metadata of the bias frames were inspected and it was confirmed they were also im-

aged at -30°C , ruling out the possibility of an error inherent to the bias frames. This confirmed images were significantly read-noise dominated.

Due to the very small sky backgrounds left (of around 5 counts) after the bias subtraction, coupled with the fact the CCD itself has a relatively high read-noise of 14.0 electrons per pixel (c.f. a medium read-noise of ~ 5 electrons per pixel [30]), the photometry of the targets was highly read noise dominated, with read noise contributions being on the order of 10^2 times larger than background contributions. The exposures were also inspected for their source noise in case they were source-limited (see Eq. 24). As the Cepheids are generally bright objects, the source noise can contribute a larger fraction of the overall noise. Still, the read noise exceeded the source noise, concluding that the observations are read noise dominated.

$$SNR \approx \sqrt{N_* t_{exp}} \quad (24)$$

Another error in the image reduction came from the orientation of the exposures. The correction for 180° -flipped images was applied during photometry; however, the flat and bias frames also had defined orientations. While the bias frames were mostly uniform, the flat frames would not have properly corrected for the pixel-to-pixel variations when applied to images of a different orientation. The images should have been aligned with respect to a defined reference orientation during reduction to prevent this occurrence.

Both the missing sky signal and misaligned calibration frames introduced sys-

tematic errors into the data at the beginning of the analysis. The missing sky signal was the more culpable of the two errors: the sky background was significantly underestimated in the science frames, which artificially brightened the Cepheids. This is reflected in their m_V values being systematically too bright and their amplitudes A being comparatively low compared to literature. The effect of this systematic error would depend on the t_{exp} values for each Cepheid: targets with lower t_{exp} values would feel a more pronounced effect. The standard stars required longer exposures of $t_{exp} \approx 30$ s and so this systematic error was limited to the galactic Cepheids.

This error did not only represent a t_{exp} -dependent offset between each Cepheid, but also between the data points for the individual Cepheids. This is because t_{exp} varied between nights depending on the observing conditions.

The assumption of the Poissonian sky background is generally an oversimplification, as objects such as faint background sources and the extremities of the target's PSF contribute additional terms to the actual sky-background [65]. However, sigma-clipping the sky annulus removed some of these non-Poissonian sources such as background targets. The PSF extremities of the target and other nearby field objects in the sky annuli would contribute a systematic error to the sky-background. However, even with this systematic increase, the noise of the exposures was still dominated by read-noise. Therefore, the Poissonian assumption did not have a significant effect on the instrumental magnitude error.

The global atmospheric extinction and zero point calibration established a single, consistent photometric scale across the dataset rather than correcting night-

to-night variations explicitly. By adopting a global extinction coefficient and zero point, the calibration accounted for the mean atmospheric attenuation and instrumental response across the whole observation period. This decision is not without consequences: while per-night calibration is more true to the conditions of the night, the fit is sensitive to the limited number of data points and can thus be inaccurate. The global calibration resolves this, but at the same time, is impacted by the inherent night-to-night scatter. This is evident in the large scatter observed in Fig. 11. The global calibration was primarily justified by the missing standard star exposures on the supplementary observing epochs. This meant per-night calibration was not possible, and it was decided the discussed benefits of a global calibration were preferable to mapping the calibration of an adjacent epoch to one with no standard star observations. Furthermore, the differential photometry partially-absorbed the night-to-night variations, correcting for the scatter in the global calibration.

The interstellar dust extinction correction also may introduce an additional systematic uncertainty through the assumption of a standard extinction law with $R_V = 3.1$. While this assumption is well motivated for diffuse interstellar environments, variations in dust properties can lead to small offsets in the corrected magnitudes. These uncertainties affect the zero point of the period-luminosity relation, which propagates to the inferred distance, but do not influence the measured periods or the relative shape of the Cepheid light curves.

The comprehensive diagnostics employed during photometry ensured the methodology was being performed correctly. The same systematic trends were observed in the reference star magnitudes of each Cepheid; this instilled confidence

that the normalisation was correct such that the intrinsic brightness variations of the Cepheid were being measured as opposed to night-to-night systematic variations.

The period fitting was limited by the small number of data points and narrow observing window compared to those found in literature. The HST Key Project to measure the Hubble Constant conducted observations of Cepheids at 12 epochs spread over a 2-month window. The observations for each Cepheid were spaced according to a power law, and an additional observation was taken one year before or after the 2-month window, steps which reduced aliasing whilst increasing time coverage [9]. By contrast, our observations were conducted during a 6-week window and spaced according to availability: each Cepheid had 8 data points on average.

Consequently, the χ^2_v values (Table 2) and the residuals of the final fits (see Appendix) demonstrate the data were overfitted in most cases, indicating the model was also capturing the noise in the data. It is important to have comprehensive phase coverage to fully profile the light curve. The spacing of observations meant phase coverage varied between Cepheids: the number of cycles the observing window covered is dependent on the period of each Cepheid. This is evident in the fit to TU Cassiopeiae, the shortest-period Cepheid, which completed the most cycles and had its phase well-covered. It is also worth noting the aforementioned underestimated sky background, the effect of which varied between nights.

Another consequence of the limited data available was the increased tolerance to poorer data. To preserve phase coverage it became harder to justify removing data points except in the case of clear outliers.

The reliability of results would be improved with more epochs to tighten exclusion criteria.

The simplicity of the model fitting must also be acknowledged. Cepheid light curves are complex and require a thorough examination: in literature, the light curves are described by custom templates [66] that employ more complex methods such as principal component analysis [67]. These templates allow rigorous determination of the parameters from a limited number of data points. Our model fitting measures period from successive maxima in the light curve. This can be considered a naïve assumption, as the aforementioned 'bump' Cepheids can appear to have two peaks [21] due to the bump on their light curves. Furthermore, the model fitting does not take into account the pulsation modes of each Cepheid: this is most relevant for TU Cassiopeiae as it pulsates in two modes [24]. TU Cassiopeiae is, however, the only P-L relation Cepheid to exhibit such behaviour.

The limited number of Cepheids led the selection criteria to be conservative. In addition to the 5 omissions, specific issues were noted with 3 remaining Cepheids.

VX Cygni was observed to have a similarly-significant correction to its DR3 parallax. However, the correction brought its distance measurement in line with previous measurements in literature [60, 59, 61]. Furthermore, VX Cygni was the longest-period Cepheid and was consequently crucial in constraining the slope of the relation. This justified its inclusion.

VY Cygni was observed to have an unusually-high τ of 100.2 and its posterior spread indicated it was less-well converged. This is attributed to the limited phase coverage of its light curve (see Appendix). Though its residuals indicate one spurious data point, this data point was

also crucial in constraining the shape of the light curve and was thus included.

TU Cassiopeiae was well-fit but nonetheless examined on grounds of its unusually-low metallicity [68] and status as a beat Cepheid [24]. However, as the shortest-period Cepheid, it was important in constraining the slope of the relation: furthermore, as M31 CV1 is similarly metal-poor, it was decided TU Cassiopeiae should be included nonetheless.

P-L relation trial fits were run with the 3 above Cepheids. From examination of the resulting fits and residuals, omission of the above three Cepheids could not be justified.

The problem of overfitting is again posed with respect to the P-L relation, which was highly sensitive to the variations between its 6 individual Cepheids. This is indicated by the distribution of its residuals, which indicates its uncertainties were underestimated. More Cepheids would smooth out the scatter and provide a more representative population sample. We again refer to the HST Key Project as an example in literature, which used as many as 94 Cepheids in a galaxy to calibrate a P-L relation [9]. The underestimation of σ by the model can be explained by the model incorporating noise into its fit.

The previously-discussed systematic magnitude error introduced by the read-noise-limited images was t_{exp} dependent. It would cause the zero point b to become more negative as the Cepheids were systematically too bright, contrary to the obtained result; however, t_{exp} dependence would also offset the slope a , and diagnosing the effect of this is complex.

It is well-established in literature that the brightness of Cepheids is metallicity-dependent [69]: metal-rich Cepheids are brighter for a given period [70]. Though most of our Cepheids have similar metal-

licity values (Table 7), the notable exception to the general trend of our Cepheids is once again TU Cassiopeiae: this Cepheid is comparatively unusually metal-poor [68].

It is also well-established that the P-L relation depends on the instability strip (the period-colour relation) which is specific to the H-R diagram of a given Cepheid population [71].

The variation between Cepheids is absorbed to some degree by the scatter parameter σ : however, σ captures random scatter and does not account for the systematic trend in metallicity and colour. More reliable results would require a rigorous metallicity and colour correction.

The g-band to V-band transformation was derived from an empirical fit of Landolt standard stars with an R-I colour of < 1.15 . There was not sufficient photometry of $R - I > 1.15$ stars to derive an equivalent transformation [46]. Because no R- or I-filter observations were taken of M31 CV1, the validity of the transformation was not verified, but assumed to be true, based on literature to suggest that $R - I < 1$ for most Cepheid variables [72].

Furthermore, the filter transformation relied on the assumption that the literature derived B-V colour of M31 CV1 was constant with time and thus, applicable to all nights. This is an inaccurate assumption, as the colour of Cepheids does oscillate with pulsations, similarly to their luminosities [72, 73, 74]. However, it was impossible to accurately compute the night-to-night colour variation of M31 CV1 because data were only supplied in one filter. From Eq. 10, r-band observations would need to have accompanied the g-band observations to allow an independent colour estimation.

M31 CV1 is extremely metal-poor [75]. Since more metal-poor Cepheids appear

fainter, M31 CV1 is fainter than ascertained from our P-L relation, causing its distance to be underestimated. Its measured period is also considerably in excess of the longest-period Cepheid in our P-L relation, VX Cygni. Its high χ^2_v value indicates a poor initial fit, though its low

τ value and posterior spread indicates its chain converged. This is in part attributed to the use of a cited value for its $B - V$ value. The sinusoidal pattern in the residuals of the M31 CV1 fit should be noted, indicating a systematic error which is attributed to the filter transformation.

CONCLUSION

The distance measured to Andromeda, $660^{+66}_{-60} \text{ kpc}$, was closer than the literature value of $761 \pm 11 \text{ kpc}$, but within the 95% credible interval (2σ).

The considerable number of identified systematic errors affecting the P-L calibration complicate disentangling the exact cause of the too-shallow slope a and less-negative zero point b .

The primary source of error is attributed to the inability to take background-limited exposures of the Cepheids without saturation. Saturation was directly responsible for the omission of 4 Cepheids from the P-L relation: the significantly read-noise-limited exposures introduced a t_{exp} -dependent systematic brightening of the remaining Cepheids. This introduced artificial scatter into the relation and caused complex errors in both a and b . The misaligned calibration frames are considered a less-severe systematic error.

The sparse sampling of the light curves introduced overfitting problems in the model fitting. It is likely the focus on determining the correct period during initialisation came at the cost of accuracy in the magnitudes. However, both of these problems were unavoidable given observing constraints. The robust error propagation and detailed analysis of posterior distributions made possible by the MCMC methods used during model fitting instilled confidence in the results obtained on low-quality data. Adopting light-curve tem-

plate fitting would have allowed a more rigorous determination of the model parameters given the limited dataset.

The approximations used to transform the SDSS g -band M31 CV1 data onto the Johnson V -band in combination with the use of a literature $B - V$ value are attributed as the leading cause of the error in the determination of the period of M31 CV1.

The P-L relation could have been improved with a correction for the relationship between metallicity and brightness in Cepheids. Further benefit would have come from consideration and correction for the complex pulsation modes of the Cepheids, especially for TU Cassiopeiae. The dependence of a P-L relation on the period-colour relation, which vary between stellar populations, introduced unavoidable systematic error when placing a Cepheid in the Andromeda Galaxy onto a relation calibrated by Milky Way Cepheids.

Determining the distance to the Andromeda Galaxy by the methodology described herein is thus only reliable as a first-order estimate. The obtained result is encouraging given the methodology was robust and results were limited by poor data. More observing epochs spread over a longer time period; corrections for metallicity and colour; and data for M31 CV1 in the V and B filters to determine a proper filter correction would improve future results.

REFERENCES

- [1] G. Fritz Benedict et al. "Hubble Space Telescope Fine Guidance Sensor Parallaxes of Galactic Cepheid Variable Stars: Period-Luminosity Relations*". In: *The Astronomical Journal* 133.4 (Mar. 2007), p. 1810. issn: 1538-3881. doi: 10.1086/511980.
- [2] Siyang Li et al. "A Sub-2% Distance to M31 from Photometrically Homogeneous Near-infrared Cepheid Period-Luminosity Relations Measured with the Hubble Space Telescope". In: *The Astrophysical Journal* 920 (Oct. 2021), p. 84. issn: 0004-637X. doi: 10.3847/1538-4357/ac1597.
- [3] Gaia Collaboration et al. "Gaia Early Data Release 3. Summary of the Contents and Survey Properties". In: *Astronomy and Astrophysics* 649 (May 2021), A1. issn: 0004-6361. doi: 10.1051/0004-6361/202039657.
- [4] Henrietta S. Leavitt and Edward C. Pickering. "Periods of 25 Variable Stars in the Small Magellanic Cloud." In: *Harvard College Observatory Circular* 173 (Mar. 1912), pp. 1–3.
- [5] E. P. Hubble. "Cepheids in Spiral Nebulae". In: *The Observatory* 48 (May 1925), pp. 139–142. issn: 0029-7704.
- [6] M. W. Feast and A. R. Walker. "Cepheids as Distance Indicators". In: *Annual Review of Astronomy and Astrophysics* 25. Volume 25, 1987 (Sept. 1987), pp. 345–375. issn: 0066-4146, 1545-4282. doi: 10.1146/annurev.aa.25.090187.002021.
- [7] J. D. Fernie. "THE PERIOD-LUMINOSITY RELATION: A HISTORICAL REVIEW". In: *Publications of the Astronomical Society of the Pacific* 81.483 (Dec. 1969), p. 707. issn: 1538-3873. doi: 10.1086/128847.
- [8] W. Baade. "Problems in the Determination of the Distance of Galaxies." In: *The Astronomical Journal* 63 (May 1958), pp. 207–210. issn: 0004-6256. doi: 10.1086/107726.
- [9] Wendy L. Freedman et al. "Final Results from the Hubble Space TelescopeKey Project to Measure the HubbleConstant*". In: *The Astrophysical Journal* 553.1 (May 2001), p. 47. issn: 0004-637X. doi: 10.1086/320638.
- [10] David G. Turner. "The Progenitors of Classical Cepheid Variables". In: *Journal of the Royal Astronomical Society of Canada* 90 (Apr. 1996), p. 82. issn: 0035-872X.
- [11] David G. Turner. "The PL Calibration for Milky Way Cepheids and Its Implications for the Distance Scale". In: *Astrophysics and Space Science* 326 (Apr. 2010), pp. 219–231. issn: 0046-640X. doi: 10.1007/s10509-009-0258-5.
- [12] Alfred Gautschy and Hideyuki Saio. "STELLAR PULSATIONS ACROSS THE HR DIAGRAM: Part II". In: *Annual Review of Astronomy and Astrophysics* 34. Volume 34, 1996 (Sept. 1996), pp. 551–606. issn: 0066-4146, 1545-4282. doi: 10.1146/annurev.astro.34.1.551.

- [13] Francis LeBlanc. "An Introduction to Stellar Astrophysics". In: *Wiley* (2010), p. 196.
- [14] R.S. Stobie. "Cepheids". In: *International Astronomical Union Colloquium* 29 (1976), 87–113. doi: 10.1017/S0252921100061923.
- [15] Joyce A. Guzik, Jason Jackiewicz, and Nancy R. Evans. *Challenges in Cepheid Evolution and Pulsation Modeling*. July 2023. doi: 10.48550/arXiv.2307.12386. arXiv: 2307.12386 [astro-ph].
- [16] Barry F. Madore and Wendy L. Freedman. "THE CEPHEID DISTANCE SCALE". In: *Publications of the Astronomical Society of the Pacific* 103.667 (Sept. 1991), p. 933. issn: 1538-3873. doi: 10.1086/132911.
- [17] E. Antonello and E. Poretti. "Structural Properties of the Light Curves of S-Cepheids." In: *Astronomy and Astrophysics* 169 (Nov. 1986), pp. 149–153. issn: 0004-6361.
- [18] J. Robert Buchler. "The State of Cepheid Pulsation Theory". In: *AIP Conference Proceedings*. 2009, pp. 51–58. doi: 10.1063/1.3246556. arXiv: 0907.1766 [astro-ph].
- [19] I. Soszyński et al. *The Optical Gravitational Lensing Experiment. The OGLE-III Catalog of Variable Stars. XIV. Classical and TypeII Cepheids in the Galactic Bulge*. Dec. 2011. doi: 10.48550/arXiv.1112.1406.
- [20] R. Smolec and P. Moskalik. "Non-Linear Modelling of Beat Cepheids: Resonant and Non-Resonant Models". In: *Astronomy & Astrophysics* 524 (Dec. 2010), A40. issn: 0004-6361, 1432-0746. doi: 10.1051/0004-6361/201014494.
- [21] G. Bono, M. Marconi, and R. F. Stellingwerf. *Classical Cepheid Pulsation Models — VI. The Hertzsprung Progression*. Aug. 2000. doi: 10.48550/arXiv.astro-ph/0006229.
- [22] P. Pietrukowicz, I. Soszyński, and A. Udalski. "Classical Cepheids in the Milky Way". In: *Acta Astronomica* 71.3 (Nov. 2021), pp. 205–222. issn: 00015237. doi: 10.32023/0001-5237/71.3.2. arXiv: 2112.03284 [astro-ph].
- [23] P. Klagyivik and L. Szabados. "Observational Studies of Cepheid Amplitudes - I. Period-amplitude Relationships for Galactic Cepheids and Interrelation of Amplitudes". In: *Astronomy & Astrophysics* 504.3 (Sept. 2009), pp. 959–972. issn: 0004-6361, 1432-0746. doi: 10.1051/0004-6361/200811464.
- [24] L. N. Berdnikov and E. N. Pastukhova. "Search for Evolutionary Changes in the Periods of the Double-Mode Cepheid TU Cas". In: *Astronomy Letters* 47.8 (Aug. 2021), pp. 544–559. issn: 1562-6873. doi: 10.1134/S1063773721070021.
- [25] F. Arenou et al. "Gaia Data Release 2. Catalogue Validation". In: *Astronomy and Astrophysics* 616 (Aug. 2018), A17. issn: 0004-6361. doi: 10.1051/0004-6361/201833234.
- [26] C. A. L. Bailer-Jones et al. "VizieR Online Data Catalog: Distances to 1.47 Billion Stars in Gaia EDR3 (Bailer-Jones+, 2021)". In: *VizieR Online Data Catalog* 1352 (Feb. 2021), pp. I/352.
- [27] S. Holmes et al. "PIRATE: A Remotely Operable Telescope Facility for Research and Education". In: *Publications of the Astronomical Society of the Pacific* 123.908 (Oct. 2011),

- 1177–1187. ISSN: 1538-3873. doi: 10.1086/662148. URL: <http://dx.doi.org/10.1086/662148>.
- [28] PlaneWave Instruments. *CDK24 f/6.5 Optical Tube Assembly*. <https://planewave.com/product/cdk24-ota/>. Accessed: 2026-02-27.
- [29] Ming-an Guo et al. “Development of 4kx4k long-range digital imaging system”. In: *International Symposium on Photoelectronic Detection and Imaging 2011: Advances in Imaging Detectors and Applications*. Vol. 8194. Proceedings of SPIE. SPIE, Aug. 2011, p. 81940M. doi: 10.1117/12.898938.
- [30] Steve B. Howell. “CCD imaging”. In: *Handbook of CCD Astronomy*. Cambridge Observing Handbooks for Research Astronomers. Cambridge University Press, 2006, 66–101.
- [31] Rodney F Warren-Smith et al. “CCDPACK: CCD Data Reduction Package”. In: *Astrophysics Source Code Library* (2014), ascl-1403.
- [32] Peter B. Stetson. “DAOPHOT - A Computer Program for Crowded-Field Stellar Photometry”. In: *Publications of the Astronomical Society of the Pacific* 99 (Mar. 1987), p. 191. ISSN: 0004-6280, 1538-3873. doi: 10.1086/131977.
- [33] “CCD Imaging”. In: *Handbook of CCD Astronomy*. Ed. by Steve B. Howell. 2nd ed. Cambridge Observing Handbooks for Research Astronomers. Cambridge: Cambridge University Press, 2006, pp. 66–101. ISBN: 978-0-521-61762-8. doi: 10.1017/CBO9780511807909.006.
- [34] The Astropy Collaboration et al. “The Astropy Project: Sustaining and Growing a Community-oriented Open-source Project and the Latest Major Release (v5.0) of the Core Package”. In: *The Astrophysical Journal* 935.2 (Aug. 2022), p. 167. ISSN: 0004-637X, 1538-4357. doi: 10.3847/1538-4357/ac7c74. arXiv: 2206.14220 [astro-ph].
- [35] E. Norman Walker. *CCD Photometry*. Accessed: 01-02-2026. n.d. URL: https://britastro.org/vss/ccd_photometry.htm.
- [36] Rajiv Daxini and Yupeng Wu. “Review of methods to account for the solar spectral influence on photovoltaic device performance”. In: *Energy* 286 (2024), p. 129461. ISSN: 0360-5442. doi: <https://doi.org/10.1016/j.energy.2023.129461>. URL: <https://www.sciencedirect.com/science/article/pii/S0360544223028554>.
- [37] Skipper Seabold and Josef Perktold. “Statsmodels: Econometric and Statistical Modeling with Python”. In: *Proceedings of the 9th Python in Science Conference 2010* (Jan. 2010).
- [38] Dave Kilkenny. *Photometry – I. “All sky”*. <https://optical-astronomy.education/onewebmedia/kilkenny.pdf>. Accessed: 1 February 2026.
- [39] David J. Schlegel, Douglas P. Finkbeiner, and Marc Davis. “Maps of Dust Infrared Emission for Use in Estimation of Reddening and Cosmic Microwave Background Radiation Foregrounds”. In: 500.2 (June 1998), pp. 525–553. doi: 10.1086/305772. arXiv: astro-ph/9710327 [astro-ph].
- [40] *DDO Cepheids - Colour Excess*. URL: https://www.astro.utoronto.ca/DDO/research/cepheids/table_colourexcess.html{textbraceright}.

- [41] Jason A. Cardelli, Geoffrey C. Clayton, and John S. Mathis. "The relationship between infrared, optical, and ultraviolet extinction". en. In: *The Astrophysical Journal* 345 (Oct. 1989), p. 245. issn: 0004-637X, 1538-4357. doi: 10.1086/167900. url: <http://adsabs.harvard.edu/doi/10.1086/167900> (visited on 02/06/2026).
- [42] M. Wenger et al. "The SIMBAD astronomical database: The CDS reference database for astronomical objects". en. In: *Astronomy and Astrophysics Supplement Series* 143.1 (Apr. 2000), pp. 9–22. issn: 0365-0138, 1286-4846. doi: 10.1051/aas:2000332. url: <http://aas.aanda.org/10.1051/aas:2000332> (visited on 02/24/2026).
- [43] Heather Flewelling. "Pan-STARRS Data Release 2". In: *American Astronomical Society Meeting Abstracts #231*. Vol. 231. Jan. 2018, p. 436.01.
- [44] A. Ginsburg, B.M. Sipocz, C.E. Brasseur, et al. "astroquery: An Astronomical Web-querying Package in Python". In: *The Astronomical Journal* 157 (2019), p. 98.
- [45] F. Oschenbein and other. *The VizieR database of astronomical catalogues*. doi: 10.26093/cds/vizier.
- [46] S. Jester, D.P. Schneider, G.T. Richards, et al. "The Sloan Digital Sky Survey View of the Palomar-Green Bright Quasar Survey". In: *The Astronomical Journal* 130 (2005), p. 873.
- [47] *Alert Notice 422: Observing Campaign on Hubble's First Variable in M31: M31_V1 | Aavso*. url: <https://www.aavso.org/index.php/aavso-alert-notice-422>.
- [48] H. L. Johnson and W. W. Morgan. "Fundamental Stellar Photometry for Standards of Spectral Type on the Revised System of the Yerkes Spectral Atlas." In: *The Astrophysical Journal* 117 (May 1953), p. 313. issn: 0004-637X. doi: 10.1086/145697.
- [49] Charles R. Harris et al. "Array Programming with NumPy". In: *Nature* 585.7825 (Sept. 2020), pp. 357–362. issn: 1476-4687. doi: 10.1038/s41586-020-2649-2.
- [50] Pauli Virtanen et al. "SciPy 1.0: Fundamental Algorithms for Scientific Computing in Python". In: *Nature Methods* 17.3 (Mar. 2020), pp. 261–272. issn: 1548-7105. doi: 10.1038/s41592-019-0686-2.
- [51] Jacob T. VanderPlas. "Understanding the Lomb–Scargle Periodogram". In: *The Astrophysical Journal Supplement Series* 236.1 (May 2018), p. 16. issn: 0067-0049. doi: 10.3847/1538-4365/aab766.
- [52] J. H. Minniti et al. "Using Classical Cepheids to Study the Far Side of the Milky Way Disk - I. Spectroscopic Classification and the Metallicity Gradient". In: *Astronomy & Astrophysics* 640 (Aug. 2020), A92. issn: 0004-6361, 1432-0746. doi: 10.1051/0004-6361/202037575.
- [53] Michel Breger. "The Unusual Classical Cepheid Hr 7308: 1966-1969". In: *International Astronomical Union Colloquium* 58 (Aug. 1980), pp. 431–436. issn: 0252-9211. doi: 10.1017/S0252921100081872.
- [54] I. Soszyński et al. "Discovery of the Longest-period Classical Cepheid in the Milky Way". In: *The Astrophysical Journal Letters* 965.2 (Apr. 2024), p. L17. issn: 2041-8205. doi: 10.3847/2041-8213/ad392f.

- [55] Donald W. Marquardt. "An Algorithm for Least-Squares Estimation of Nonlinear Parameters". In: *Journal of the Society for Industrial and Applied Mathematics* 11.2 (1963), pp. 431–441. ISSN: 0368-4245. JSTOR: 2098941.
- [56] Daniel Foreman-Mackey et al. "Emcee: The MCMC Hammer". In: *Publications of the Astronomical Society of the Pacific* 125.925 (Feb. 2013), p. 306. ISSN: 1538-3873. doi: 10.1086/670067.
- [57] Jonathan Goodman and Jonathan Weare. "Ensemble Samplers with Affine Invariance". In: *Communications in Applied Mathematics and Computational Science* 5 (Jan. 2010), pp. 65–80. doi: 10.2140 / camcos . 2010.5.65.
- [58] *Autocorrelation Analysis & Convergence — Emcee*. url: <https://emcee.readthedocs.io/en/stable/tutorials/autocorr>.
- [59] Dorota M. Skowron et al. "A Three-Dimensional Map of the Milky Way Using Classical Cepheid Variable Stars". In: *Science* 365 (Aug. 2019), pp. 478–482. ISSN: 0036-8075. doi: 10.1126/science.aau3181.
- [60] R. Earle Luck and David L. Lambert. "THE DISTRIBUTION OF THE ELEMENTS IN THE GALACTIC DISK. III. A RECONSIDERATION OF CEPHEIDS FROM $1 = 30^\circ$ TO 250° ". In: *The Astronomical Journal* 142.4 (Sept. 2011), p. 136. ISSN: 1538-3881. doi: 10.1088/0004-6256/142/4/136.
- [61] A. G. A. Brown et al. "Gaia Data Release 2 - Summary of the Contents and Survey Properties". In: *Astronomy & Astrophysics* 616 (Aug. 2018), A1. ISSN: 0004-6361, 1432-0746. doi: 10.1051/0004-6361/201833051.
- [62] Kim M. Sebo et al. "The Cepheid Period-Luminosity Relation in the Large Magellanic Cloud". In: *The Astrophysical Journal Supplement Series* 142.1 (Sept. 2002), p. 71. ISSN: 0067-0049. doi: 10.1086/341177.
- [63] Barry F. Madore and Wendy L. Freedman. "MULTI-WAVELENGTH CHARACTERISTICS OF PERIOD-LUMINOSITY RELATIONS". In: *The Astrophysical Journal* 744.2 (Dec. 2011), p. 132. ISSN: 0004-637X. doi: 10.1088/0004-637X/744/2/132.
- [64] Xiaodian Chen et al. "The Zwicky Transient Facility Catalog of Periodic Variable Stars". In: *The Astrophysical Journal Supplement Series* 249.1 (July 2020), p. 18. ISSN: 0067-0049. doi: 10.3847 / 1538 - 4365 / ab9cae.
- [65] I. Ji et al. "Estimating Sky Level". In: *Publications of the Astronomical Society of the Pacific* 130 (2018), p. 084504.
- [66] L. Inno et al. "New NIR Light-Curve Templates for Classical Cepheids". In: *Astronomy & Astrophysics* 576 (Apr. 2015), A30. ISSN: 0004-6361, 1432-0746. doi: 10.1051/0004-6361 / 201424396.
- [67] Garance Bras et al. "Versatile Light Curve Templates of Cepheids - Multi-band Fitting of Photometric Time Series". In: *Astronomy & Astrophysics* 698 (June 2025), A97. ISSN: 0004-6361, 1432-0746. doi: 10.1051 / 0004-6361 / 202553783.
- [68] S. M. Andrievsky et al. "An Investigation of the Double-Mode Cepheid TU Cassiopeiae – I. Atmospheric Parameters and Chemical Composition". In: *Monthly Notices of the Royal Astronomical Society* 265.2 (Nov. 1993), pp. 257–260. ISSN: 0035-8711. doi: 10.1093/mnras/265.2.257.

- [69] Shoko Sakai et al. "The Effect of Metallicity on Cepheid-based Distances*". In: *The Astrophysical Journal* 608.1 (June 2004), p. 42. issn: 0004-637X. doi: 10.1086/386540.
- [70] V. Ripepi et al. "Period–Luminosity–Metallicity Relation of Classical Cepheids". In: *Astronomy & Astrophysics* 642 (Oct. 2020), A230. issn: 0004-6361, 1432-0746. doi: 10.1051/0004-6361/202038714.
- [71] Allan Sandage and G. A. Tammann. "Temperature Differences in the Cepheid Instability Strip Require Differences in the Period–Luminosity Relation in Slope and Zero Point". In: *The Astrophysical Journal* 686.2 (Oct. 2008), p. 779. issn: 0004-637X. doi: 10.1086/591306.
- [72] T.G. Barnes III, J.A. Fernley, M.L. Frueh, et al. "BVRIJHK Photometry of Cepheid Variables". In: *Publications of the Astronomical Society of the Pacific* 109 (1997), p. 645.
- [73] S.M. Kanbur, C.C. Ngeow, and J.R. Buchler. "Period–colour and amplitude–colour relations in classical Cepheid variables – II. The Galactic Cepheid models". In: *Monthly Notices of the Royal Astronomical Society* 354 (2004), pp. 212–224.
- [74] J.D. Fernie et al. https://www.astro.utoronto.ca/DDO/research/cepheids/table_ampmean.html. Accessed: 2026-02-26.
- [75] Arjun Dey et al. "DESI Observations of the Andromeda Galaxy: Revealing the Immigration History of Our Nearest Neighbor". In: *The Astrophysical Journal* 944.1 (Feb. 2023), p. 1. issn: 0004-637X. doi: 10.3847/1538-4357/aca5f8.
- [76] Isaac Newton Group of Telescopes La Palma. *Object Visibility - STARALT*. <https://astro.ing.iac.es/staralt/>. [Accessed 23-10-2025]. 2025.

APPENDICES

TABLES

Cepheid	t_{exp} [s]	N
01 MW Cygni	10	8
02 V520 Cygni	3	9
03 VX Cygni	5	8
04 VY Cygni	5	8
05 CP Cephei	10	9
06 Z Lacertae	5	7
07 V Lacertae	5	8
08 SW Cassiopeiae	10	10
09 TU Cassiopeiae	3	8
10 DL Cassiopeiae	5	8
11 V636 Cassiopeiae	3	8

Table 6: A representative sample of the t_{exp} values for each Cepheid. These values varied across epochs due to observing conditions, however, this most accurately reflects the average t_{exp} for comparison purposes. The number of useable observations is also included. The highlighted entries correspond to targets which were flagged for saturation issues on observation nights.

Cepheid	E(B-V)	[Fe/H]
01 MW Cygni	0.68	0.14
02 V520 Cygni	0.80	0.08
03 VX Cygni	0.79	0.14
04 VY Cygni	0.65	0.05
05 CP Cephei	0.68	0.04
06 Z Lacertae	0.40	0.06
07 V Lacertae	0.36	0.05
08 SW Cassiopeiae	0.49	0.18
09 TU Cassiopeiae	0.12	-0.43
10 DL Cassiopeiae	0.53	0.04
11 V636 Cassiopeiae	0.70	0.11
M31 CV1	0.06	-0.50

Table 7: $E(B-V)$ colour excesses [40] and metallicities [23, 68, 60] of the twelve observed Cepheids.

Cepheid	τ
01 MW Cygni	47.5
02 V520 Cygni	75.2
03 VX Cygni	54.4
04 VY Cygni	100.2
05 CP Cephei	67.1
06 Z Lacertae	61.7
07 V Lacertae	48.3
08 SW Cassiopeiae	47.4
09 TU Cassiopeiae	47.3
10 DL Cassiopeiae	122
11 V636 Cassiopeiae	156.3
M31 CV1	46.7

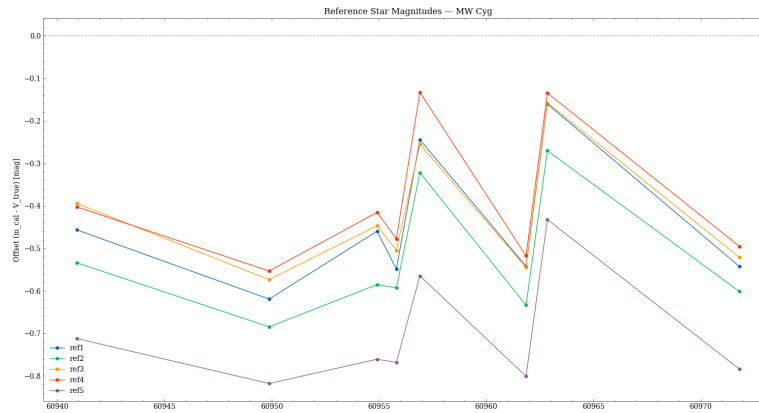
Table 8: The autocorrelation times of the chains of each Cepheid.

CEPHEID PLOTS

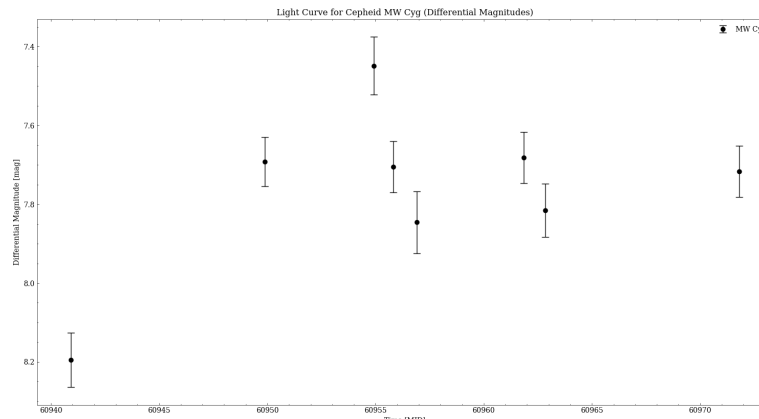
CEPHEID 01 - MW CYGNI



((a)) DAOFIND results for MW Cygni. The estimated location of the Cepheid is shown in red.

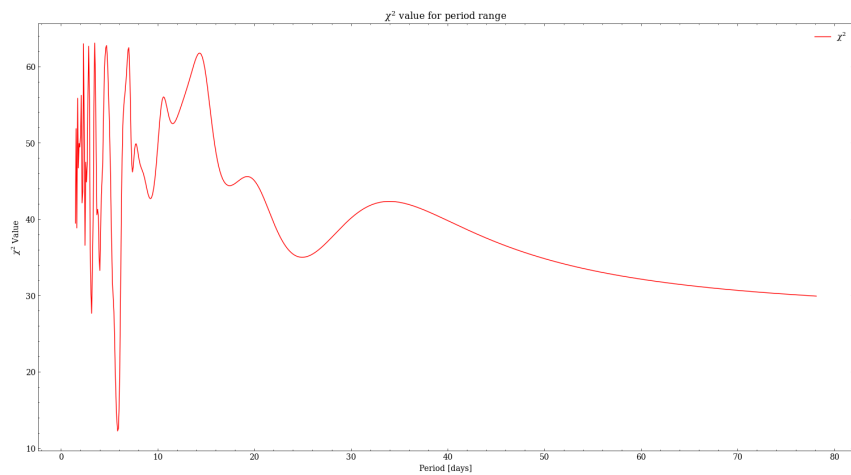


((b)) A graph showing the offset between the calibrated magnitude and the true magnitude for reference stars in the field of MW Cygni, which was used to mitigate night-to-night variations.

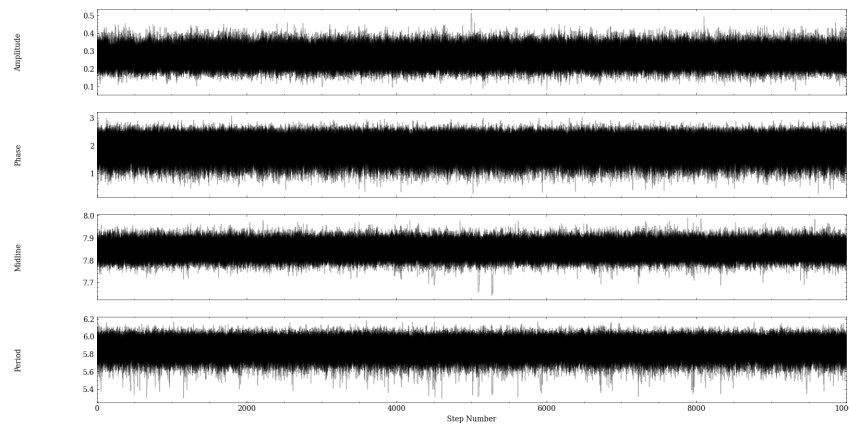


((c)) Initial light curve following differential photometry for MW Cygni.

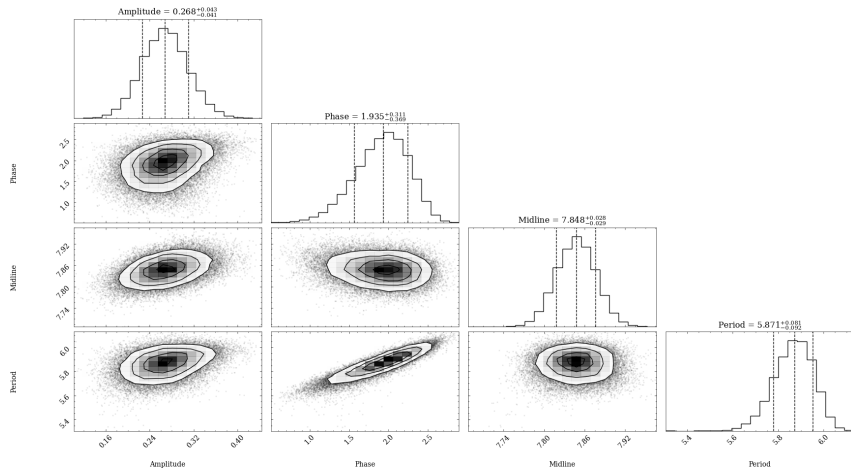
Figure 41: Photometric analysis and sinusoidal modelling results for MW Cygni (1 of 2).



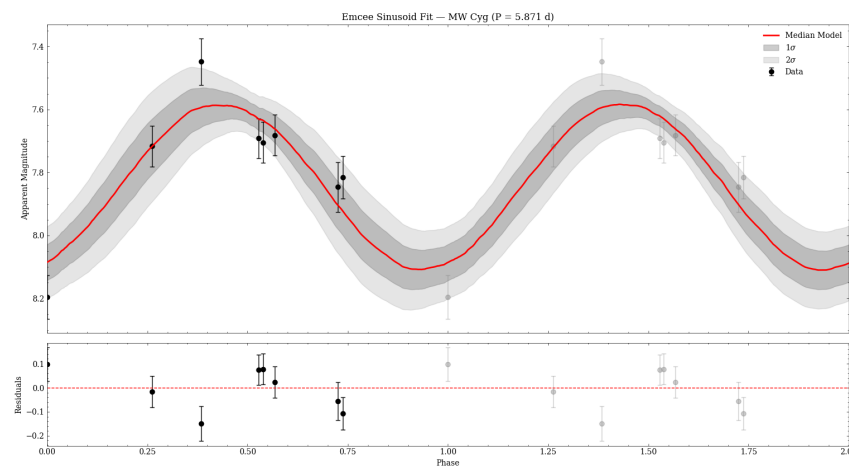
((d)) The χ^2 grid search for MW Cygni using the sinusoidal model.



((e)) The parameter time series of MW Cygni.



((f)) The posterior spread for MW Cygni.

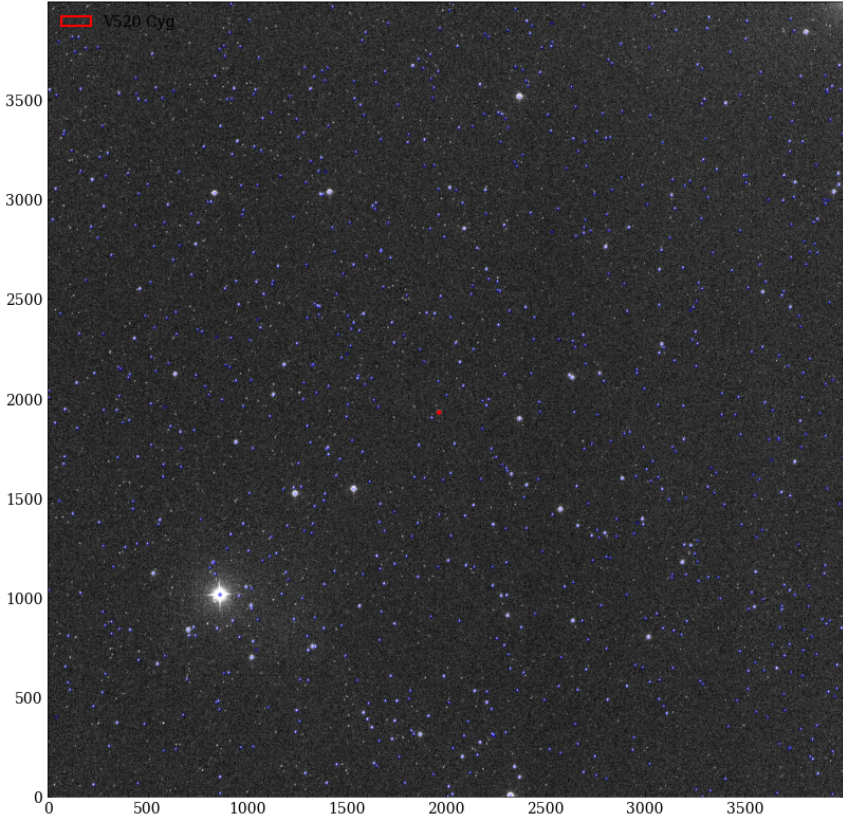


((g)) The final sinusoidal fit to MW Cygni.

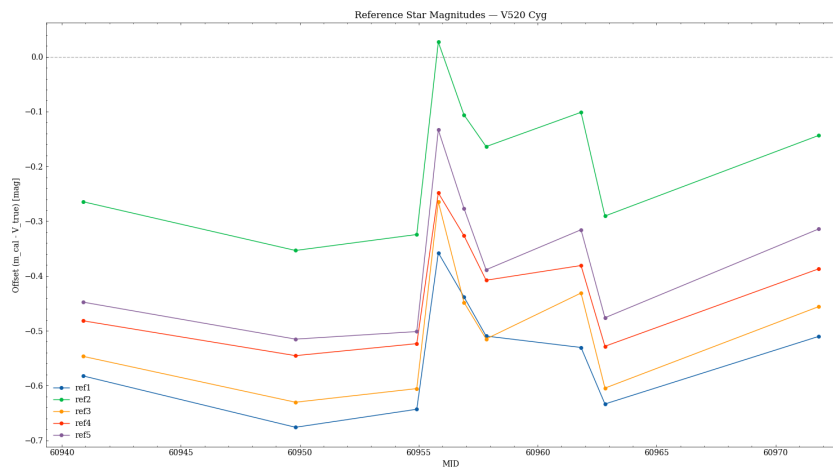
Figure 41: Photometric analysis and sinusoidal modelling results for MW Cygni (2 of 2).

CEPHEID 02 - V520 CYGNI

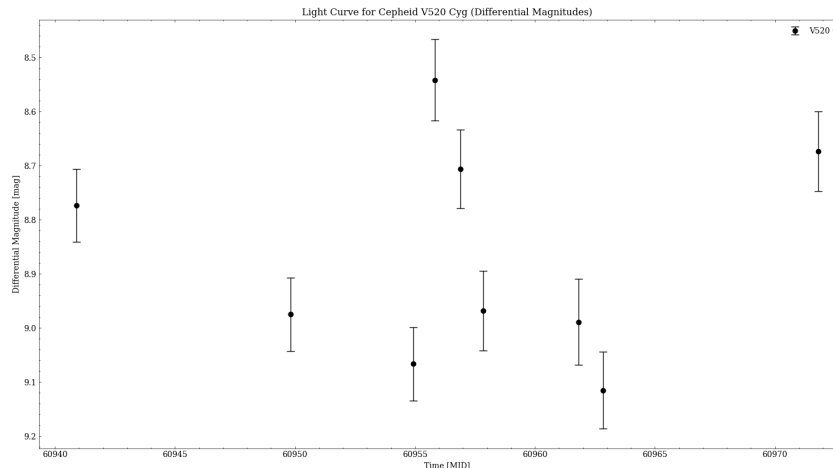
2025-10-06 V520 Cyg Full Image: (917 Sources Detected)



((a)) DAOFIND results for V520 Cygni. The estimated location of the Cepheid is shown in red.

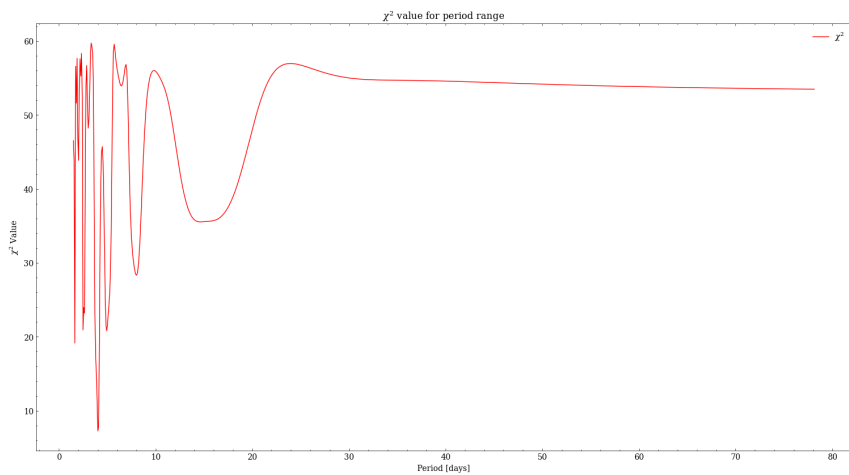


((b)) A graph showing the offset between the calibrated magnitude and the true magnitude for reference stars in the field of V520 Cygni, which was used to mitigate night-to-night variations.

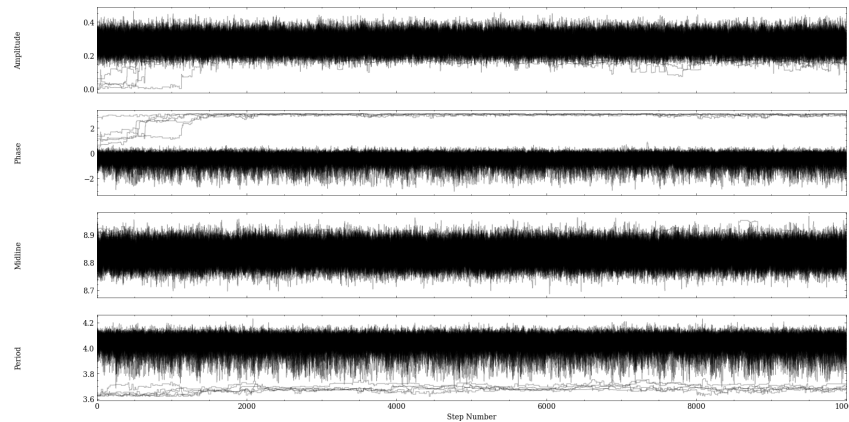


((c)) Initial light curve following differential photometry for V520 Cygni.

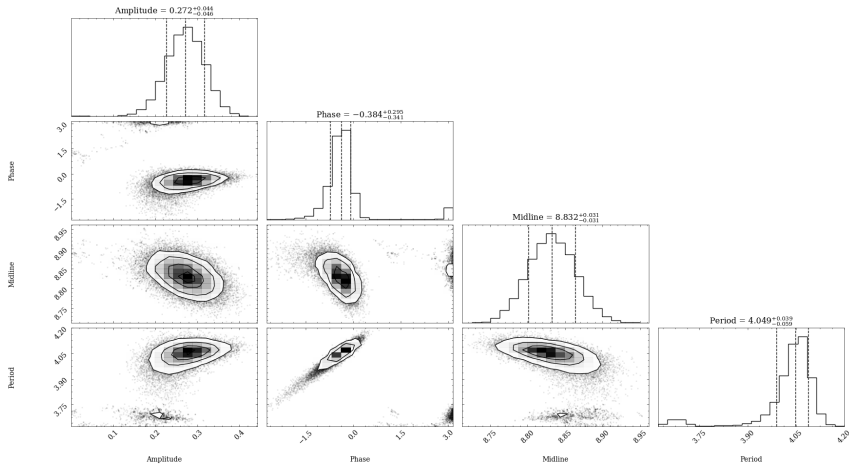
Figure 42: Photometric analysis and sinusoidal modelling results for V520 Cygni (1 of 2).



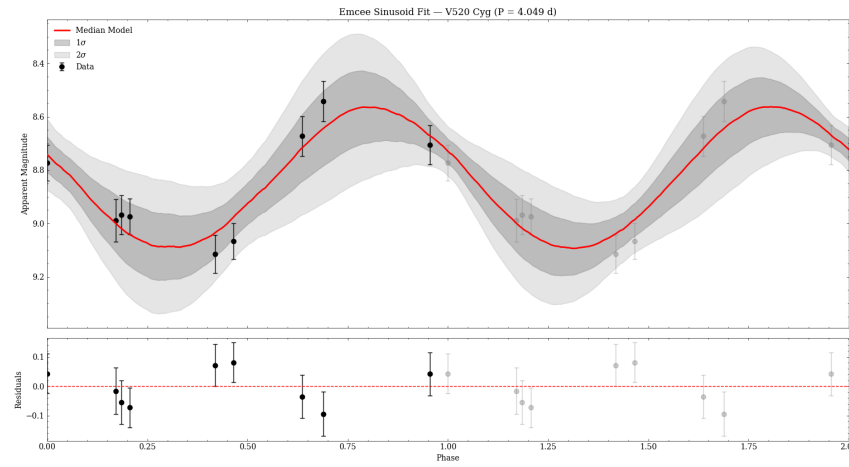
((d)) The χ^2 grid search for V520 Cygni using the sinusoidal model.



((e)) The parameter time series of V520 Cygni.



((f)) The posterior spread for V520 Cygni.



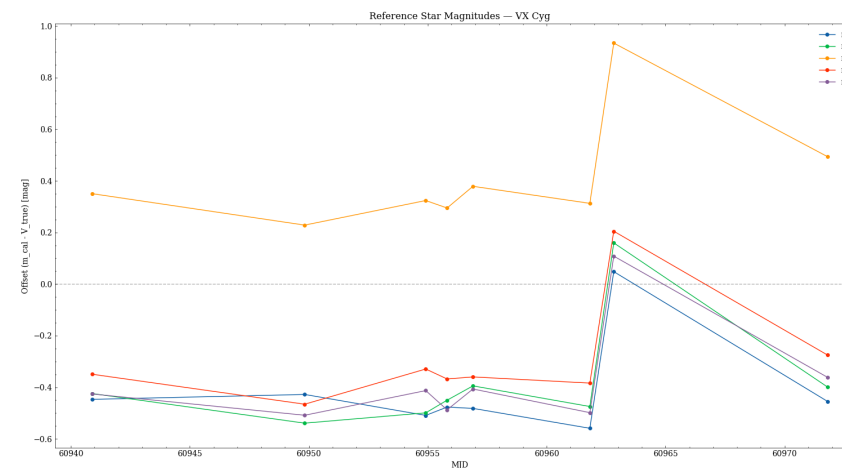
((g)) The final sinusoidal fit to V520 Cygni.

Figure 42: Photometric analysis and sinusoidal modelling results for V520 Cygni (2 of 2).

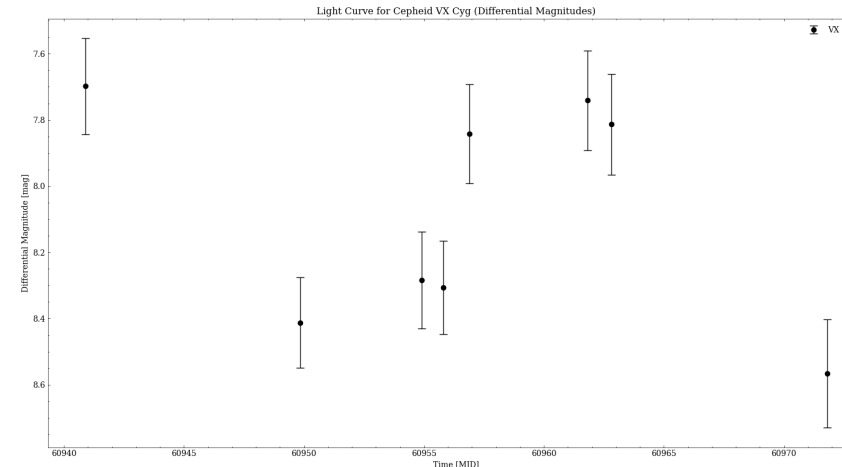
CEPHEID 03 - VX CYGNI



((a)) DAOIND results for VX Cygni. The estimated location of the Cepheid is shown in red.

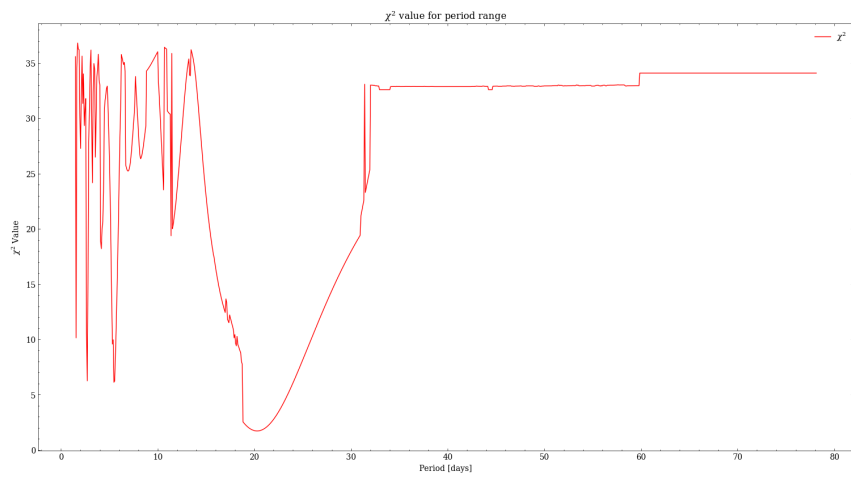


((b)) A graph showing the offset between the calibrated magnitude and the true magnitude for reference stars in the field of VX Cygni, which was used to mitigate night-to-night variations.

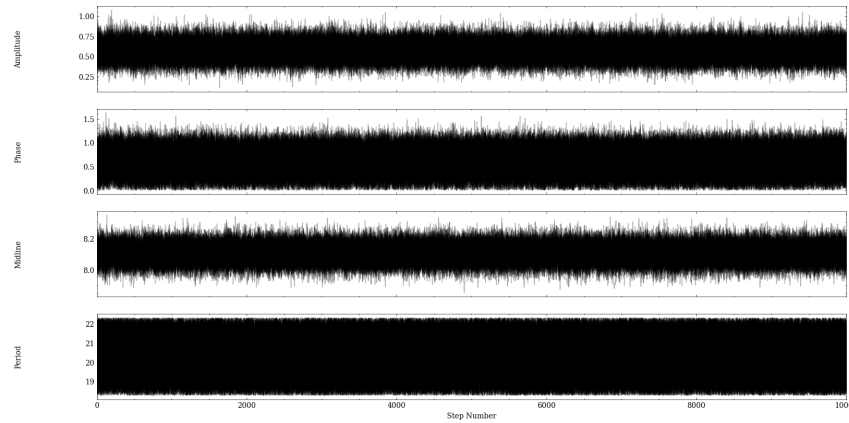


((c)) Initial light curve following differential photometry for VX Cygni.

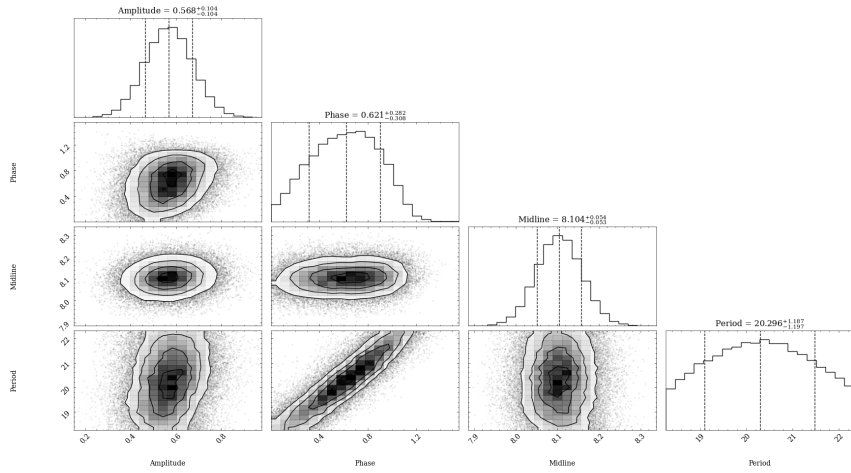
Figure 43: Photometric analysis and sawtooth modelling results for VX Cygni (1 of 2).



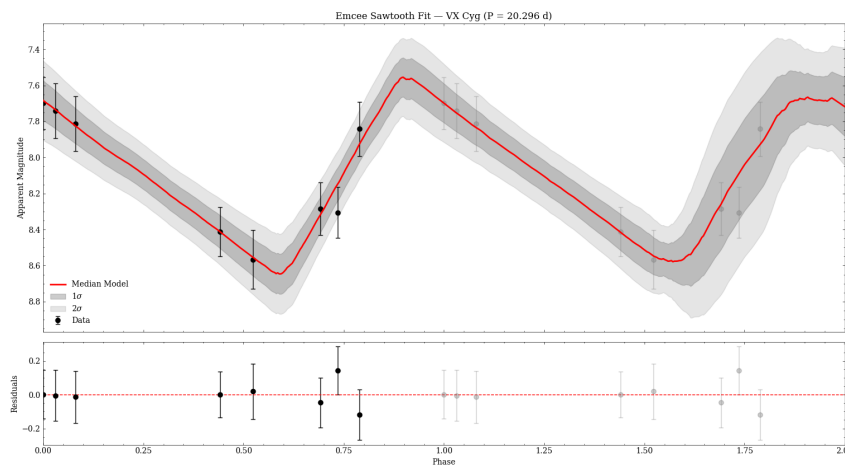
((d)) The χ^2 grid search for VX Cygni using the sawtooth model.



((e)) The parameter time series of VX Cygni.



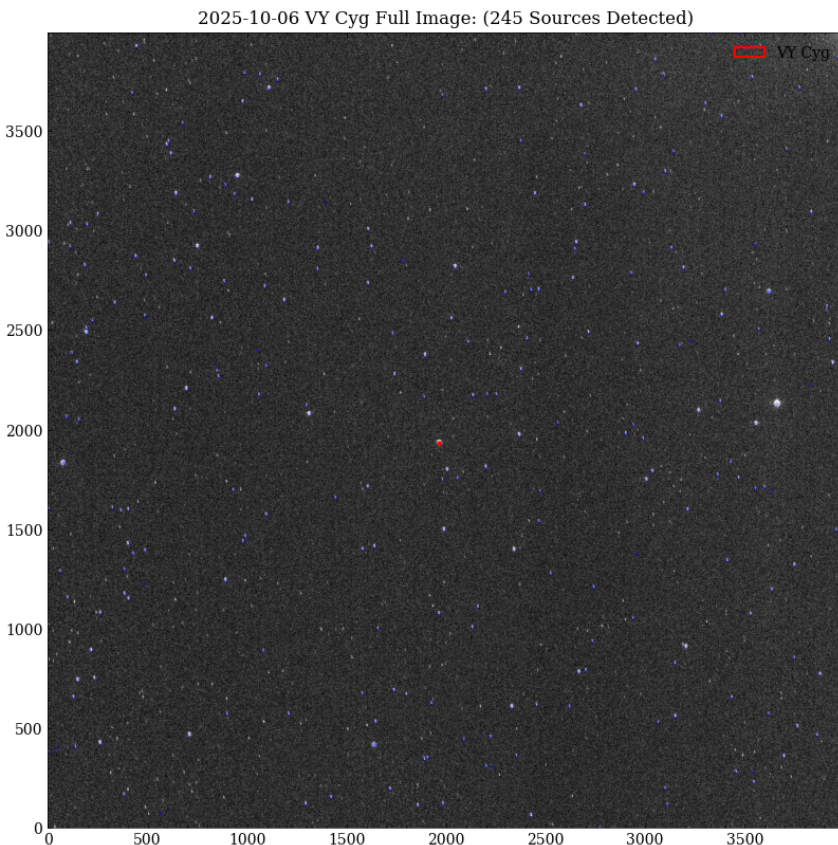
((f)) The posterior spread for VX Cygni



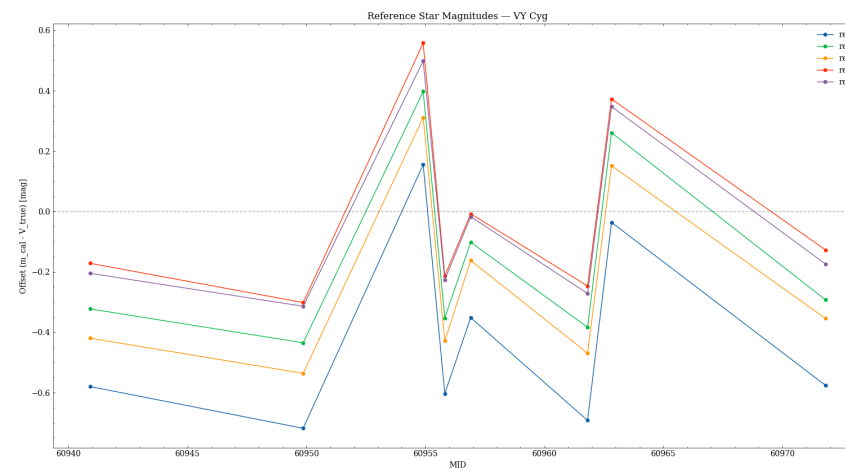
((g)) The final sawtooth fit to VX Cygni.

Figure 43: Photometric analysis and sawtooth modelling results for VX Cygni (2 of 2).

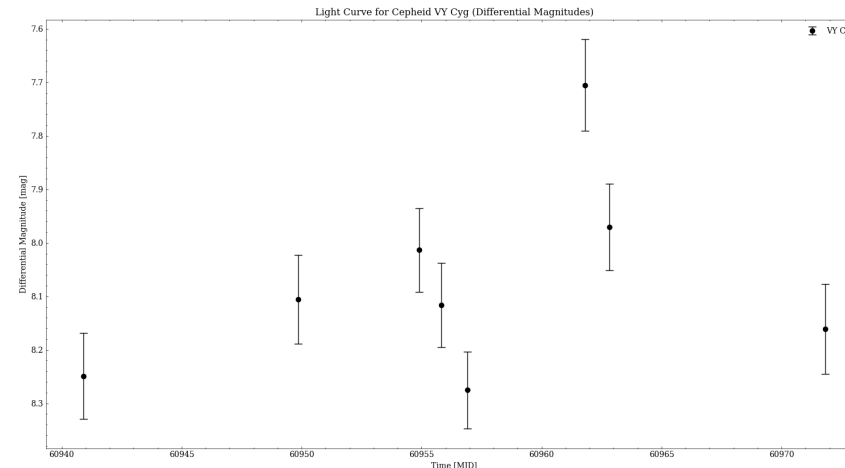
CEPHEID 04 - VY CYGNI



((a)) DAOIND results for VY Cygni. The estimated location of the Cepheid is shown in red.

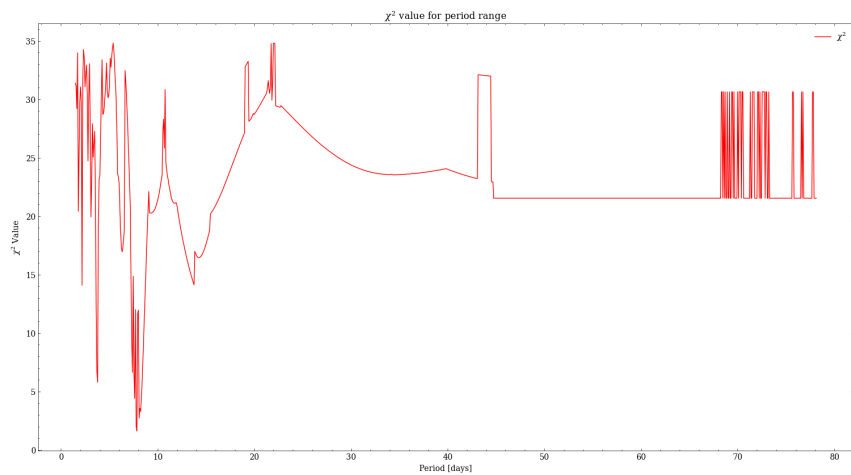


((b)) A graph showing the offset between the calibrated magnitude and the true magnitude for reference stars in the field of VY Cygni, which was used to mitigate night-to-night variations.

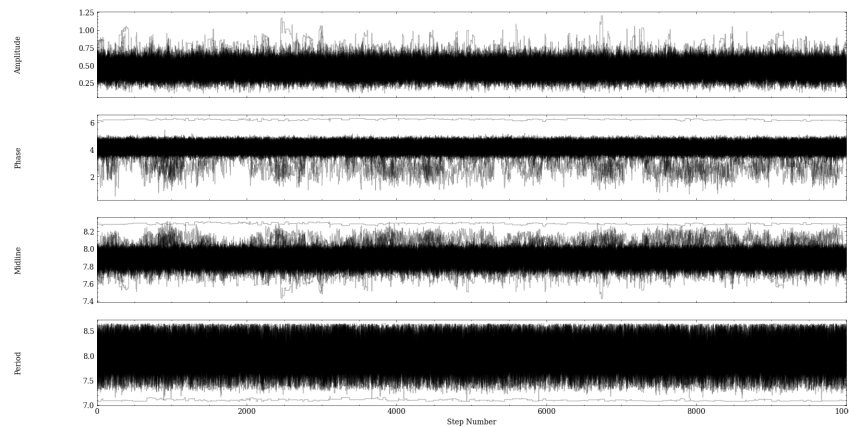


((c)) Initial light curve following differential photometry for VY Cygni.

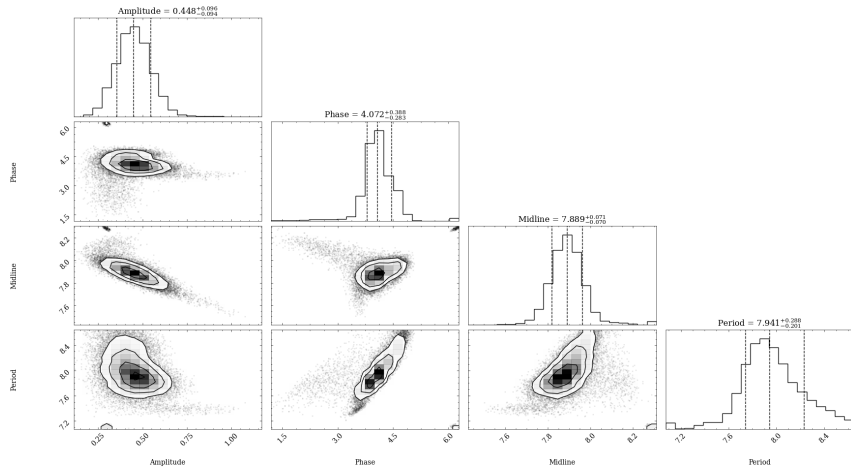
Figure 44: Photometric analysis and sawtooth modelling results for VY Cygni (1 of 2).



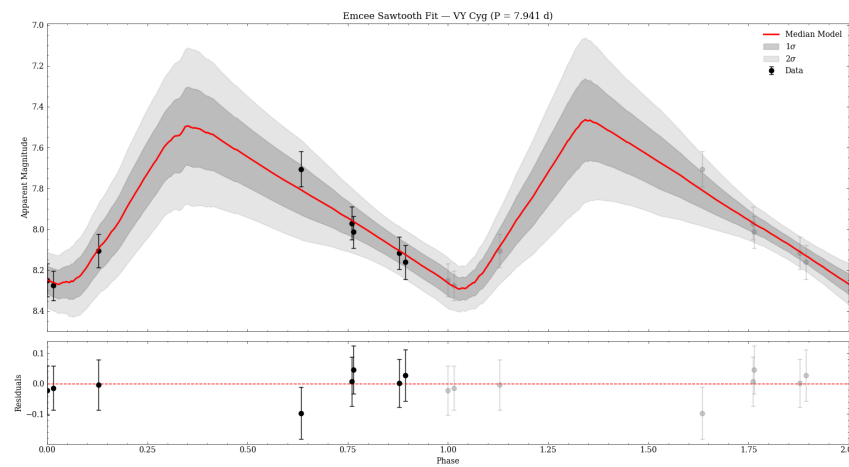
((d)) The χ^2 grid search for VY Cygni using the sawtooth model.



((e)) The parameter time series of VY Cygni.



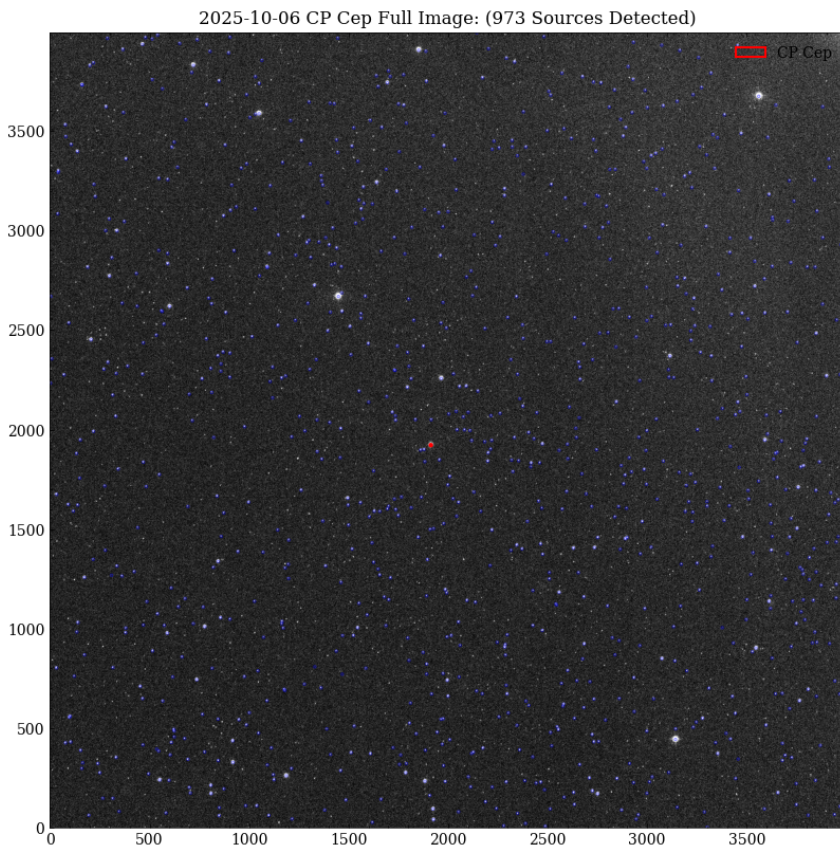
((f)) The posterior spread for VY Cygni.



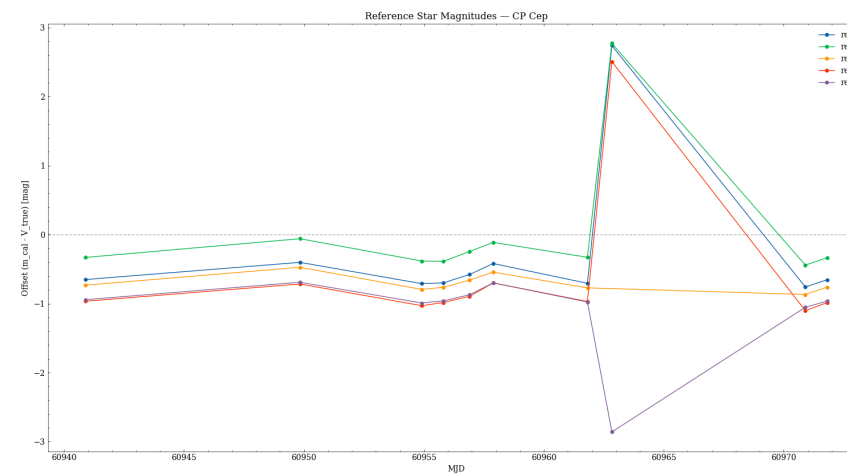
((g)) The final sawtooth fit to VY Cygni.

Figure 44: Photometric analysis and sawtooth modelling results for VY Cygni (2 of 2).

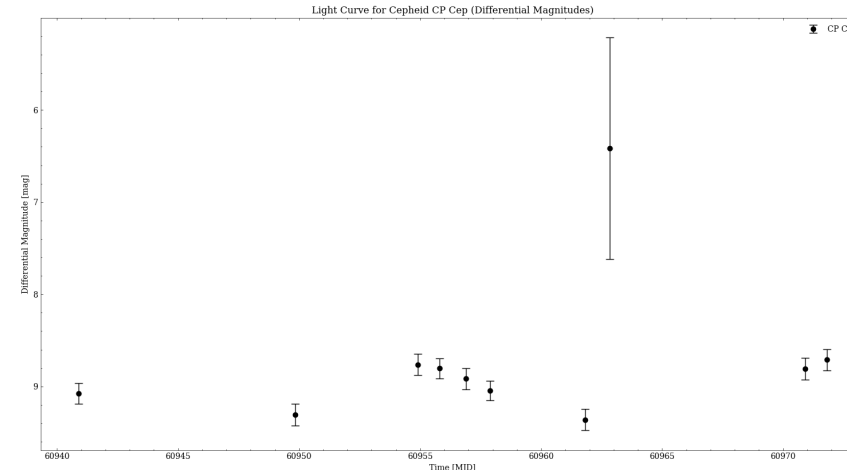
CEPHEID 05 - CP CEPHEI



((a)) DAOIND results for CP Cephei. The estimated location of the Cepheid is shown in red.

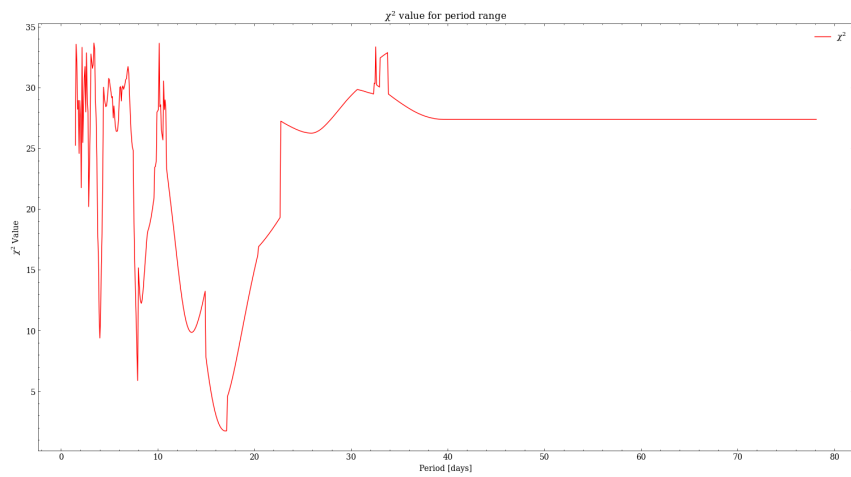


((b)) A graph showing the offset between the calibrated magnitude and the true magnitude for reference stars in the field of CP Cephei, which was used to mitigate night-to-night variations.

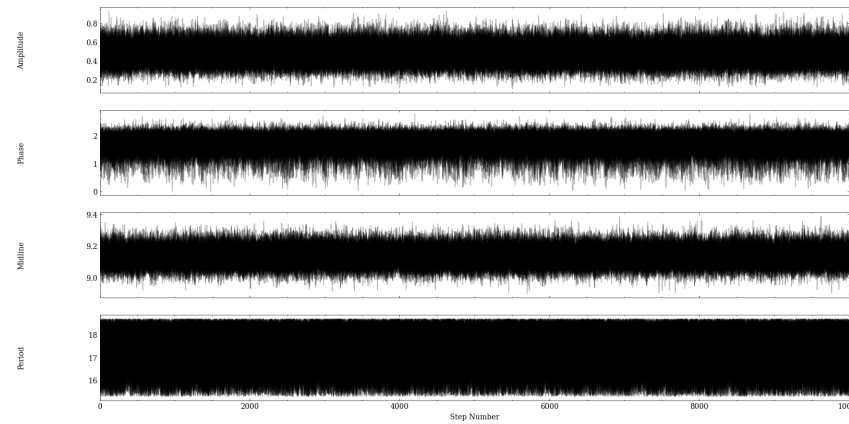


((c)) Initial light curve following differential photometry for CP Cephei.

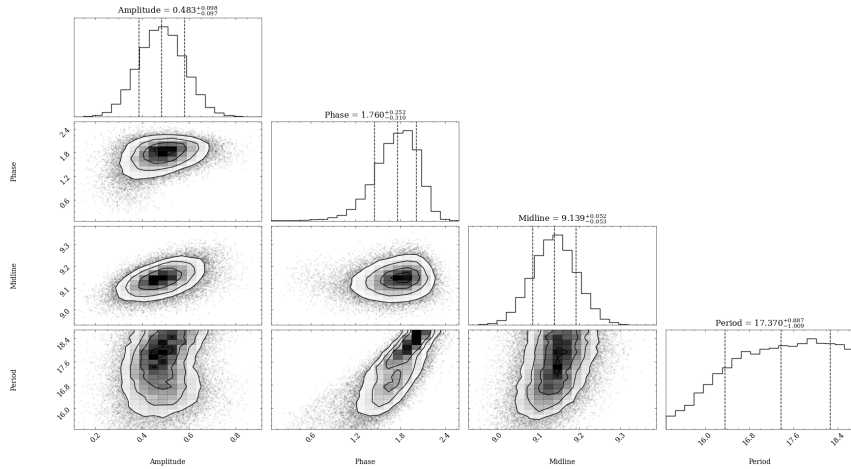
Figure 45: Photometric analysis and sawtooth modelling results for CP Cephei (1 of 2).



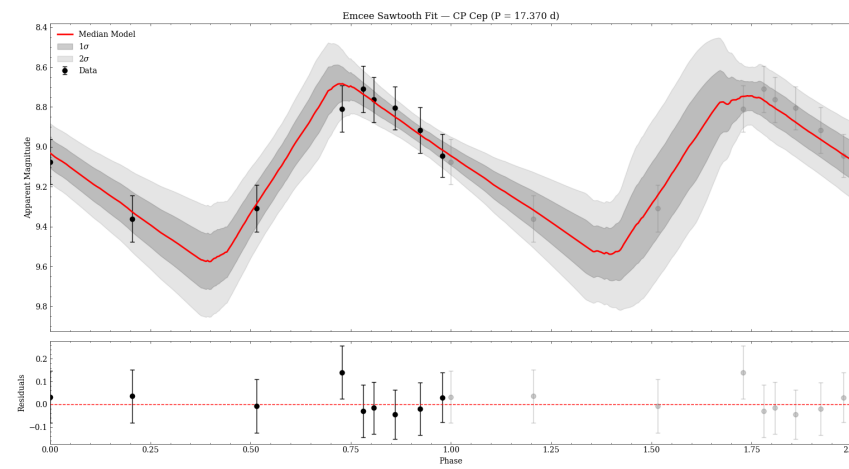
((d)) The χ^2 grid search for CP Cephei using the sawtooth model.



((e)) The parameter time series of CP Cephei.



((f)) The posterior spread for CP Cephei.



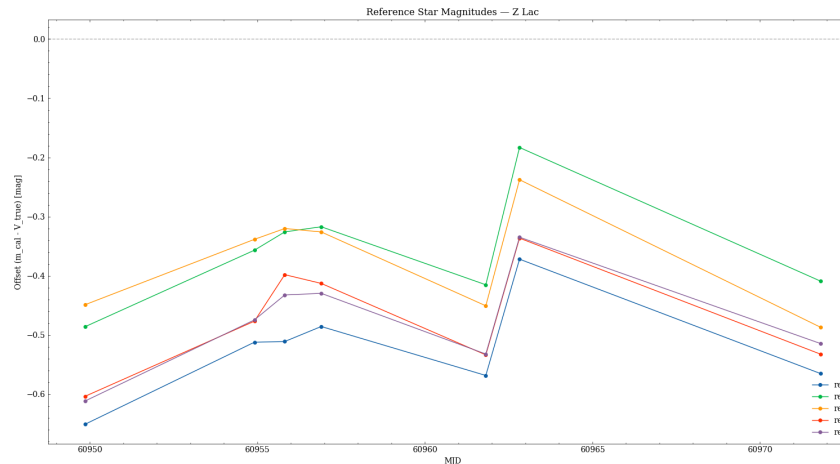
((g)) The final sawtooth fit to CP Cephei.

Figure 45: Photometric analysis and sawtooth modelling results for CP Cephei (2 of 2).

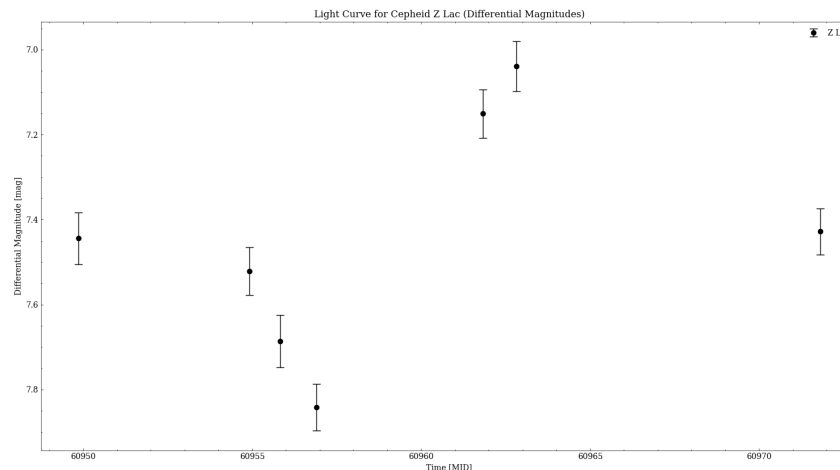
CEPHEID 06 - Z LACERTAE



((a)) DAOIND results for Z Lacertae. The estimated location of the Cepheid is shown in red.

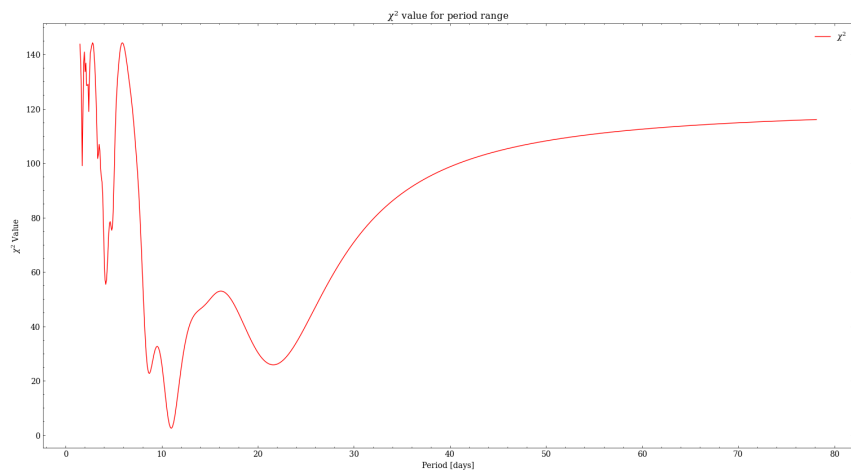


((b)) A graph showing the offset between the calibrated magnitude and the true magnitude for reference stars in the field of Z Lacertae, which was used to mitigate night-to-night variations.

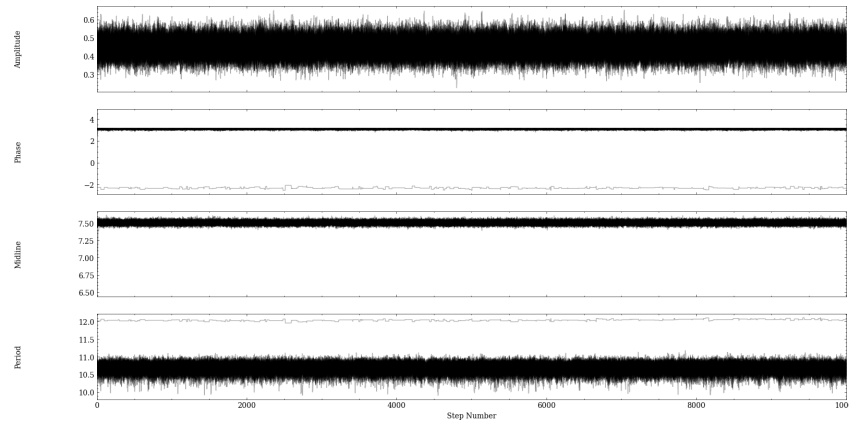


((c)) Initial light curve following differential photometry for Z Lacertae.

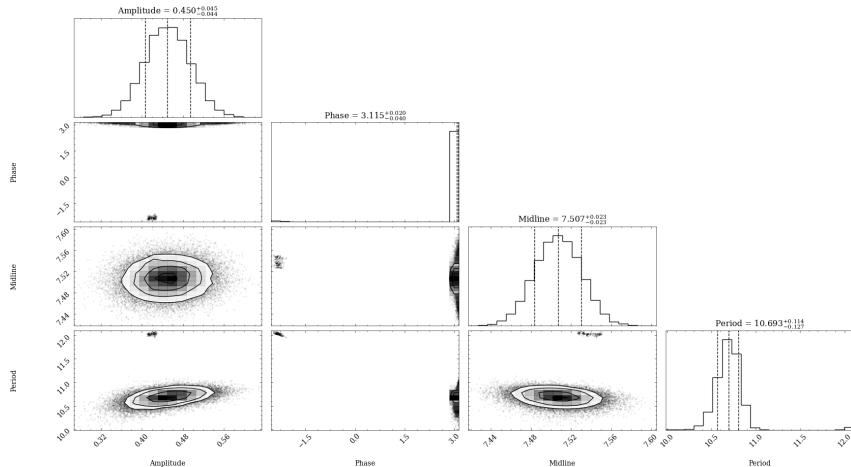
Figure 46: Photometric analysis and sinusoidal modelling results for Z Lacertae (1 of 2).



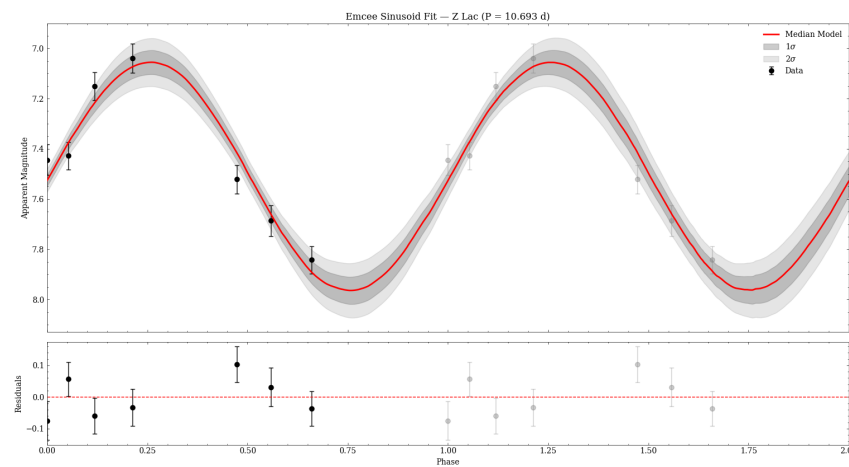
((d)) The χ^2 grid search for Z Lacertae using the sinusoidal model.



((e)) The parameter time series of Z Lacertae.



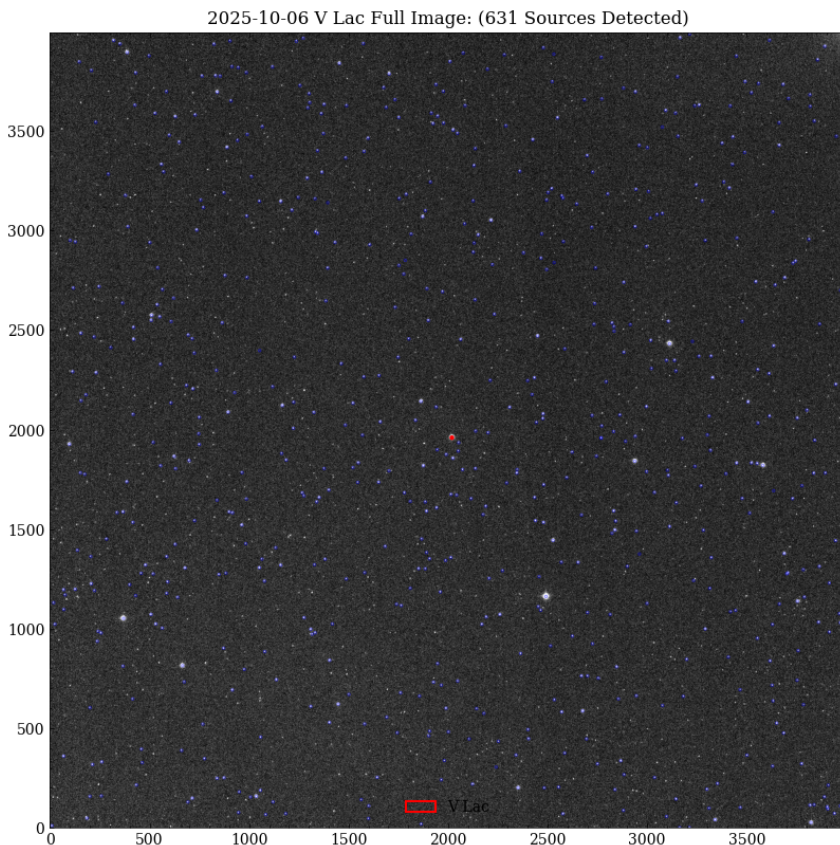
((f)) The posterior spread for Z Lacertae.



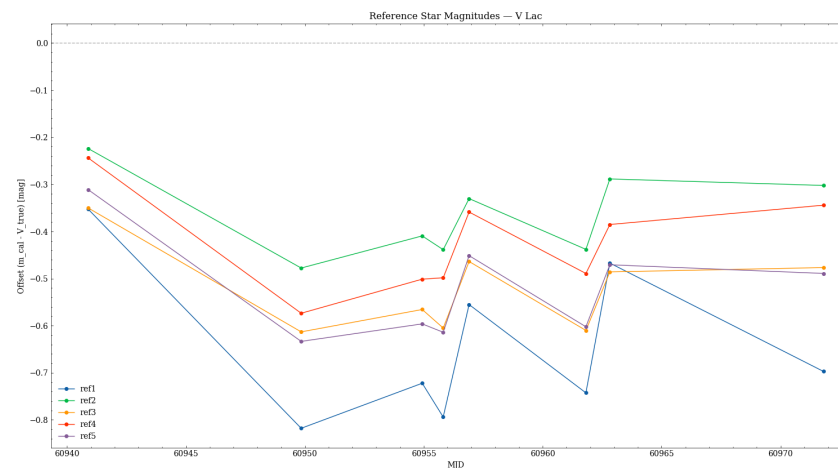
((g)) The final sinusoidal fit to Z Lacertae.

Figure 46: Photometric analysis and sinusoidal modelling results for Z Lacertae (2 of 2).

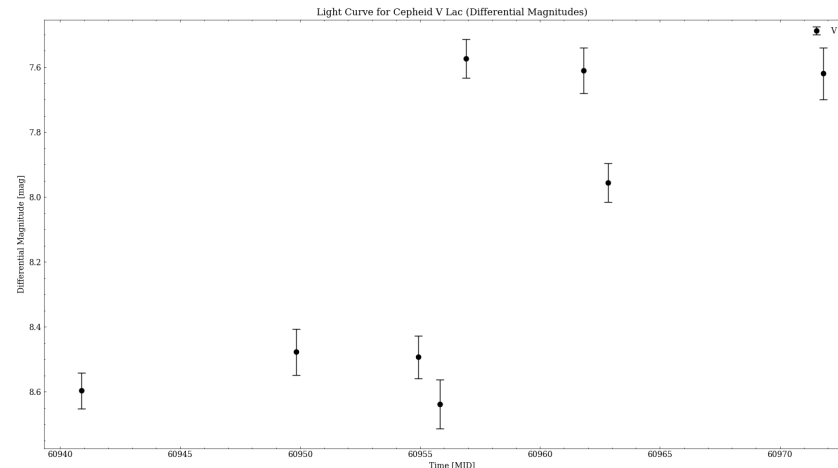
CEPHEID 07 - V LACERTAE



((a)) DAOIND results for V Lacertae. The estimated location of the Cepheid is shown in red.

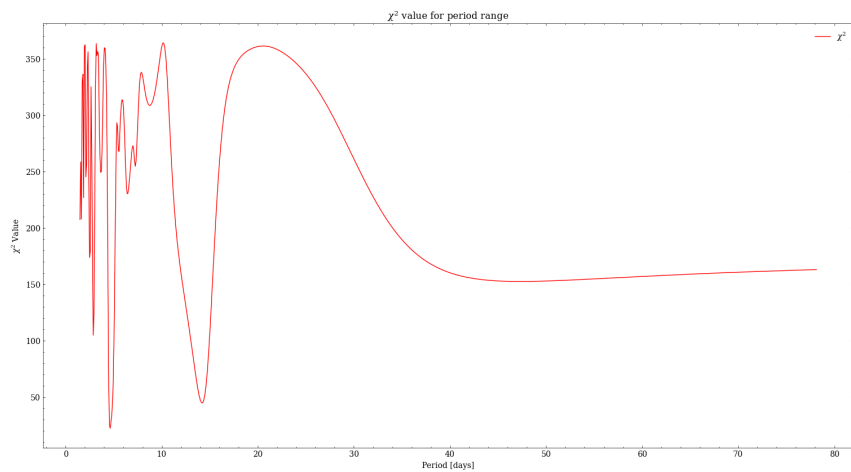


((b)) A graph showing the offset between the calibrated magnitude and the true magnitude for reference stars in the field of V Lacertae, which was used to mitigate night-to-night variations.

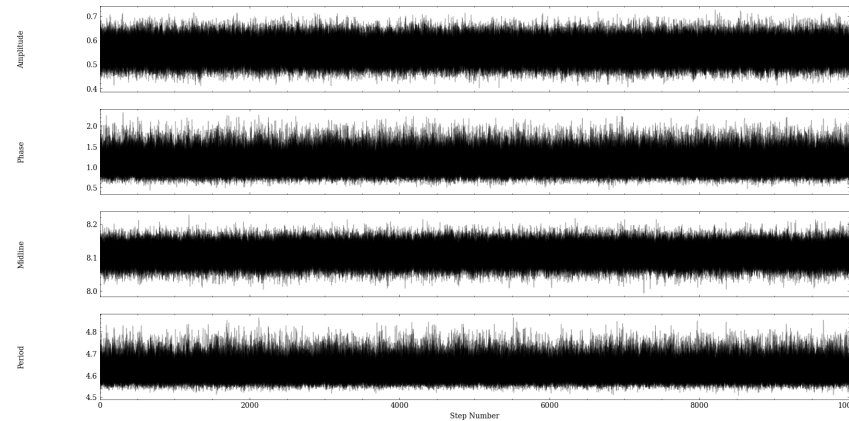


((c)) Initial light curve following differential photometry for V Lacertae.

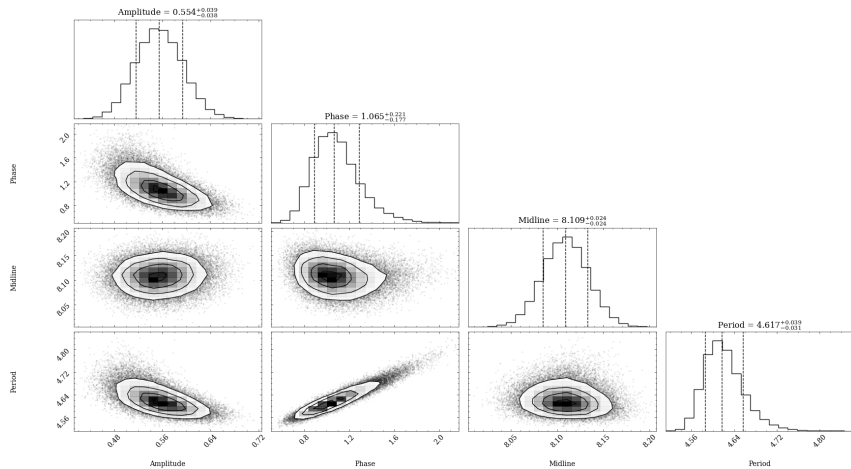
Figure 47: Photometric analysis and sinusoidal modelling results for V Lacertae (1 of 2).



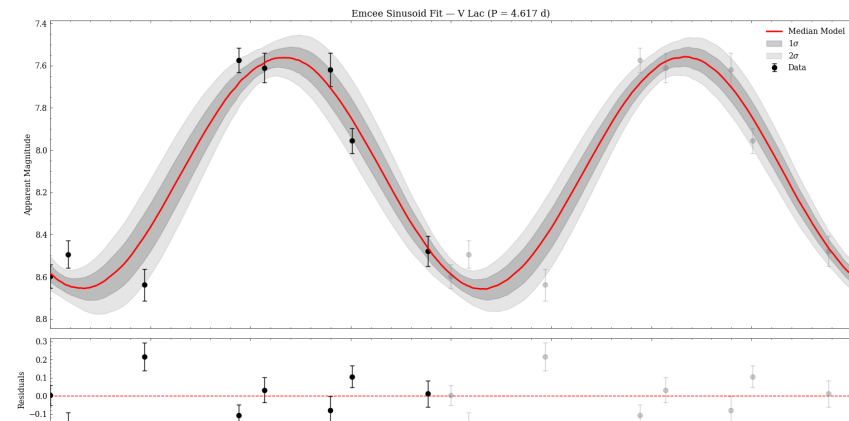
((d)) The χ^2 grid search for V Lacertae using the sinusoidal model.



((e)) The parameter time series of V Lacertae.



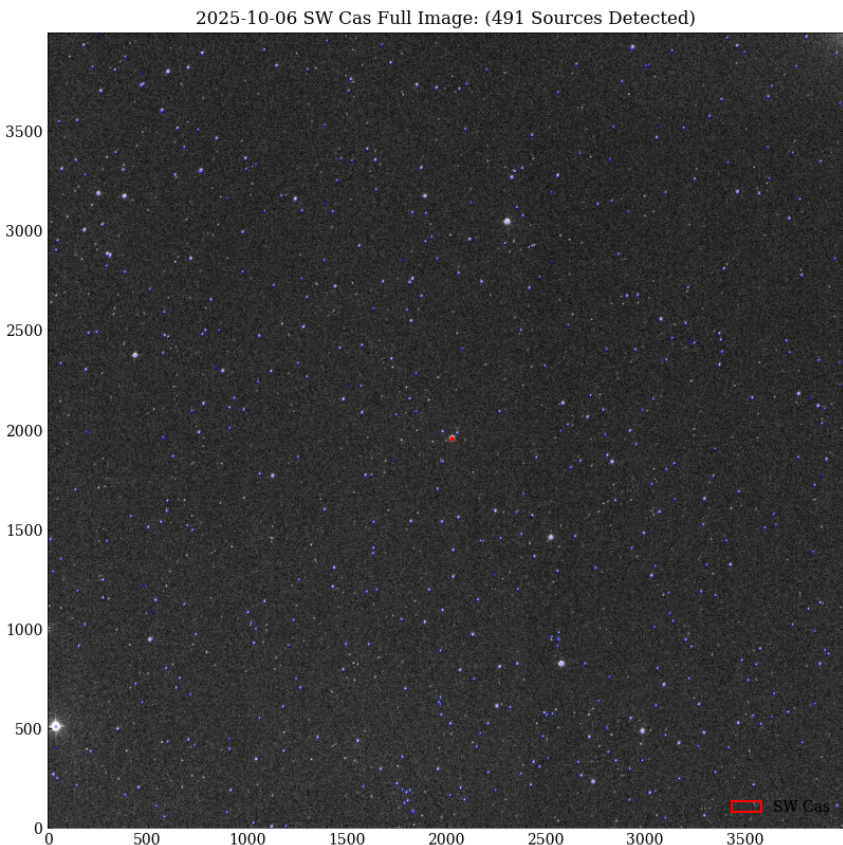
((f)) The posterior spread for V Lacertae.



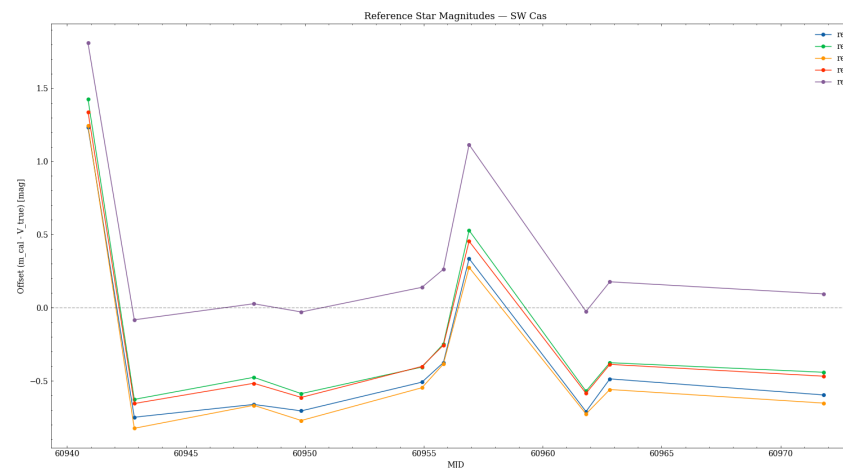
((g)) The final sinusoidal fit to V Lacertae.

Figure 47: Photometric analysis and sinusoidal modelling results for V Lacertae (2 of 2).

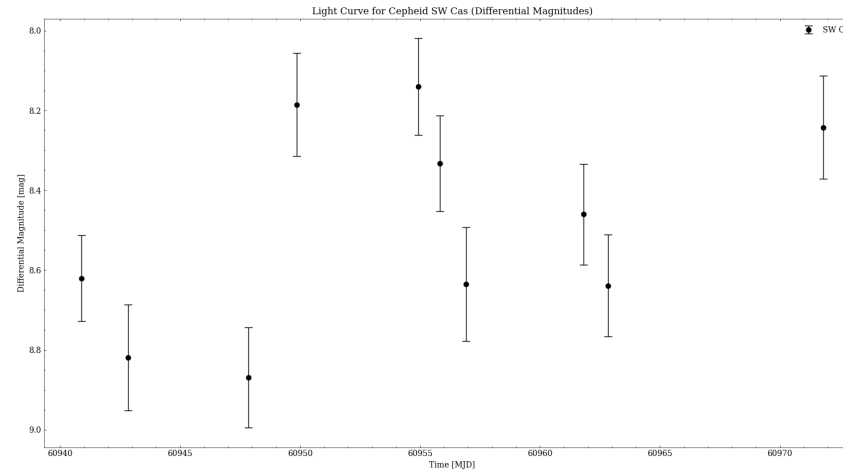
CEPHEID 08 - SW CASSIOPEIAE



((a)) DAOIND results for SW Cassiopeiae. The estimated location of the Cepheid is shown in red.

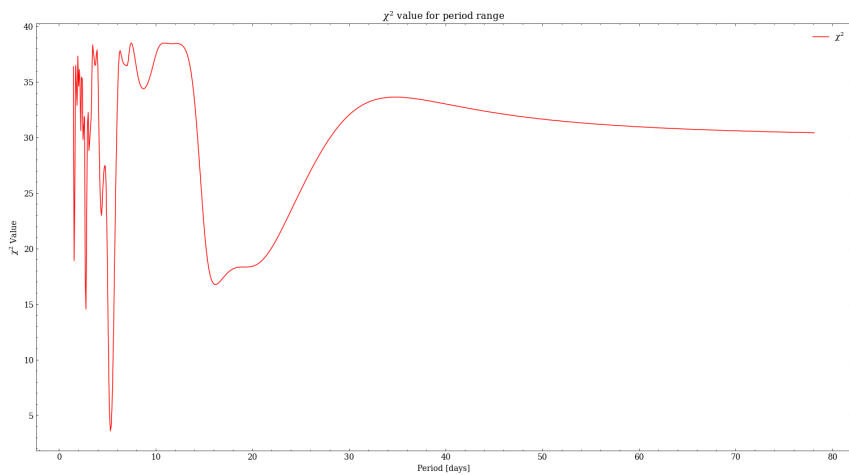


((b)) A graph showing the offset between the calibrated magnitude and the true magnitude for reference stars in the field of SW Cassiopeiae, which was used to mitigate night-to-night variations.

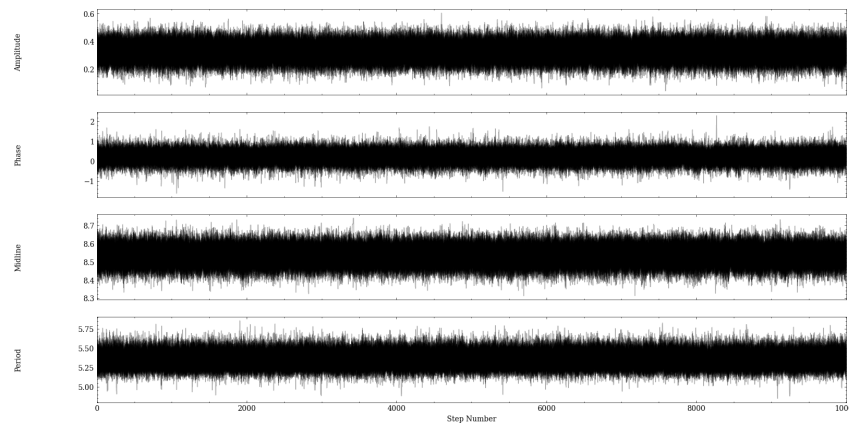


((c)) Initial light curve following differential photometry for SW Cassiopeiae.

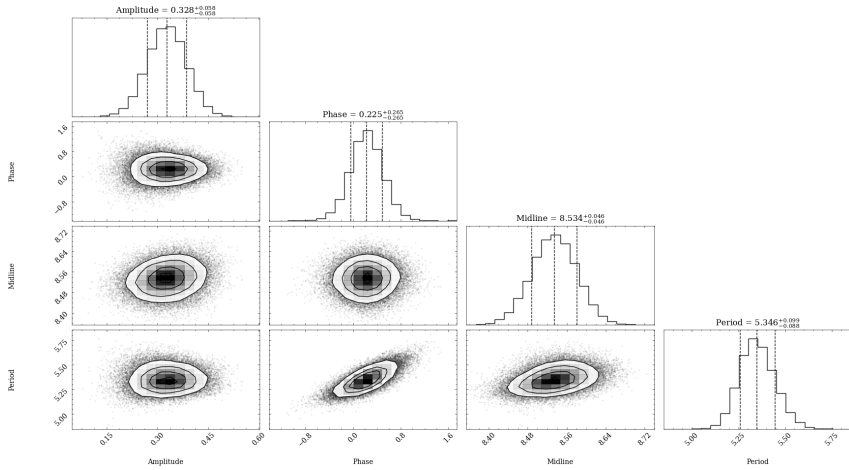
Figure 48: Photometric analysis and sinusoidal modelling results for SW Cassiopeiae (1 of 2).



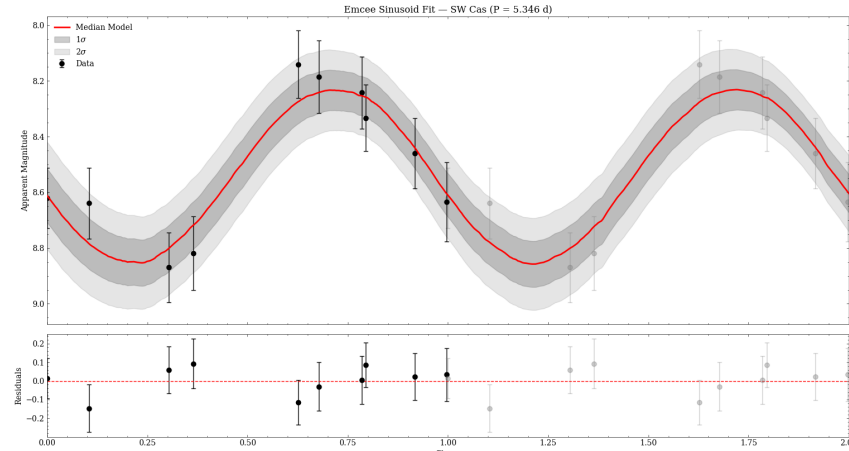
((d)) The χ^2 grid search for SW Cassiopeiae using the sinusoidal model.



((e)) The parameter time series of SW Cassiopeiae.



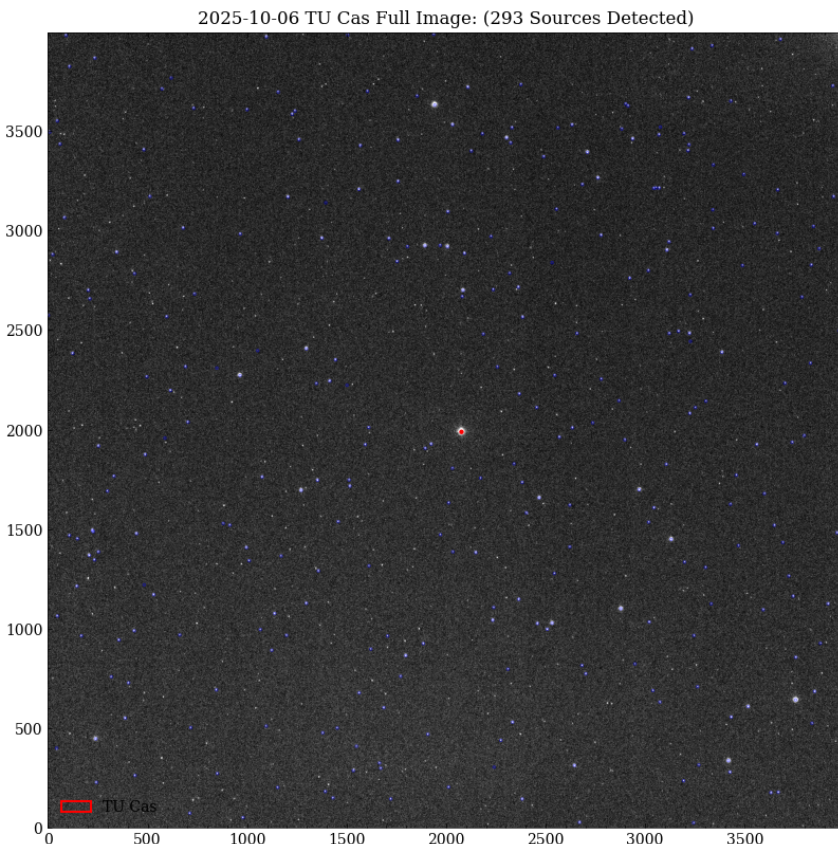
((f)) The posterior spread for SW Cassiopeiae.



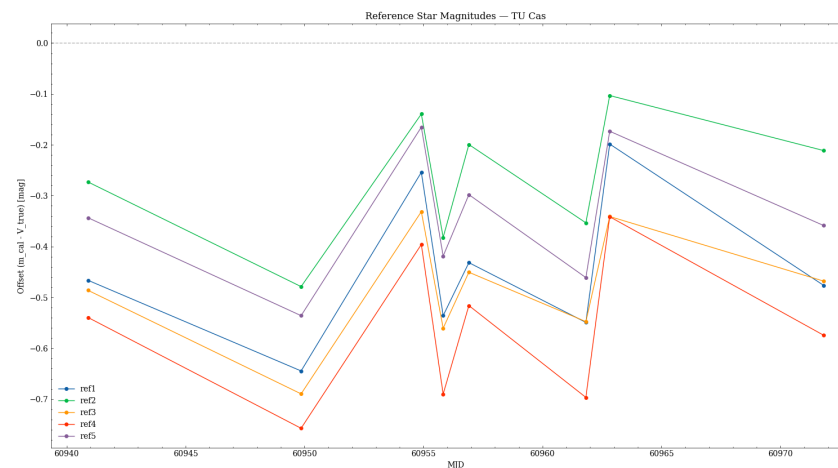
((g)) The final sinusoidal fit to SW Cassiopeiae.

Figure 48: Photometric analysis and sinusoidal modelling results for SW Cassiopeiae (2 of 2).

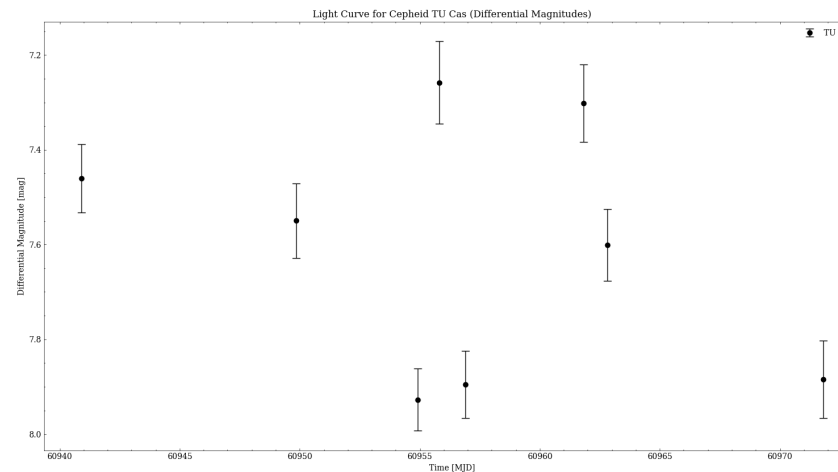
CEPHEID 09 - TU CASSIOPEIAE



((a)) DAOIND results for TU Cassiopeiae. The estimated location of the Cepheid is shown in red.



((b)) A graph showing the offset between the calibrated magnitude and the true magnitude for reference stars in the field of TU Cassiopeiae, which was used to mitigate night-to-night variations.



((c)) Initial light curve following differential photometry for TU Cassiopeiae.

Figure 49: Photometric analysis and sawtooth modelling results for TU Cassiopeiae (1 of 2).

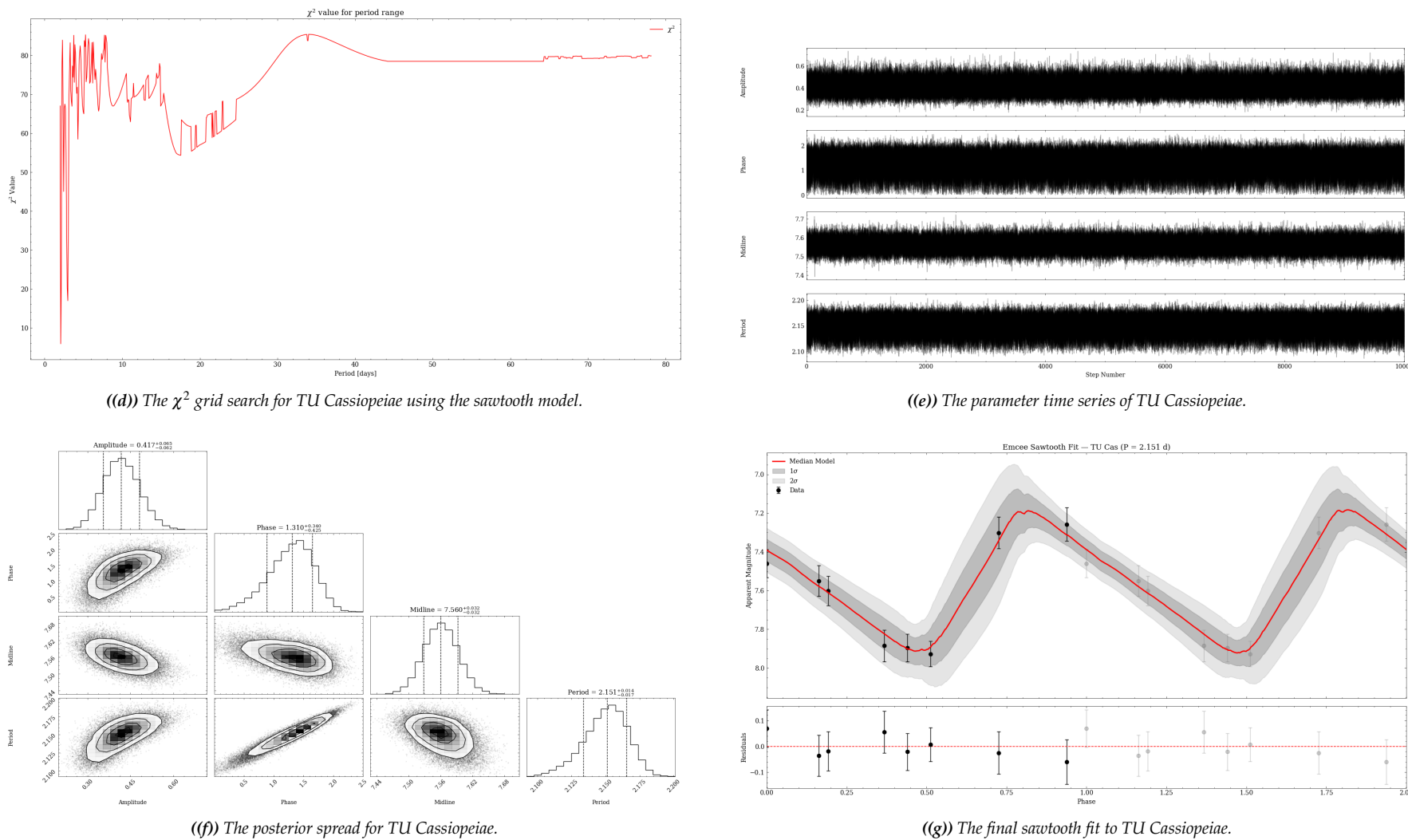
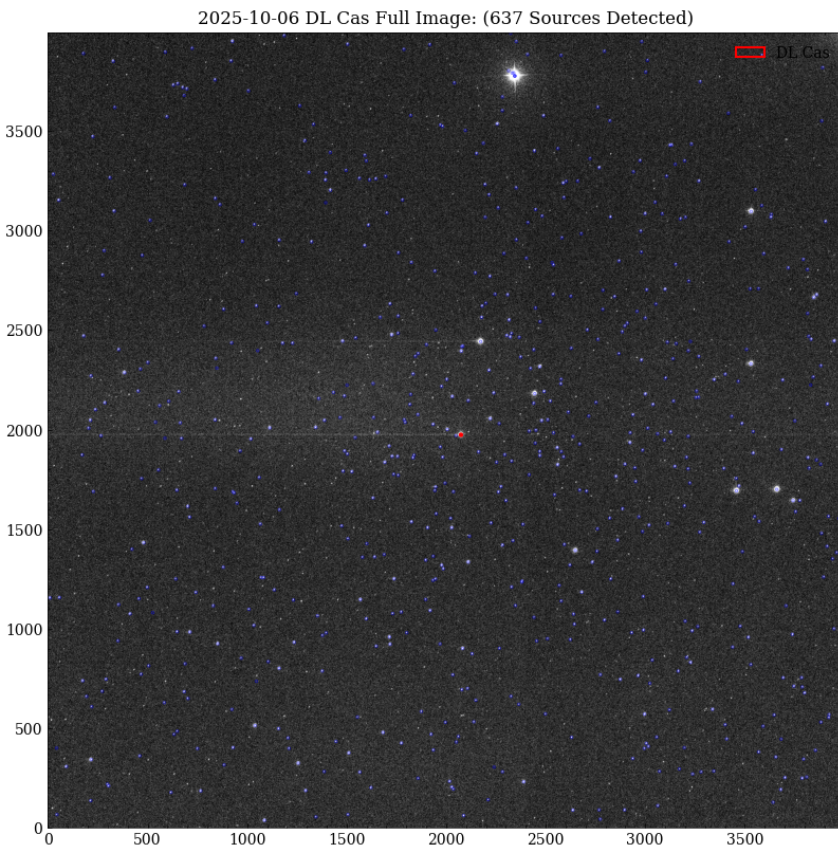
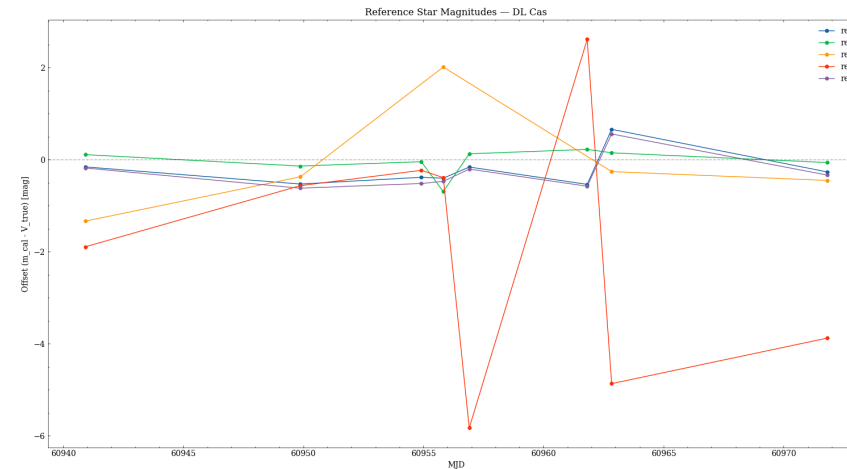


Figure 49: Photometric analysis and sawtooth modelling results for TU Cassiopeiae (2 of 2).

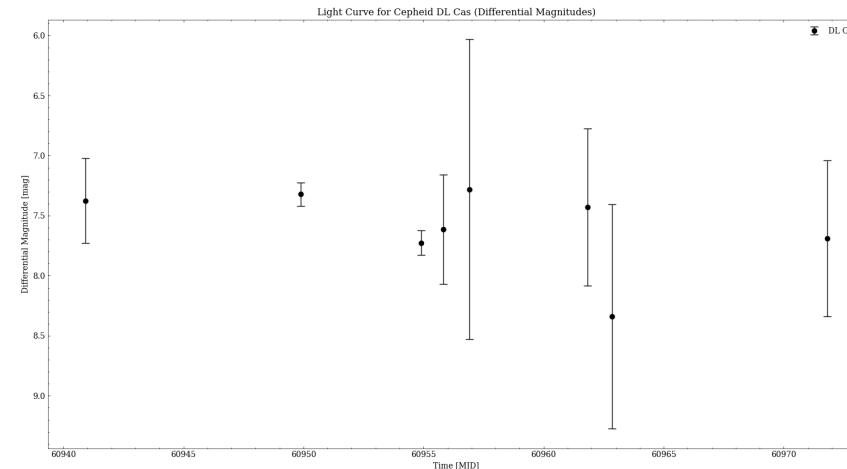
CEPHEID 10 - DL CASSIOPEIAE



((a)) DAO FIND results for DL Cassiopeiae. The estimated location of the Cepheid is shown in red.

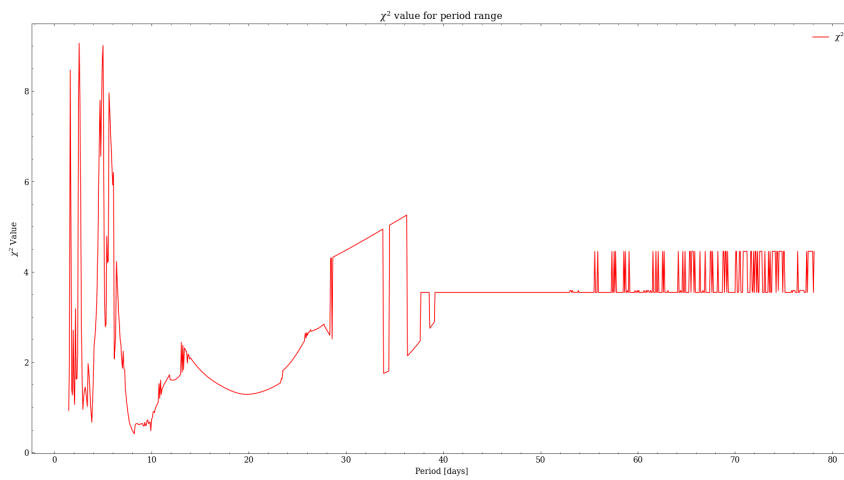


((b)) A graph showing the offset between the calibrated magnitude and the true magnitude for reference stars in the field of DL Cassiopeiae, which was used to mitigate night-to-night variations.

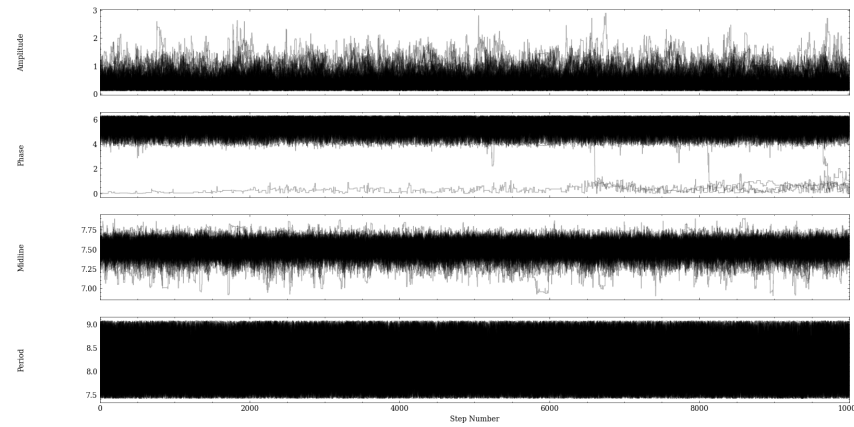


((c)) Initial light curve following differential photometry for DL Cassiopeiae.

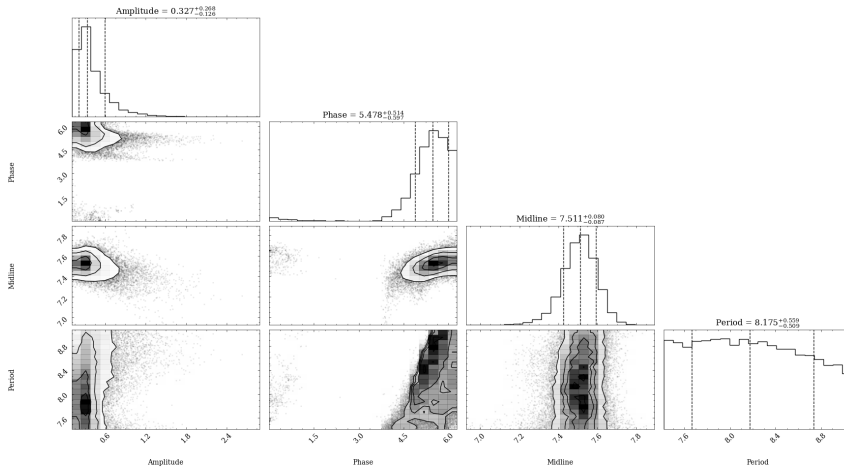
Figure 50: Photometric analysis and sawtooth modelling results for DL Cassiopeiae (1 of 2).



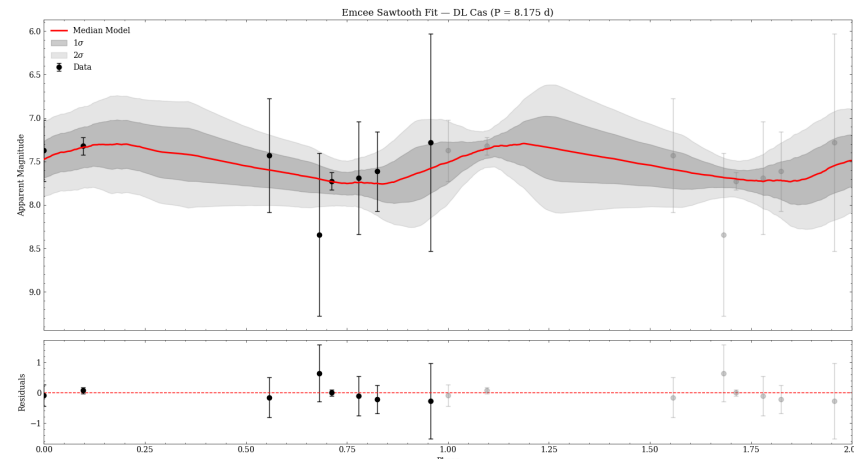
((d)) The χ^2 grid search for DL Cassiopeiae using the sawtooth model.



((e)) The parameter time series of DL Cassiopeiae.



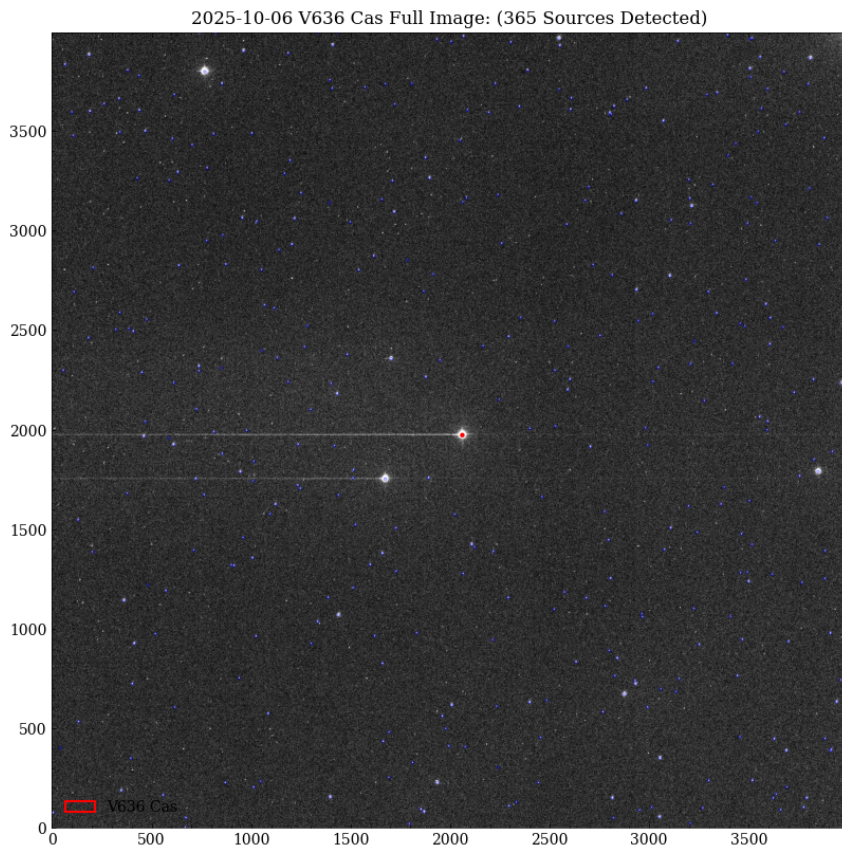
((f)) The posterior spread for DL Cassiopeiae.



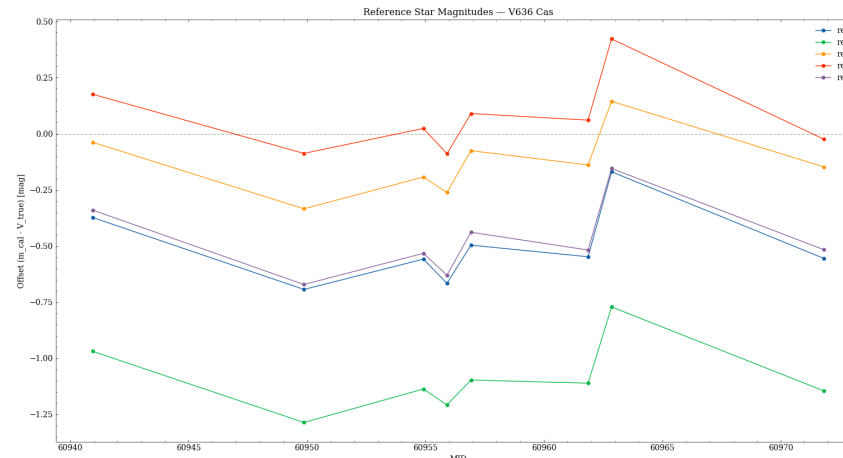
((g)) The final sawtooth fit to DL Cassiopeiae.

Figure 50: Photometric analysis and sawtooth modelling results for DL Cassiopeiae (2 of 2).

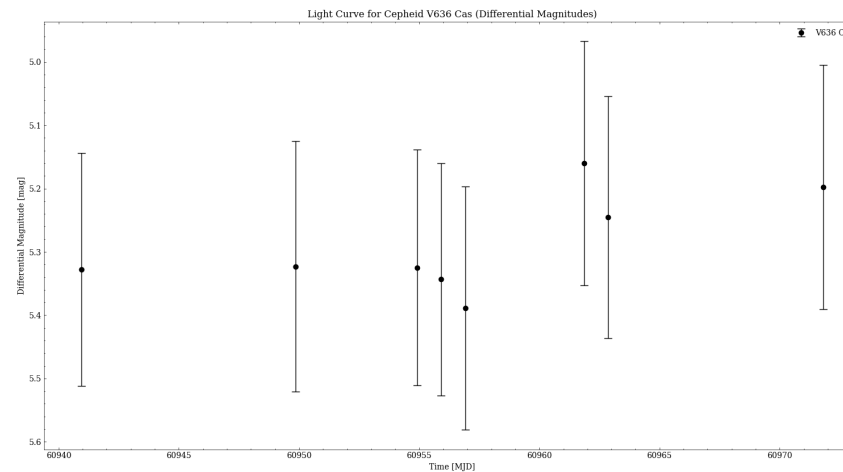
CEPHEID 11 - V636 CASSIOPEIAE



((a)) DAOIND results for V636 Cassiopeiae. The estimated location of the Cepheid is shown in red.

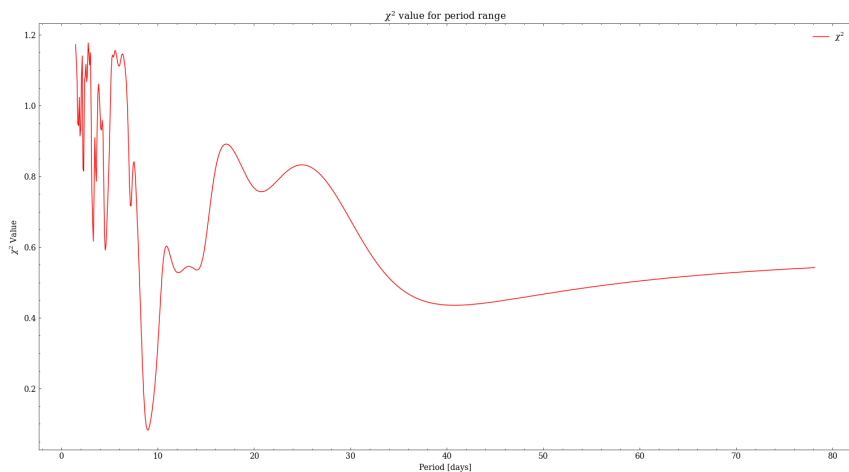


((b)) A graph showing the offset between the calibrated magnitude and the true magnitude for reference stars in the field of V636 Cassiopeiae, which was used to mitigate night-to-night variations.

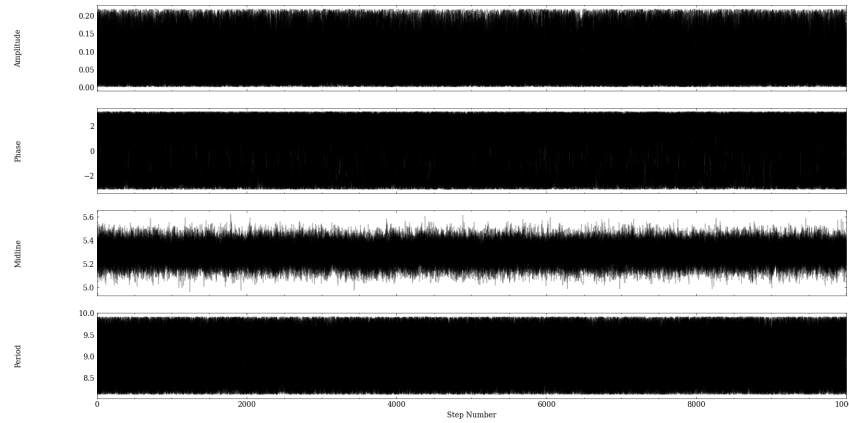


((c)) Initial light curve following differential photometry for V636 Cassiopeiae.

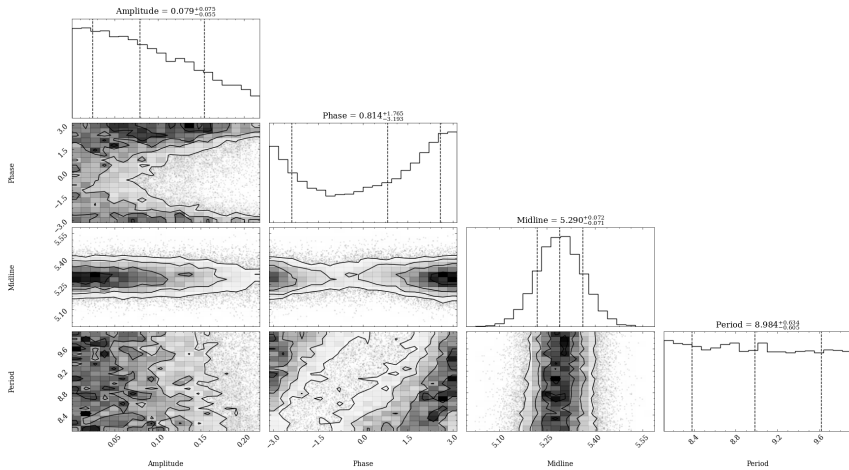
Figure 51: Photometric analysis and sinusoidal modelling results for V636 Cassiopeiae (1 of 2).



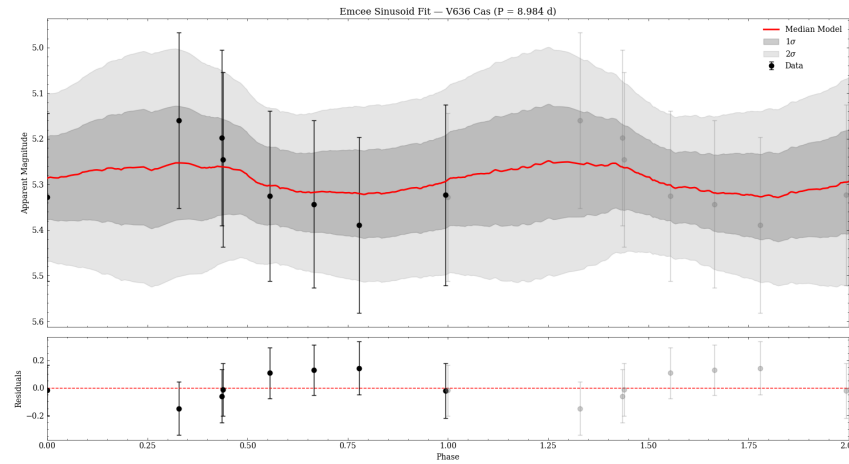
((d)) The χ^2 grid search for V636 Cassiopeiae using the sinusoidal model.



((e)) The parameter time series of V636 Cassiopeiae.



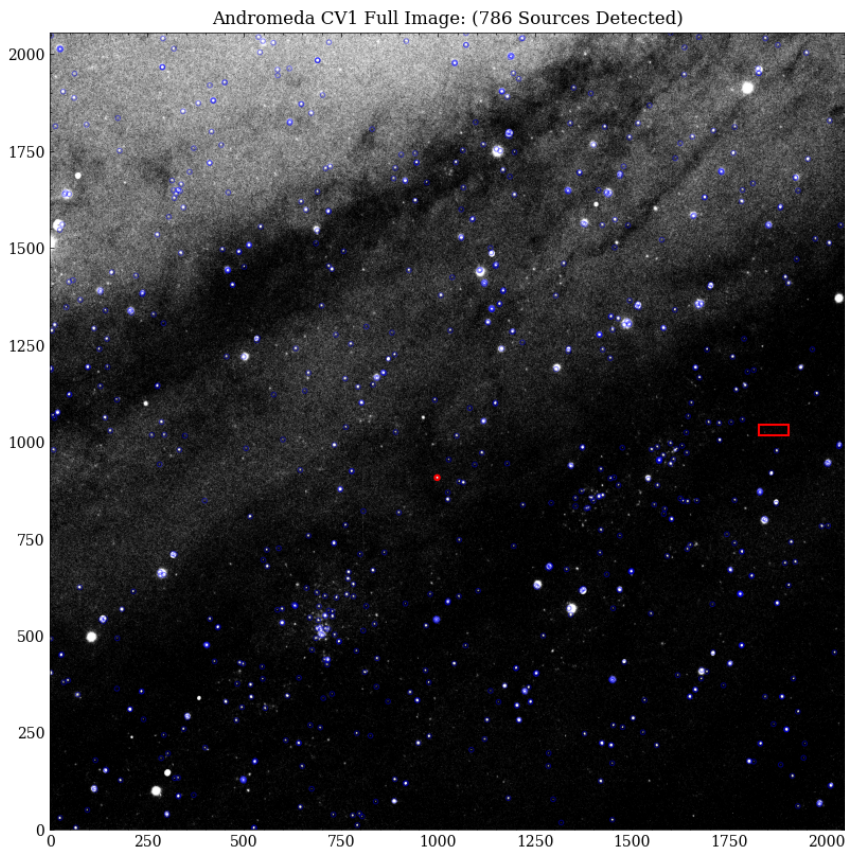
((f)) The posterior spread for V636 Cassiopeiae.



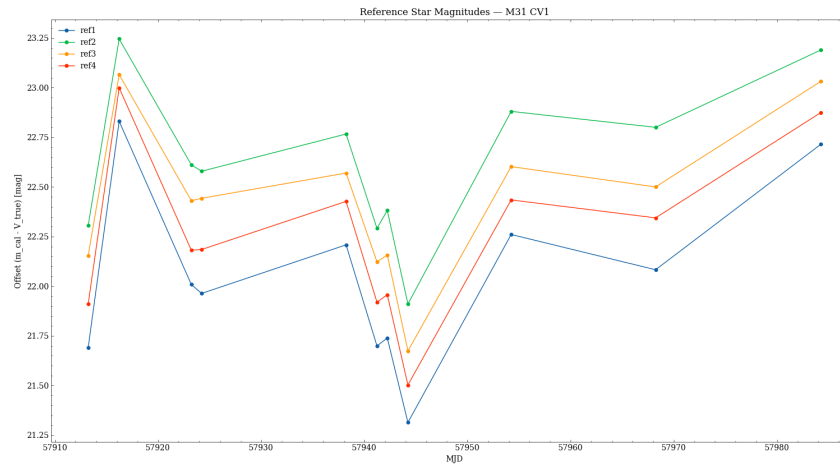
((g)) The final sinusoidal fit to V636 Cassiopeiae.

Figure 51: Photometric analysis and sinusoidal modelling results for V636 Cassiopeiae (2 of 2).

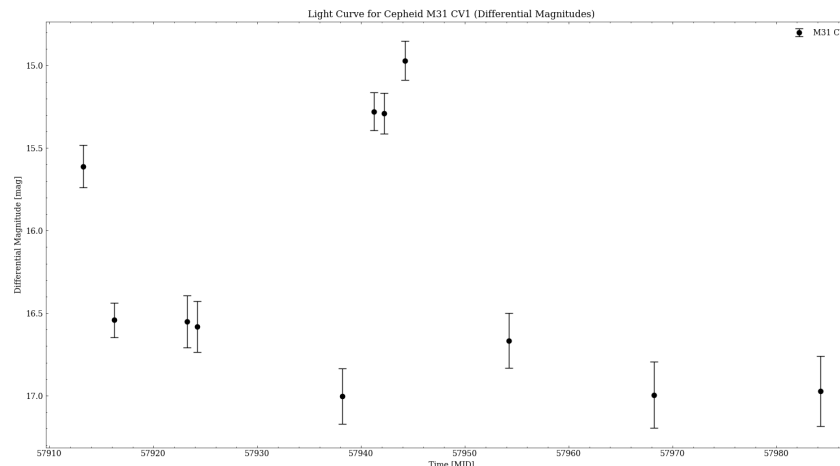
ANDROMEDA CEPHEID - M31 CV1



((a)) DAOIND results for M31 CV1. The estimated location of the Cepheid is shown in red.

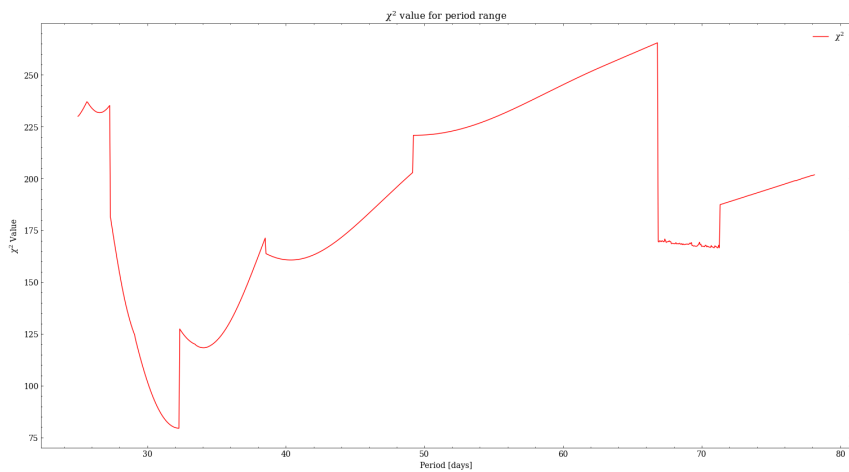


((b)) A graph showing the offset between the calibrated magnitude and the true magnitude for reference stars in the field of M31 CV1, which was used to mitigate night-to-night variations.

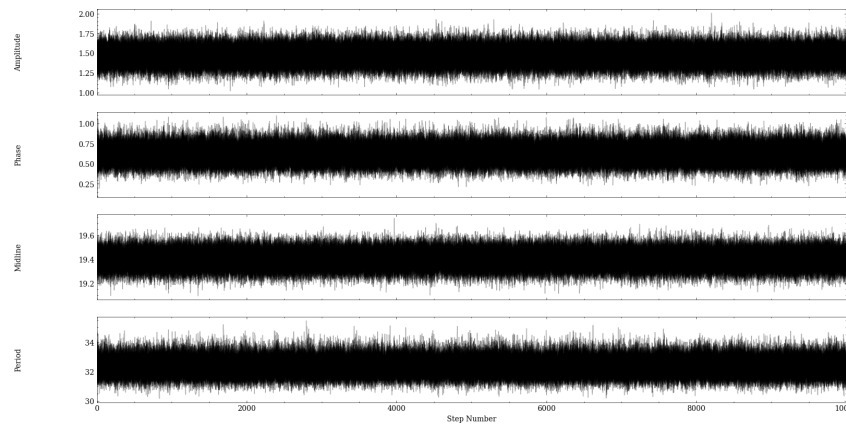


((c)) Initial light curve following differential photometry for M31 CV1.

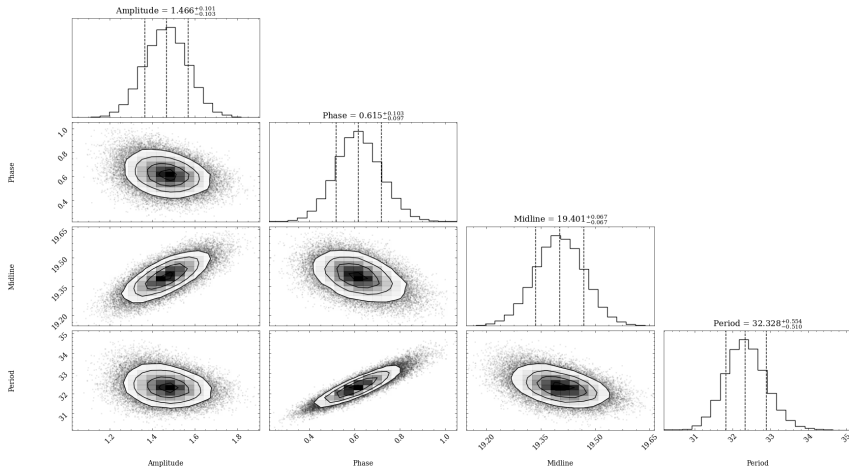
Figure 52: Photometric analysis and sinusoidal modelling results for M31 CV1 (1 of 2).



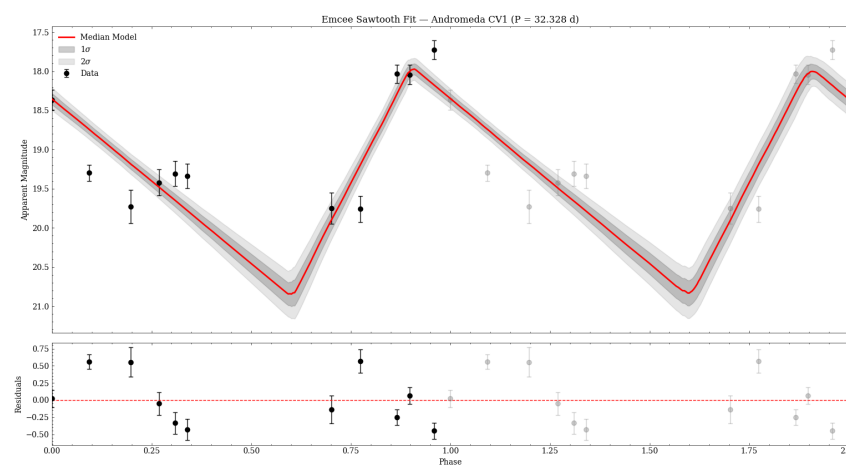
((d)) The χ^2 grid search for M31 CV1 using the sawtooth model.



((e)) The parameter time series of M31 CV1.



((f)) The posterior spread for M31 CV1.



((g)) The final sawtooth fit to M31 CV1.

Figure 52: Photometric analysis and sawtooth modelling results for M31 CV1 (2 of 2).

OBSERVATION NIGHTS - AIRMASS PLOTS

2025-09-22

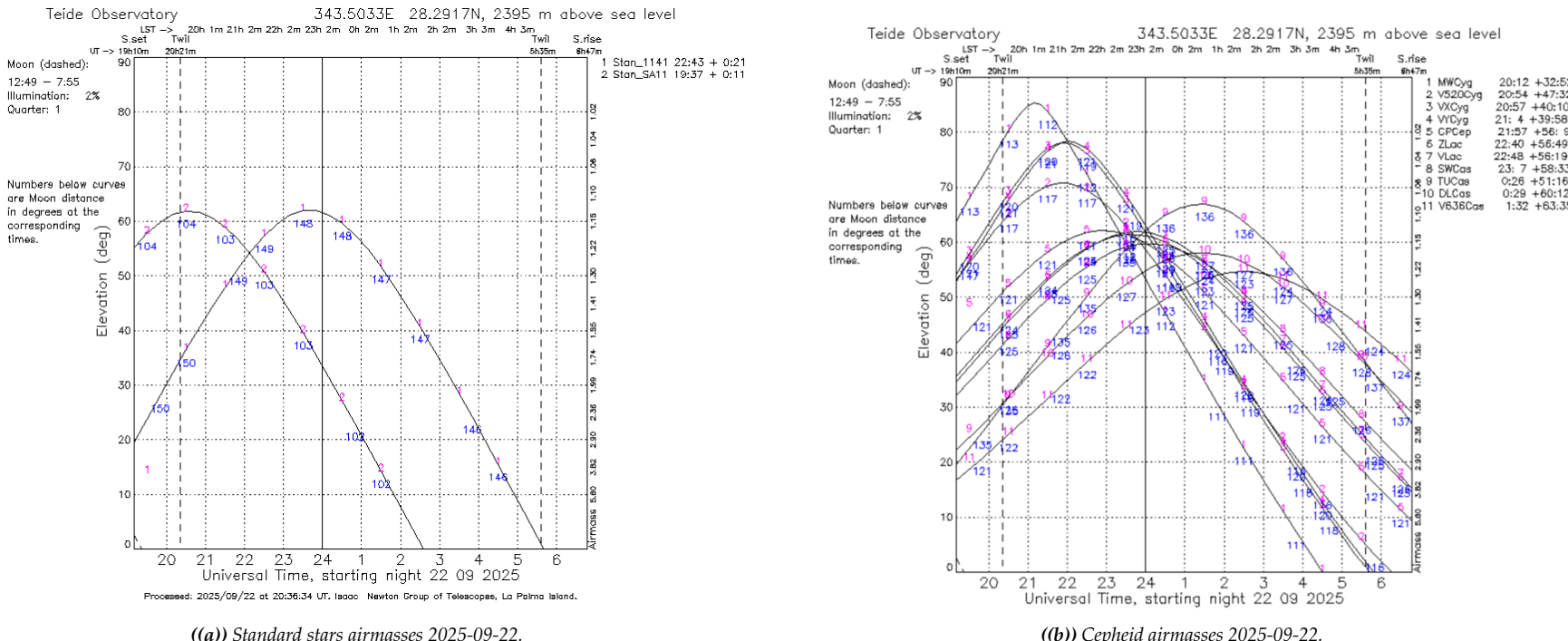


Figure 53: Airmass plots of the standard stars and Cepheids on the night of 2025-09-22 [76].

2025-10-06

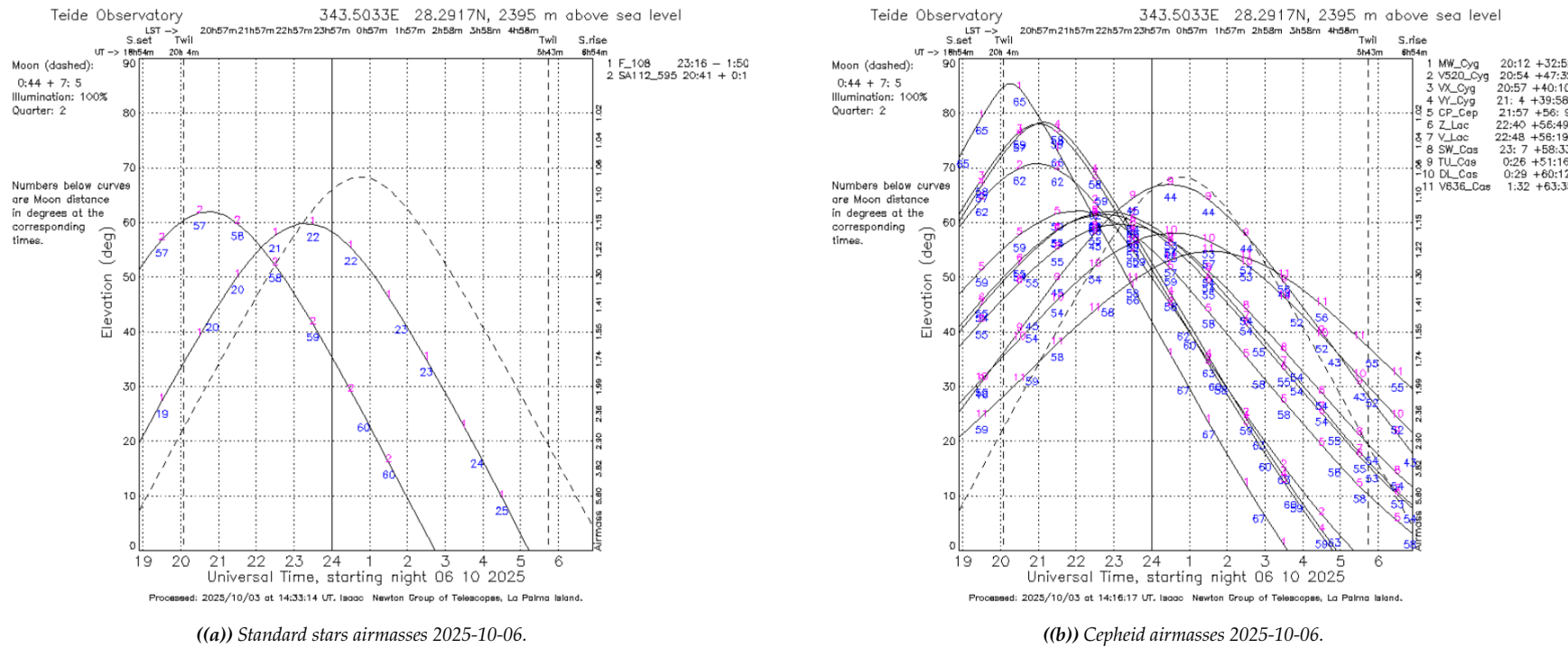


Figure 54: Airmass plots of the standard stars and Cepheids on the night of 2025-10-06 [76].

2025-10-07

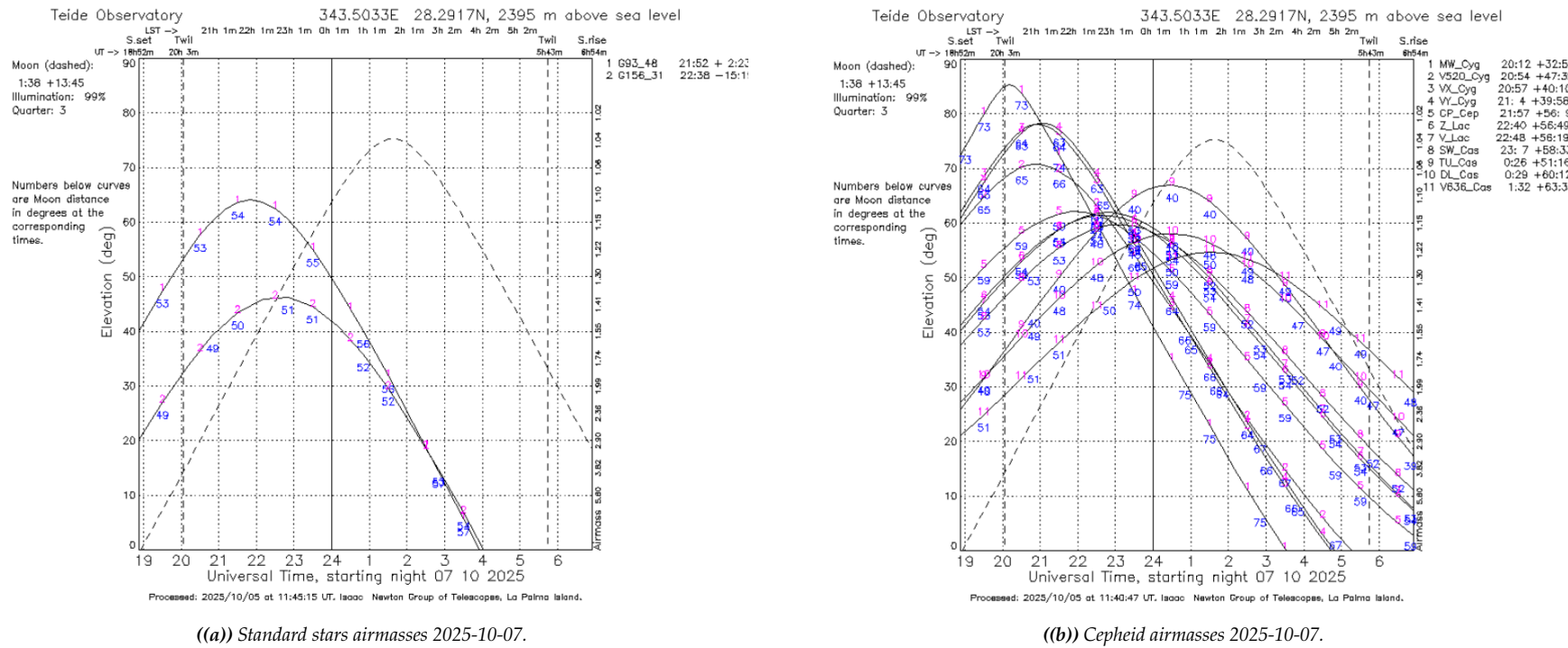


Figure 55: Airmass plots of the standard stars and Cepheids on the night of 2025-10-07 [76].

2025-10-08

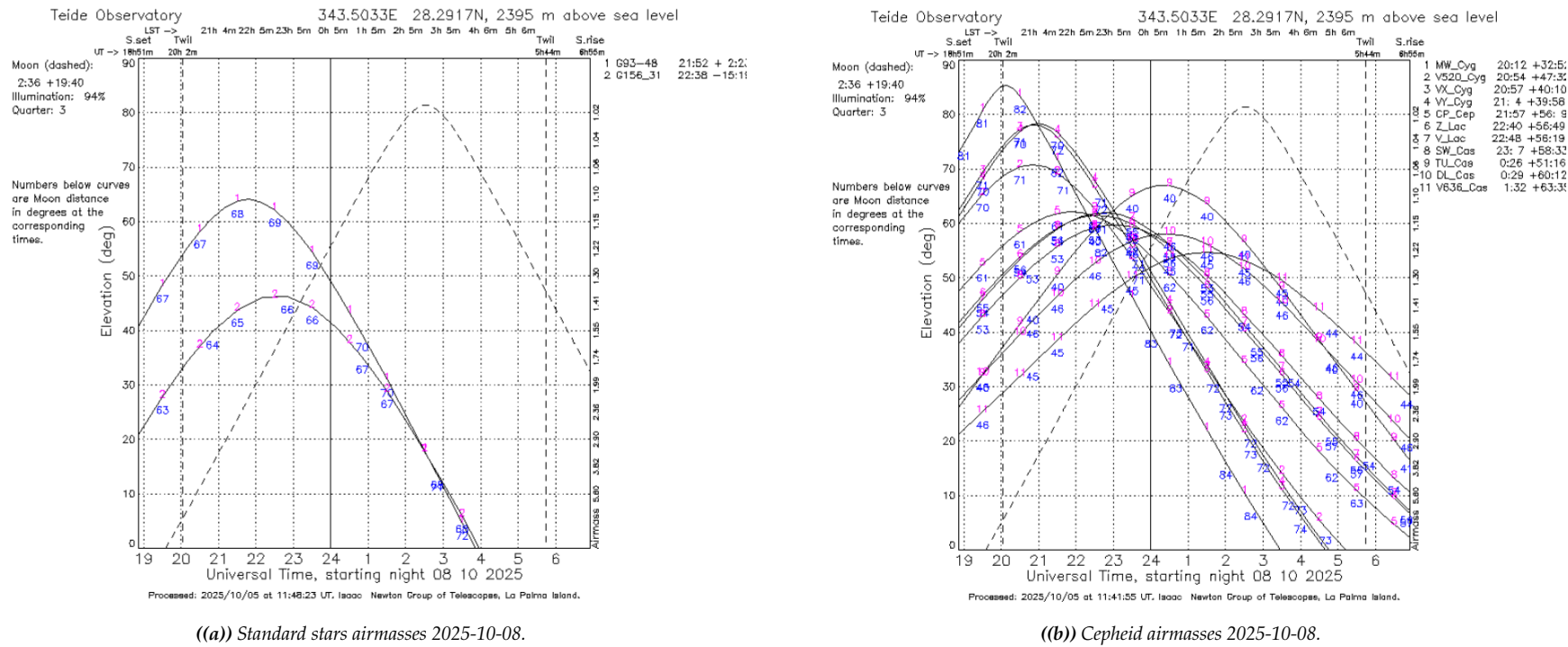


Figure 56: Airmass plots of the standard stars and Cepheids on the night of 2025-10-08 [76].

2025-10-13

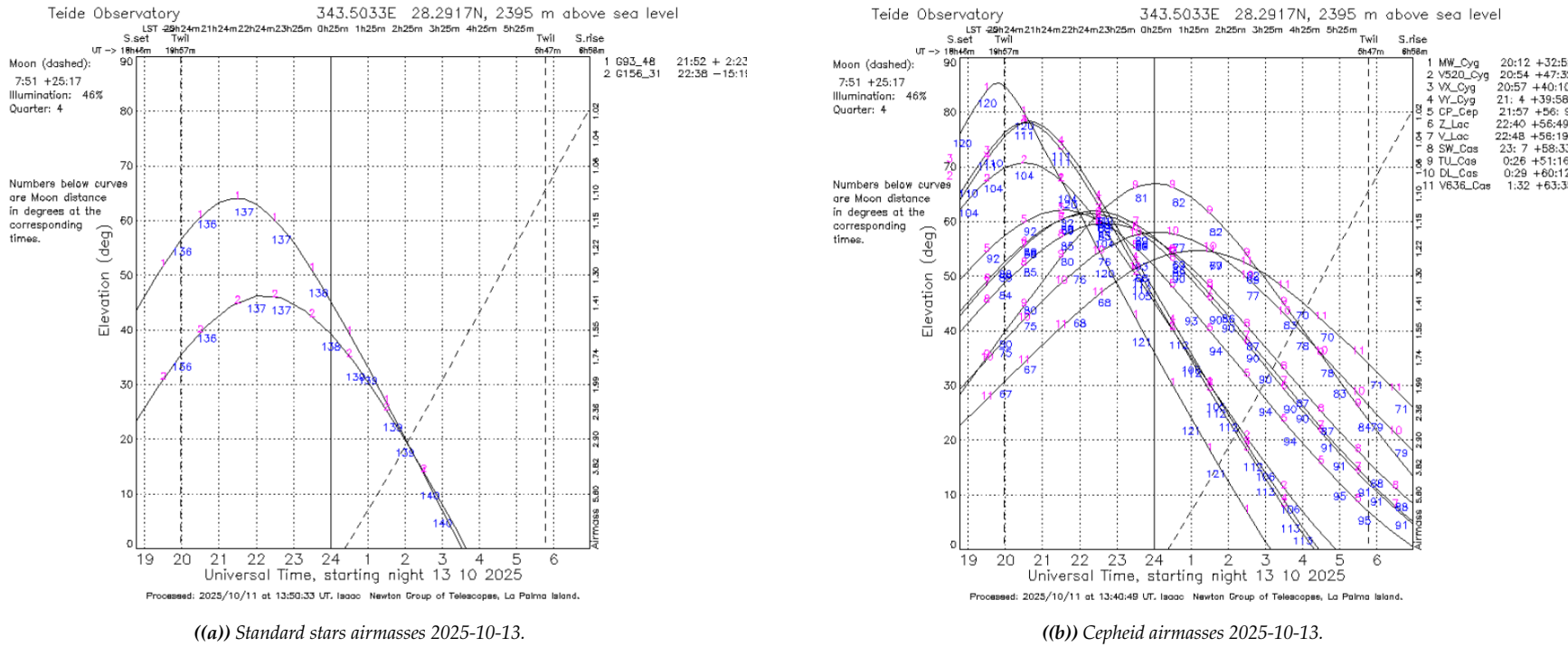


Figure 57: Airmass plots of the standard stars and Cepheids on the night of 2025-10-13 [76].

2025-10-14

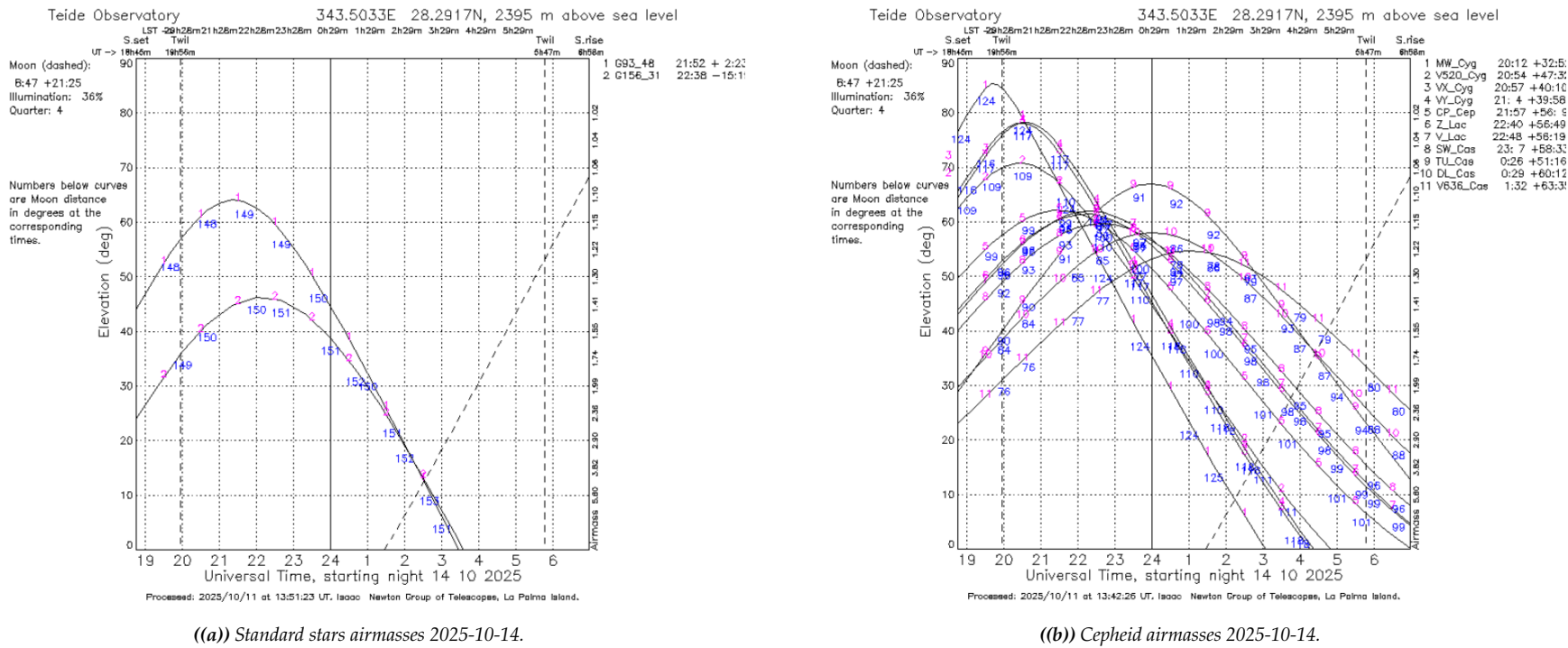


Figure 58: Airmass plots of the standard stars and Cepheids on the night of 2025-10-14 [76].

2025-10-23

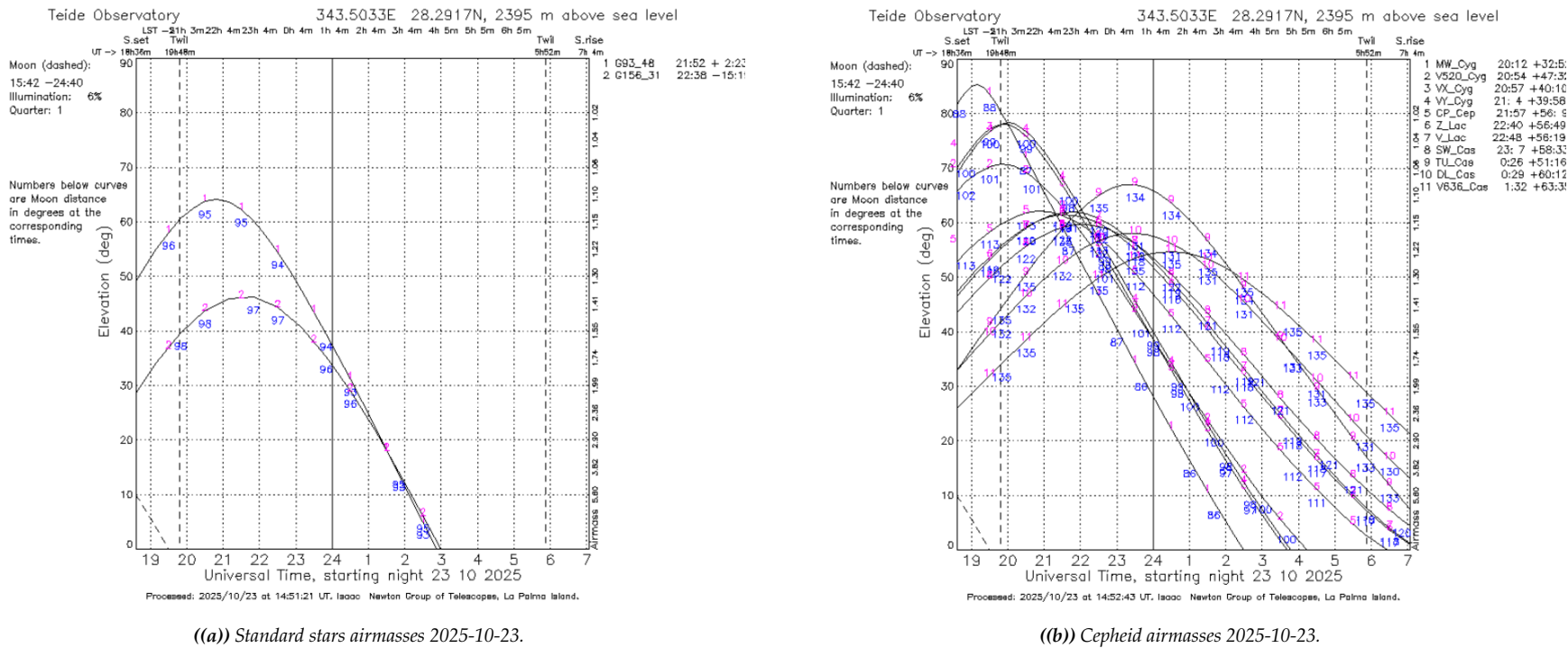


Figure 59: Airmass plots of the standard stars and Cepheids on the night of 2025-10-23 [76].